Lithium Transition Metal Oxides and Battery Applications

by

Wu Li

B. Sc. Zhongshan University, P. R. China, 1985
M. Sc. Zhongshan University, P. R. China, 1988
M. Sc. Simon Fraser University, Canada, 1992

A THESIS SUBMITTED IN PARTIAL FULFILLMENT OF
THE REQUIREMENTS FOR THE DEGREE OF
DOCTOR OF PHILOSOPHY
in the Department
of
Physics

SIMON FRASER UNIVERSITY
September 1994

APPROVAL

Name: Wu Li
Degree Doctor of Philosophy
Title of Thesis: **Lithium Transition Metal Oxides and Battery Applications**

Examining Committee: Dr. B. Frisken
Chairperson

Dr. Jeff Dahn
Senior Supervisor

Dr. Robert F. Frindt

Dr. Mike Plischke

Dr. J. C. Irwin
Internal Examiner

Dr. Mike M. Thackeray
External Examiner,

Date Approved: September 12, 1994
September 12, 1994

PARTIAL COPYRIGHT LICENSE

I hereby grant to Simon Fraser University the right to lend my thesis, project or extended essay (the title of which is shown below) to users of the Simon Fraser University Library, and to make partial or single copies only for such users or in response to a request from the library of any other university, or other educational institution, on its own behalf or for one of its users. I further agree that permission for multiple copying of this work for scholarly purposes may be granted by me or the Dean of Graduate Studies. It is understood that copying or publication of this work for financial gain shall not be allowed without my written permission.

Title of Thesis/Project/Extended Essay

Lithium Transition Metal Oxides and Battery Applications

Author: _____

(signature)

_____

(name)

3 October 1994

(date)

Abstract

Lithium transition metal oxides are currently the cathode materials of choice for lithium battery applications. Because the electrochemical performance of these materials depends on their structure, it is crucial to understand their structures. We describe the structures of these important materials and use a lattice gas model to explain the structures of the rock-salt derived $LiMO_2$ (M=Sc, Ti, V, Cr, Mn, Fe, Co, Ni, Cu) materials. Using mean field theory and Monte Carlo methods, we found that both the spinel (atacamite) and layered structures have identical entropy and free energy. Furthermore, we use these theoretical results to explain why $LiCoO_2$ exists in two phases, and why they have similar X-ray diffraction patterns.

We developed a new in-situ X-ray cell and used it to observe the changes in structure of Li_xNiO_2 with x. Three hexagonal phases and one monoclinic phase are observed. Three coexisting phase regions are also found. These phase transitions are correlated with anomalies in the electrochemical behavior of Li_xNiO_2.

In order to synthesize lithium-rich transition metal oxides which are suitable for rechargeable lithium-ion battery applications, we propose a new method of lithium intercalation from aqueous solutions. Using this method, we synthesize $Li_2Mn_2O_4$ and γ-$LiMnO_2$ which can be used as cathode materials in rechargeable lithium cells with non-aqueous electrolytes. A simple theory is used to understand lithium intercalation from aqueous solutions. Furthermore, the competition between hydrogen intercalation and lithium intercalation is investigated and it is confirmed that further electrochemical reduction of $Li_2Mn_2O_4$ and γ-$LiMnO_2$ results in the formation of $Mn(OH)_2$.

Based on the understanding of lithium intercalation from aqueous solutions, we developed rechargeable lithium-ion batteries with aqueous electrolytes. Cells with $LiMn_2O_4$ and $VO_2(B)$ as electrodes and 5 M $LiNO_3$ in water as the electrolyte provide a fundamentally safe and cost-effective technology that can compete with nickel-cadmium and lead-acid batteries on the basis of stored energy per unit of weight. Other couples like $LiMn_2O_4/\gamma\text{-}Li_{0.36}MnO_2$ are also tested in the cells with various aqueous electrolytes. Using electrochemical methods, we confirmed that lithium intercalation reactions occur in these $LiMn_2O_4/VO_2(B)$, $LiMn_2O_4/VO_2(B)$ cells with aqueous electrolytes. Such a fundamentally safe and inexpensive technology provides a new option for scientists and engineers to make practical batteries for electric vehicle applications.

Acknowledgments

During my four years at SFU, Dr. Jeff Dahn, my senior supervisor spent a lot of time to support my research. I would like to thank him for his encouragement and advice throughout the entire research work. The laboratory under his leadership provides a very good environment to do research and this makes it easier to finish my Ph. D thesis. I believe that his excellent experimental skill and open mind will benefit the rest of my career.

I also would like to thank Dr. J. N. Reimers for his assistance with programming and for the useful suggestions and discussions, especially in the theoretical work described here.

I wish to thank Dr. R. Frindt, Dr. M. Plischke, Dr. M. M. Thackeray, Dr. B. Frisken and Dr. J. C. Irwin for serving on for my examining committee.

I also wish to thank Dr. U. von Sacken, Dr. Q. Zhong and D. Wainwright at Moli Energy (1990) Ltd. for various support, from samples and ideas to financial aid. The financial aid from the Science Council of British Columbia and Moli Energy (1990) Ltd. are greatly appreciated.

Finally I wish to thank my fellow students B. M. Way, Hang Shi, Erik Rossen, Eric Fuller, Oliver Schilling, Michelle Baudais, Alf Wilson, Tao Zheng for their general support.

Contents

List of Tables

List of Figures

Chapter 1. Introduction

Rechargeable lithium batteries have some advantages over conventional rechargeable batteries. They operate at higher voltage and provide higher energy density than lead acid, Ni-Cd or Ni-MH rechargeable batteries. They also have longer shelf life. Many types of portable electronic equipment, such as CD players, cordless phones, and laptop computers need high energy density power sources, so rechargeable lithium batteries are attractive for application in these types of equipment. Another potential application of rechargeable lithium batteries may be in electric vehicles.

The periodic table is a good place to look for materials for high energy density rechargeable batteries. Hydrogen is the lightest element and can store very high energy density per unit weight. However, solid or liquid hydrogen does not exist at room temperature, hence hydrogen has relatively low energy density per unit volume. Lithium is the third lightest element after hydrogen and helium and therefore is best candidate for high energy density electrochemical storage because of its electronegativity and the availability of its solid state.

Rechargeable Li batteries consist of four main parts, the negative electrode, the positive electrode, the electrolyte and the separator. The positive electrode is usually an intercalation compound. The negative electrode can be lithium metal, a lithium alloy or another intercalation compound. Intercalation compounds are materials into which lithium ions can be inserted and subsequently removed without significantly changing the basic structure of the compound. In other words, lithium can be placed in empty interstitial sites within the lattices of intercalation hosts without damage to the host

lattices. The lithium in the host can be expressed as Li_x(Host) where x is the amount of lithium intercalated in the host.

The chemical potential of lithium in lithium metal is different from that of lithium in intercalation compounds. Lithium atoms in different intercalation compounds also have different chemical potentials. When lithium moves between lithium metal and an intercalation compound, or between one intercalation compound and another, the difference in chemical potentials is responsible for the voltage of lithium batteries. The electrolyte provides a lithium ion path between the anode and the cathode. The separator is a porous membrane which holds the electrolyte and electrically isolates the positive and negative electrodes.

Figure 1.1 shows a Li/Lithium intercalation compound rechargeable battery. During discharge a lithium atom loses an electron and becomes a lithium ion, electrons travel from the lithium metal to the intercalation compound through the outside circuit and lithium ions travel from the lithium metal to the intercalation compound through the electrolyte path. The lithium ions and electrons combine, then intercalate into the intercalation compound making both electrodes electroneutral. During the recharge of the cell the lithium atoms deintercalate from the intercalation compound and are transported to the lithium metal. The voltage $V(x)$ of a Li/Li_x(Host) intercalation cell is given by (McKinnon and Haering)

$$V(x)=-(1/e)(\mu_{Li}^{int}(x)-\mu_{Li}^{0}) \qquad (1.1)$$

where μ_{Li}^{0} is the chemical potential of Li in Li metal and $\mu_{Li}^{int}(x)$ is the chemical potential of Li in the intercalation compound.

"Lithium-Ion" rechargeable cells are made by using a second intercalation compound in place of metallic lithium as the anode electrode. Thus, one intercalation compound is used as the anode and another is used as the cathode. These cells are so called "rocking-chair" cells because Li ions rock back and forth between the intercalation compounds during charge and discharge cycles. Figure 1.2 shows the discharge of a rocking chair cell where lithium ions deintercalate from the anode and travel to the other lithium intercalation compound through the nonaqueous electrolyte path. Simultaneously, the electrons travel from the anode to the cathode through the outside circuit. The anode and the cathode are therefore electroneutral during cell operation.

The chemical potential ranges of intercalated lithium in various intercalation compounds can be used to predict the voltage of rechargeable lithium cells. Figure 1.3 (Li, Wainwright and Dahn) shows the lithium binding energy in a variety of compounds, measured relative to lithium metal. The vertical lines besides the compounds correspond to their binding energy ranges versus x. LiF is not lithium intercalation compound, but is included as a reference. The chemical potentials of intercalation compounds can be obtained using the following equation:

$$-\mu_{Li}^{int}(x)=\text{Lithium Binding Energy} \qquad (1.2)$$

The cell energy is proportional to the product of the average voltage of the cell and the amount of lithium which can be transferred between the cathode and the anode. Therefore, higher cell voltage translates to higher energy density, provided the same amount of lithium can be transferred between the cathode and the anode. Usually, cathodes are chosen from intercalation

compounds with high lithium binding energy and anodes are chosen from those with low lithium binding energy in order to obtain high cell voltage. $LiNiO_2$ (Dahn, Sacken, Juzkow and Al-Janaby), $LiCoO_2$ (Nagaura and Tozawa) and $LiMn_2O_4$ (Tarascon and Guyomard) are near the top of the binding energy scale and therefore are suitable to be used as cathodes . For the anode, lithium metal, Li_xGraphite, and Li_xCoke are suitable. $LiNiVO_4$ was recently discovered to be a lithium intercalation compound (Fey, Li and Dahn) and has the highest binding energy among known lithium intercalation compounds. $LiNiVO_4$ has an energy capacity per unit weight significantly lower than that of $LiMn_2O_4$, $LiCoO_2$ and $LiNiO_2$ because less lithium can be deintercalated and intercalated from $LiNiVO_4$ compared to the other materials.

Figure 1.3 also shows the value of lithium binding energy above which materials are stable in air. Higher lithium binding energy means that lithium is more tightly bound to the compounds and it is difficult for Li to react with O_2, H_2O and CO_2 in air. $LiNiVO_4$, $LiNiO_2$, $LiCoO_2$, and $LiMn_2O_4$ are air stable since they have high lithium binding energy. Lithium metal, Li_xGraphite and Li_xCoke etc. are not air stable because their lithium binding energies are not high enough to prevent lithium from reacting with O_2, H_2O and CO_2.

Rechargeable lithium batteries using lithium metal anodes have the highest energy density since lithium metal has the lowest lithium binding energy as shown in figure 1.3. For the same reason, lithium metal is the most reactive among the lithium compounds. During the early 1980's most work on rechargeable lithium cells focussed on work involving the use of intercalation materials for the cathode and lithium metal for the anode. Lithium metal instantly reacts with the electrolyte to form a passivating film which prevents further reactions between the metal and the electrolyte

(Peled). This film is an electronic insulator and a lithium ion conductor. Therefore the lithium still has an ion path between electrodes. During cell cycling the surface area of lithium metal can grow significantly and this surface becomes very unstable. Thermal or mechanical abuse as well as short circuits can result in violent reactions between lithium metal and the electrolyte and can cause flame in heavily cycled cells. After the safety problem was discovered (Globe and Mail, Toronto), more and more research work shifted to the use of another intercalation compound as the anode.

Graphite and Coke are intercalation compounds and can be used to replace lithium metal as the anode to make "lithium-ion" rechargeable cells. The lithium binding energy in graphite and Coke is very close to that of lithium metal. Therefore, the loss of energy density incurred by using graphite or Coke as the anode is relatively small. A passivating film on the surface of graphite or Coke also forms while lithium intercalates into the materials for the first time and prevents lithium from reacting further with the electrolyte (Fong Sacken and Dahn). The surface area of graphite or Coke does not change during cell cycling since intercalation is a benign process. Therefore it is much safer to use graphite or Coke than to use lithium metal as the anode (Sacken, Nodwell, Sundher and Dahn). Since Li_xCoke and $Li_xGraphite$ are unstable in air, pure graphite or coke is used as a starting material in order to obtain an easy anode manufacturing process. Hence the only lithium source in lithium ion rechargeable battery is from the cathode. Thus, larger amounts of intercalated lithium per mole in the cathode is required to obtain higher energy density.

Figure 1.4 shows the voltage of $Li/Li_{1-x}NiO_2$ cells versus x for the first few cycles (Li, Reimers and Dahn, 1993). Lithium metal is used in test cells because it has a constant chemical potential during the whole range of charge and

discharge, so the electrochemical performance of the cathode can be analyzed. The electrolyte used in this cell is a 1 *M* solution of the salt $LiPF_6$ in equal volumes of propylene carbonate (PC) and ethylene carbonate (EC). As shown in figure 1.4, about 0.60 Li per Ni can be intercalated and deintercalated in $Li_{1-x}NiO_2$ to an upper cutoff voltage of 4.2 V . A high energy density rechargeable lithium cell can be made using $Li_{1-x}NiO_2$ as the cathode. The cell voltage is not constant during the charge and discharge, which means that the chemical potential of lithium in $Li_{1-x}NiO_2$ depends on lithium concentration, *1-x*. During lithium intercalation the lattice constants of $Li_{1-x}NiO_2$ change because the intercalated lithium interacts with neighboring host atoms and with neighboring lithium. The host lattice responds to such atom-atom interactions. In other words, the structure of the host is related to the electrochemical behavior observed during lithium intercalation. It is important to understand the structure of $Li_{1-x}NiO_2$ as a function of *x* in order to understand the electrochemical behavior. Furthermore, some intermediate, structurally related phases, can form during lithium intercalation and phase transitions can occur.

X-ray diffraction experiments are used to analyze crystal structures. In-situ X-ray diffraction, using electrochemical cells with beryllium x-ray windows (Dahn, Py and Haering) is used to understand the structural changes in intermediate compounds which occur during lithium intercalation. There are no easy experimental ways to measure the ion-ion interactions. However, there are some phenomenological models which can be used to theoretically predict the structures of materials. Both theoretical and experimental approaches can be used to understand the structural changes and therefore to understand lithium intercalation reactions. This thesis addresses these problems.

$LiMn_2O_4$ is one cathode choice for rechargeable lithium batteries. Figure 1.5 (Tarascon and Guyomard) shows voltages versus time for Li/$LiMn_2O_4$, Li/petroleum coke and petroleum coke/$LiMn_2O_4$ cells during the first few cycles. The latter cell is an example of a lithium-ion cell. The features in the voltage of the petroleum coke/$LiMn_2O_4$ cell combines those of the Li/$LiMn_2O_4$ and Li/petroleum coke cells. In other words, the voltage of petroleum coke/$LiMn_2O_4$ cell can be calculated by subtracting the voltage of the Li/petroleum coke cell from the Li/$LiMn_2O_4$ cell.

It is important to use inexpensive compounds for the positive electrode and the negative electrode in real applications. Graphite and petroleum coke are cheap. Mn is also cheap (US$ 1.50 per kg) and non-toxic compared with Ni and Co. $LiMn_2O_4$ is therefore a very good candidate for a cathode material. Recall that lithium ion cells have the lithium initially supplied by the cathode. $LiMn_2O_4$ has one disadvantage for use in these cells, that is Li:Mn=1:2, which is only half that found in $LiNiO_2$ or $LiCoO_2$. Using other lithium manganese oxides with high lithium to manganese ratio may overcome this problem. This thesis addresses this issue.

The spinel $Li_2Mn_2O_4$ has Li:Mn=1:1, which is larger than that of $LiMn_2O_4$. $Li_2Mn_2O_4$ shows promise as a cathode in the lithium rechargeable battery (Tarascon and Guyomard) . $Li_2Mn_2O_4$ can be made by reacting $LiMn_2O_4$ with LiI at about 150°C. Other methods include lithium intercalation into $LiMn_2O_4$ in a non-aqueous electrolyte (Ohzuku, Ueda and Nagayama). In the former method, LiI is involved, which makes volume manufacturing difficult because of the corrosive nature of iodine. In the second method, non-aqueous electrolytes and Li metal are used and therefore it is expensive to make $Li_2Mn_2O_4$. Other methods such as heating Li_2CO_3 with MnO_2 are not successful since spinel $Li_2Mn_2O_4$ is not stable at high temperature. Hence a

better method is required to make $Li_2Mn_2O_4$ before $Li_2Mn_2O_4$ can be considered as a cathode in a lithium-ion cell. This thesis addresses this problem.

Sony Energytec Inc. began to produce a lithium-ion cells in 1990 (Nagaura and Tozawa). Using $LiCoO_2$ as the cathode and carbon as the anode, Sony's lithium-ion cell has three times the total output energy of an "old-technology" nickel cadmium cell. Figure 1.6 (Nagaura and Tozawa) shows the discharge curves of D size lithium-ion and Ni-Cd cells. The capacities are about 4000 mAh for both chemistries. The average voltage of the lithium-ion cell is about three times larger than Ni-Cd.

One lithium-ion cell operating at high voltage can replace three Nd-Cd cells, therefore they are very convenient for applications requiring an operating voltage between 3 and 4 volts. Besides their high energy density, lithium ion cells can operate up to 1200 cycles (Nagaura and Tozawa) , which is significantly better than small Ni-Cd and Lead acid cells. The self discharge is 12 % after one month, which is less than that of Ni-Cd cells.

Non-aqueous electrolytes are required in lithium-ion cells. Non-aqueous electrolytes usually have ion conductivity two orders of magnitude lower than aqueous electrolytes. Therefore large anode and cathode areas are required to increase the cell power capability. A very thin separator is also necessary to decrease the cell impedance. These technical requirements increase the cost of rechargeable lithium cells. If rechargeable lithium-ion cells can be made using aqueous electrolytes, the cost of these cells will be significantly lower. Lithium-ion cells using aqueous electrolyte are also much safer than those using non-aqueous electrolyte, therefore large cells for electric vehicle applications can be easily made. This thesis addresses this issue.

There are many lithium intercalation compounds. Some of them are not air stable. Some of them contain only small amounts of lithium measured on a molar basis. The compounds used as cathode in lithium-ion cells must be air stable and have enough lithium inside. As shown in figure 1.3, many lithium transition metal oxides are air stable in the right chemical potential ranges and have enough lithium inside. Many of them are also intercalation compounds and therefore are suitable to be used as cathode materials. Since the first row transition metals are lighter than the other transition metals, their lithium metal oxides can provide higher specific energy than other compounds. Hence Li-*M*-O (*M*=Sc-Cu) compounds are the best option for cathodes in lithium-ion cells. **They are important and crucial materials**. Therefore, most of the work in this thesis is concentrated on lithium first-row transition metal oxides.

The structure of intercalation compounds is very important to their electrochemical performance. Hence in chapter 2, the structures of lithium transition metal oxides are described in detail. Rock salt related structures are introduced carefully since they are very common in lithium transition metal oxides and because they are the subject of theoretical work in this thesis. The structures of LiMO_2 (*M*=Sc-Cu) are also reviewed because many of these materials are now used as cathodes in rechargeable lithium batteries. Furthermore, other important structures of manganese compounds are described because they are related to one another and some of them are promising in rechargeable lithium battery applications.

In chapter 3, a lattice-gas-model is used to understand the structures of lithium transition-metal oxides LiMO_2. The $LiNiO_2$, layered $LiCoO_2$, spinel $LiCoO_2$, $Li_2Ti_2O_4$, and γ-$LiFeO_2$ structures are predicted for appropriate values

of first- (J_1) and second- (J_2) neighbor interactions within such a model by analogy with binary-alloy materials having similar structures. A J_1-J_2-T phase diagram is predicted and the allowable ranges for the interactions are assigned for each of the oxides above based on the phase diagram. A surprising result is obtained that the layered and spinel structures are equally stable over the same wide range of J_1 and J_2, as predicted by mean-field and Monte Carlo results. Using this theoretical result, the structures and the x-ray diffraction patterns of layered $LiCoO_2$ and spinel $LiCoO_2$ are successfully explained.

In chapter 4, the structure of $Li_{1-x}NiO_2$ is studied as Li is electrochemically deintercalated from $LiNiO_2$ with in-situ x-ray diffraction methods. A new modified in-situ x-ray cell design is described, which is suitable for reliable operation with high voltage cathodes like $Li_{1-x}NiO_2$. Using this cell in this thesis, the electrochemical behavior of $Li_{1-x}NiO_2$ is investigated during the x-ray diffraction measurement. Three hexagonal phases and one monoclinic phase are found within the composition range $0.0 \leq x \leq 0.82$. Three regions of x corresponding to two-phase coexistence are also obtained. This new modified in-situ x-ray cell, has been used to investigate the structure of $LiNiVO_4$, which is the highest voltage cathode among known lithium intercalation compounds.

In chapter 5, lithium intercalation from aqueous solutions is investigated. It is proved in this thesis that lithium can be intercalated into host compounds from aqueous LiOH solution, provided the chemical potential of the intercalated lithium is sufficiently lower than the chemical potential of lithium in lithium metal. $Li_2Mn_2O_4$ can be made by intercalating Li from LiOH solution into $LiMn_2O_4$ in an aqueous cell. Other lithium transition metal oxides like γ-$LiMnO_2$, which are difficult to make by other methods, can

also be made by this new method. This method may prove to be an economical way of preparing lithium transition metal oxides with high lithium contents for lithium-ion cell cathodes.

In chapter 6, rechargeable lithium-ion cells are made using an aqueous electrolyte. This development is based on the understanding of lithium intercalation from aqueous solutions. When the electrode materials are properly selected, water-based electrolytes can be used in lithium-ion cells. Such a discovery leads to a fundamentally safe and inexpensive technology. Test cells using $LiMn_2O_4$ and $VO_2(B)$ as electrodes and 5M $LiNO_3$ in water as electrolyte can compete on energy basis with nickel-cadmium and lead-acid cells.

Finally, a summary and outlook is given in chapter 7.

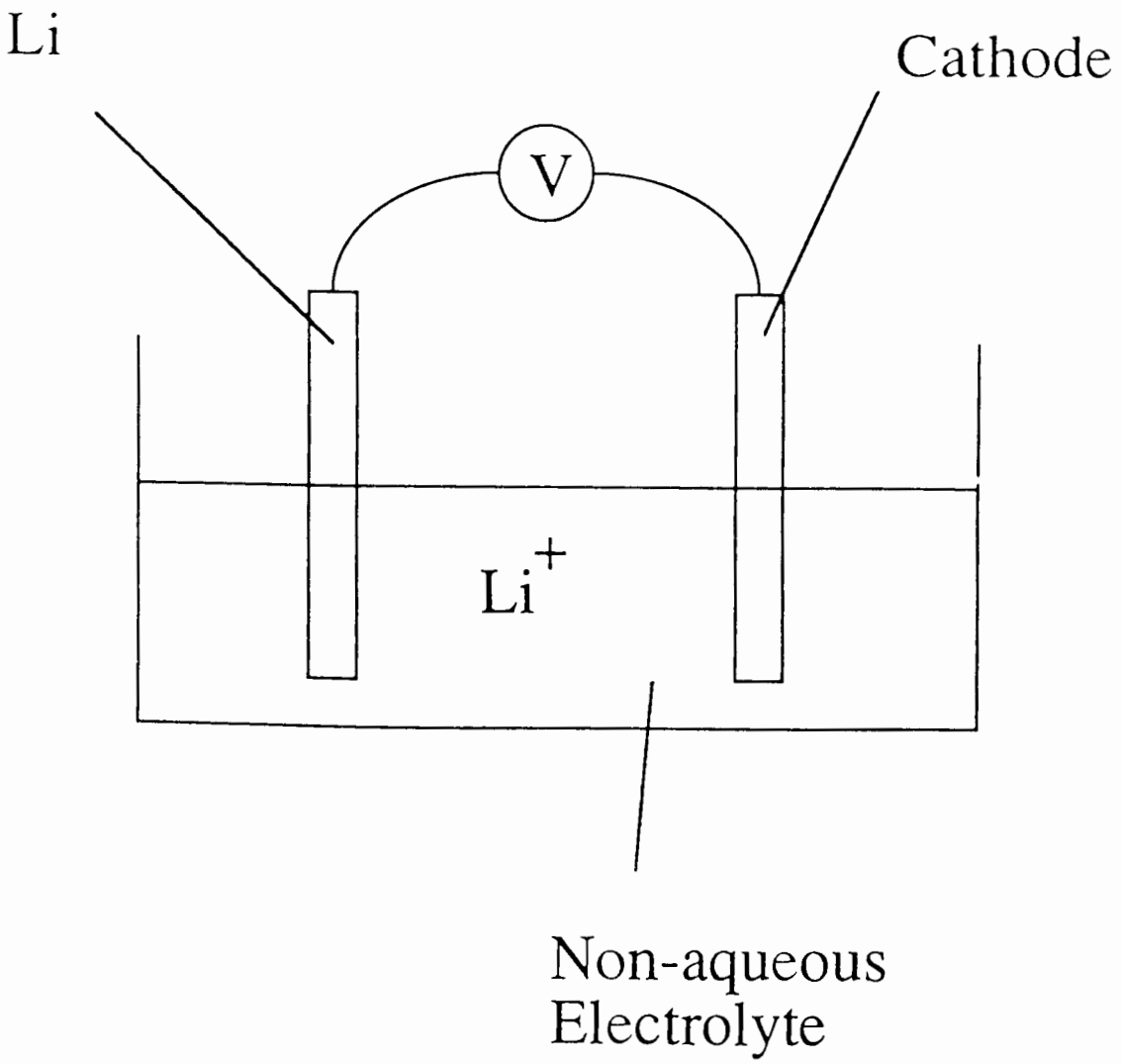

Figure 1.1. Schematically showing a lithium cell.

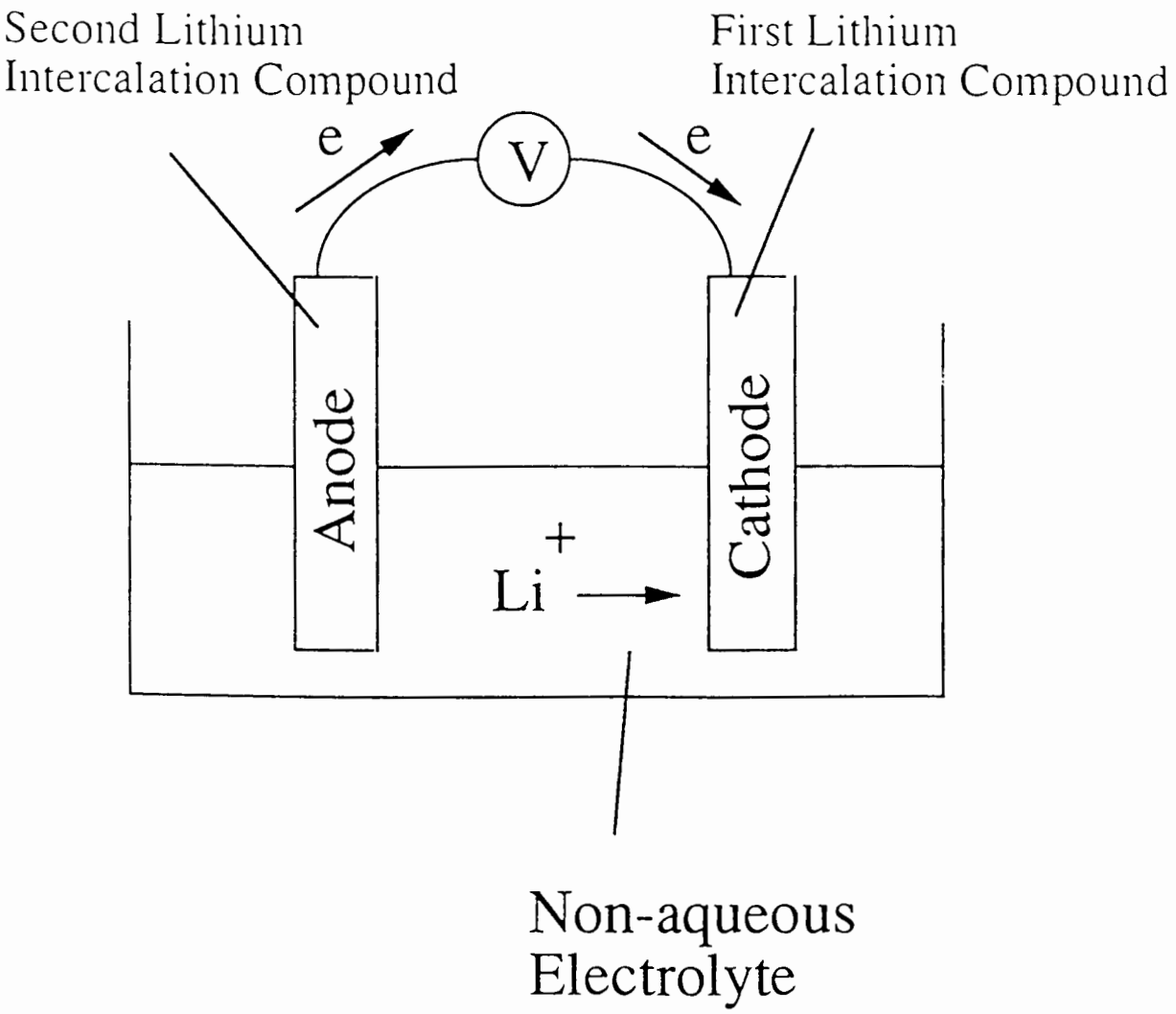

Figure 1.2. Schematically showing the discharge of a rocking chair or Li-ion cell.

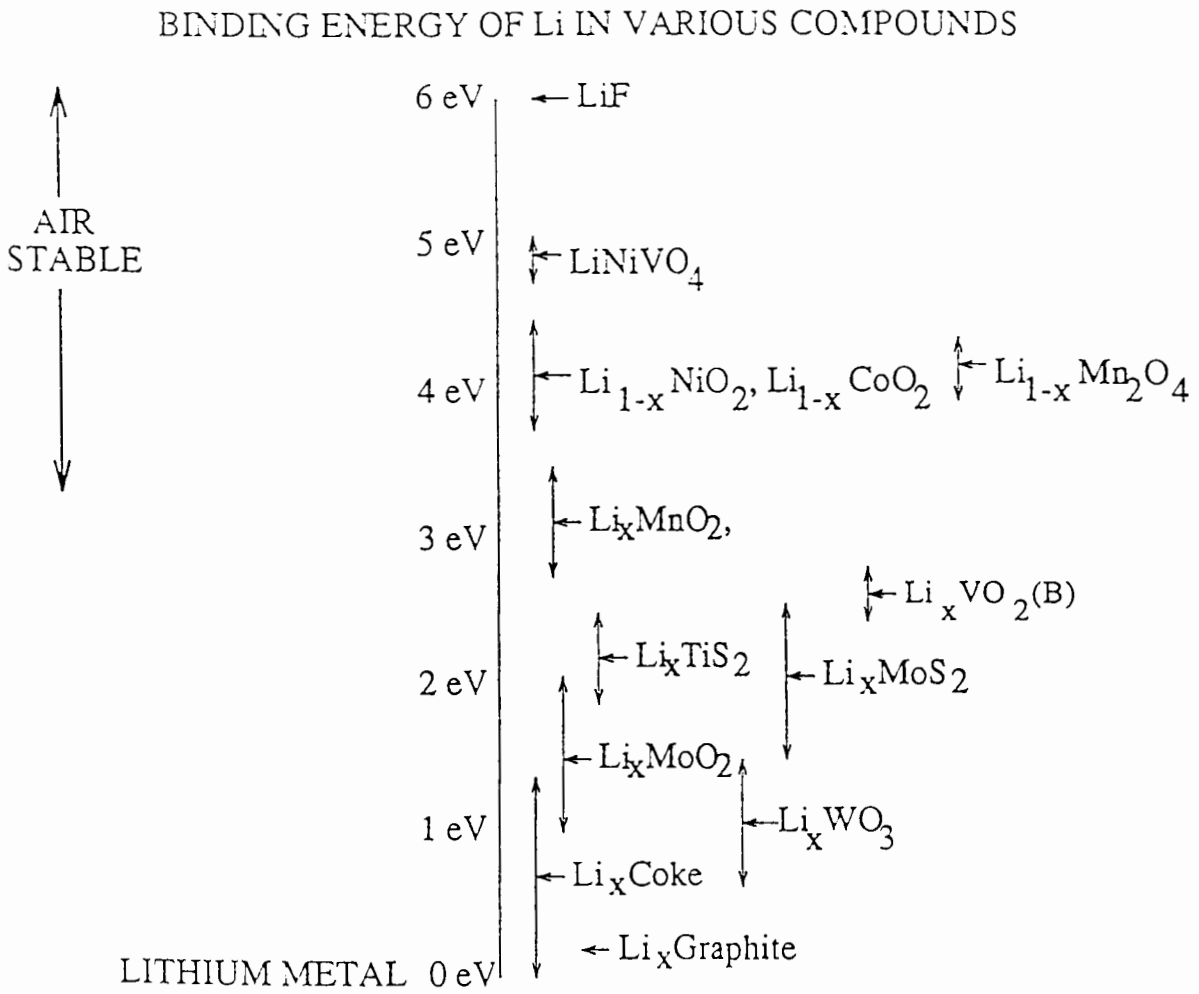

Figure 1.3. The binding energy of Li intercalated within a variety of materials, measured relative to that of Li metal.

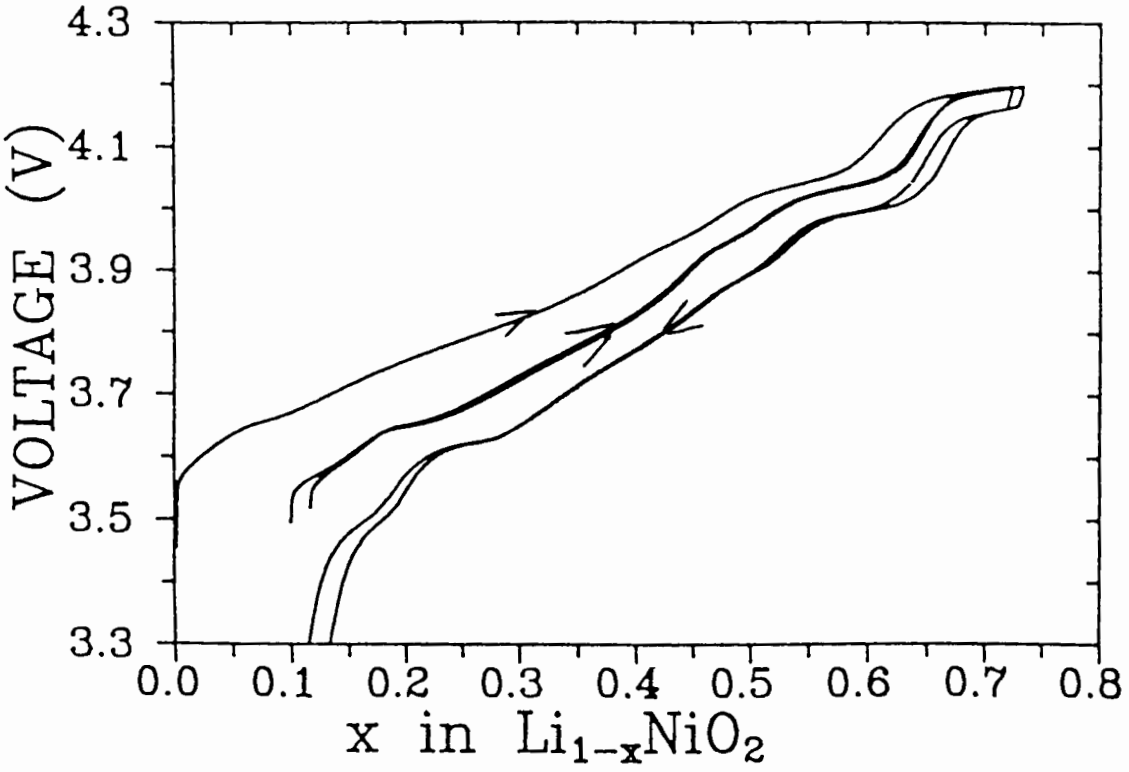

Figure 1.4. The charge and discharge curves as measured in a $Li/LiNiO_2$ coin cell for the first two cycles. A 100 hour rate (Δx=1 in 100 hours) was used at 30°C.

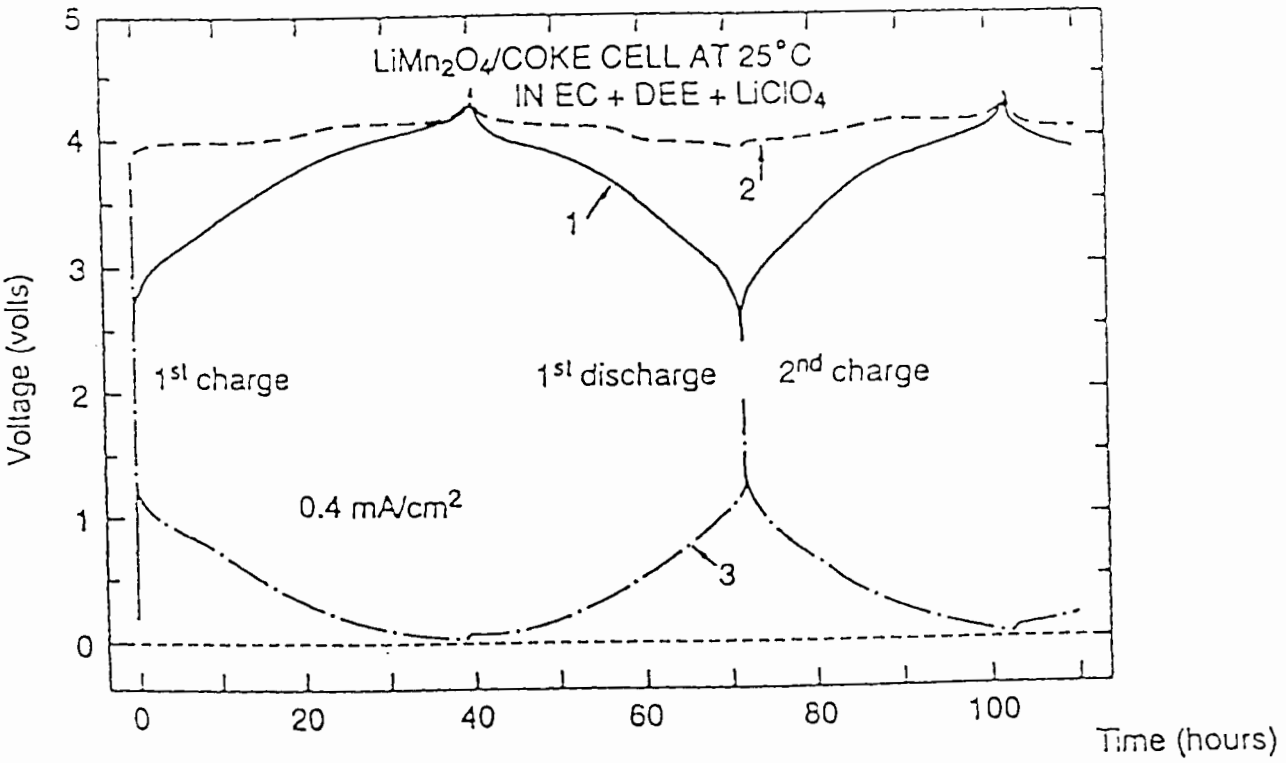

Figure 1.5. The charge and discharge curves as measured in a three-electrode cell at room temperature. The voltages denoted 1, 2 and 3 correspond to the voltage between $LiMn_2O_4$ and petroleum Coke, $LiMn_2O_4$ and Li metal, Li and petroleum coke respectively (From Tarascon and Guyomard).

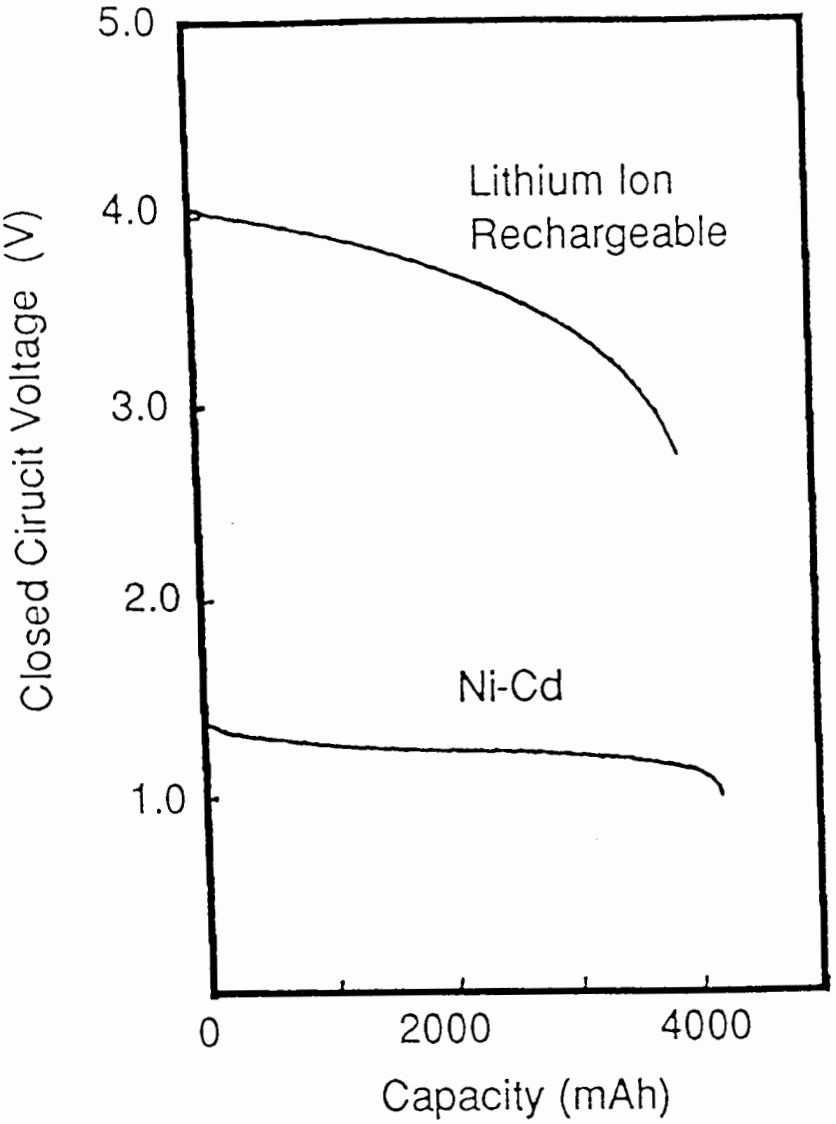

Figure 1.6. Discharge Curve of D size Cells with a 800mA discharge current (Nagaura and Tozawa).

Chapter 2. Lithium Transition Metal Oxides

2.1 Rock-Salt Related Structures

Many lithium transition metal oxides have structures derived from the perfect or distorted rock-salt structures (NaCl and NiO are examples of rock salt structure compounds). Figure 2.1 shows the rock-salt structure in which there are two fcc sublattices. Cations occupy one fcc sublattice and anions occupy the other fcc sublattice. As shown in figure 2.1 this structure can also be described as an fcc anion lattice with cations filling the octahedral interstices. In the rock-salt structure, the numbers of cations and anions are equal. Lithium transition metal oxides ($LiMO_2$, M=Sc-Cu) with the rock-salt structure also have equal numbers of cations and anions; the cations share one of the fcc sublattices and the anions occupy the other fcc sublattice. The particular arrangement of the cations on the cation lattice distinguishes the different crystal structures of these materials. Four common $LiMO_2$ structures, including layered $LiNiO_2$, spinel (or atacamite) $Li_2Ti_2O_4$, γ-$LiFeO_2$ and orthorhombic $LiMnO_2$, are introduced in the following.

$LiNiO_2$ has space group R 3m and a hexagonal (or rhombohedral) structure based on a slightly distorted fcc oxygen lattice. Li and Ni cations are arranged into layers on alternating $(111)_C$ (cubic) planes of cation sites. This structure is called the layered structure. Figure 2.2a shows the layered structure represented by close-packed oxygen octahedra (Reimers, Li, Rossen and Dahn). White octahedra have Li at the center and black octahedra have Ni (or M) at the center. Li, Ni and O are in the sites labelled 3a, 3b and 6c respectively of the space group R 3m (Wyckoff). Figure 2.2b shows the atom

positions of $LiNiO_2$ in hexagonal axes. The $LiNiO_2$ unit cell is indicated with the thick lines in figure 2.2b.

$Li_2Ti_2O_4$ has space group Fd3m and a cubic structure based on fcc oxygen. Lithium and titanium atoms are segregated into the 16c and 16d octahedral sites while oxygen occupies the 32e sites. The structure of $Li_2Ti_2O_4$ is called the spinel here (or more correctly called atacamite by Hewston and Chamberland). Figure 2.3a shows the spinel structure with close-packed oxygen octahedra (Gummow, Liles and Thackeray). White octahedra and black octahedra correspond to those occupied by Li or Ti atoms respectively. Figure 2.3b shows the atom positions in a unit cell of $Li_2Ti_2O_4$. It is hard to find any similarity between the cation arrangement in the layered and the spinel structures using figures 2.2 and 2.3.

γ–$LiFeO_2$ has space group $I4_1/amd$ and a tetragonal structure with cations arranged differently from both the spinel and the layered structures. Figure 2.4a shows the structure of γ-$LiFeO_2$ represented by close-packed oxygen octahedra. White octahedra have Li at the center and black octahedra have Fe at the center. Figure 2.4b shows the atom positions of γ-$LiFeO_2$ in a tetragonal unit cell (Hewston and Chamberland). In this structure oxygen arrangement is also based on the distorted fcc lattice and cations are arranged along the $(110)_C$ lines. Fe, Li and O occupy 4a, 4b and 8e sites, respectively (Wyckoff).

Orthorhombic $LiMnO_2$ has a space group Pmnm . $LiMnO_2$ is also based on the distorted rock-salt structure and with a larger distortion (14 %) than $LiNiO_2$ and γ-$LiFeO_2$. Figure 2.5a (Gummow, Liles and Thackeray) shows the structure of the orthorhombic $LiMnO_2$ by close-packed oxygen octahedra. White octahedra have Li at the center and black octahedra have Mn at the center. Figure 2.5b shows the atom positions of $LiMnO_2$ in an orthorhombic unit cell. The cation arrangement of $LiMnO_2$ is clearly different from those of

$LiNiO_2$, $Li_2Ti_2O_4$, γ-$LiFeO_2$. Li and Mn occupy 2a sites with parameters (1/2, 0.6347, 1/2) and (1/2, 0.126, 1/2), respectively (Hoppe, Brachtel and Jansen). Oxygen occupy 2b sites with O(1) in (1/2, 0.144, 1/4) and O(2) in (1/2, 0.602, 3/4). It is very difficult to find any similarities between the structures of $LiNiO_2$, $Li_2Ti_2O_4$, γ-$LiFeO_2$ and the orthorhombic $LiMnO_2$ from figures 2.2-2.5 based on the literature. This underscores the limitations of the space group formalism for describing complex structures!

Since $LiNiO_2$, $Li_2Ti_2O_4$, γ-$LiFeO_2$ and $LiMnO_2$ are all based on the perfect or distorted rock-salt structures, their oxygen atoms are basically found on an fcc lattice. To emphasize, the oxygen atom positions are almost the same in each of these materials. Only the cation arrangements in the cation sites differ. Now we consider the cation arrangements in these structures. Figure 2.6 (Li, Reimers and Dahn) shows the cation structures of spinel (atacamite) $Li_2Ti_2O_4$ (figure 2.6a), layered $LiNiO_2$ (figure 2.6b), γ-$LiFeO_2$ (figure 2.6c) and orthorhombic $LiMnO_2$ (figure 2.6d). The unit cell of spinel $Li_2Ti_2O_4$ consists of a 2x2x2 cubic supercell of the basic fcc primitive cell. The layered $LiNiO_2$ structure, the γ-$LiFeO_2$ structure and the $LiMnO_2$ structure are also shown on the same 2x2x2 supercell, respectively. Each of the latter three structures can be described with a smaller unit cell, which we (Li, Reimers and Dahn) have indicated in figure 2.6. When the structures are described with their conventional cells, the close structural relationship between the phases is not obvious. By showing the four structures on the same 2x2x2 super cell we show the similarities between them. For example, $LiMnO_2$, $LiNiO_2$, and $Li_2Ti_2O_4$ are made up of [001] planes of identical structures with cation rows parallel to <110>. The structures only differ in the stacking sequence and rotation of the planes. All these structures are based on the rock-salt structure and the differences among them are only in the cation arrangement,

therefore a lattice gas model can be used to understand these different cation arrangements. The details of such a theory will be discussed in chapter 3. In section 2.2 we review the $LiMO_2$ materials and in section 2.3 we describe other important structures. Application of these materials in batteries is described in section 2.4.

2.2 Review of Known Rock-Salt Type $LiMO_2$ Structures

Hewston and Chamberland reviewed the first-row ternary oxides $LiMO_2$. Most of these compounds take one of the four structures introduced above in section 2.1.

$LiScO_2$ was first reported by Hoppe in 1959. X-ray diffraction studies showed that $LiScO_2$ has a tetragonal NaCl superstructure and a space group $I4_1/amd$. The unit cell parameters are a=4.18 Å and c=9.30 Å. The cation arrangement is the same as that in γ-$LiFeO_2$.

$LiTiO_2$ has two structures. The first one was reported by Bongers in 1957. X-ray diffraction studies (Bongers) indicate that $LiTiO_2$ has a fully disordered cubic rock-salt structure and a=4.140Å. Li and Ti are distributed equally and randomly on the cation sites. The second form of $LiTiO_2$ was prepared by lithiation of the spinel $LiTi_2O_4$ using the intercalation agent n-butyl lithium (Cava, Murphy, Zahurak, Santoro and Roth). This is what is described in former section as the spinel $Li_2Ti_2O_4$ with a=8.376 Å. Metastable $Li_2Ti_2O_4$ transforms irreversibly to the disordered rock-salt structure above 600°C.

$LiVO_2$ has two structures. One of the structures is hexagonal and has the same cation arrangement as $LiNiO_2$ (a=2.84Å and c=14.7 Å) (Rudorff and Becker). The second structure of $LiVO_2$ is cubic and has a rock-salt superstructure, with the same cation arrangement as $Li_2Ti_2O_4$ (a=8.227Å). This spinel structure was prepared by using high pressure methods (Chieh, Chamberland and Wells). One may wonder why the same compound should be stable in two different crystal forms. We return to this point in chapter 3.

$LiCrO_2$ was first reported by Rudorff and Becker. $LiCrO_2$ has the hexagonal structure and the same cation arrangement as $LiNiO_2$. The lattice constants are a=2.88Å and c=14.6Å.

$LiMnO_2$ has three structures. The first structure is reported with an orthorhombic unit cell (Johnston, Heikes) as described in the former section. A Jahn-Teller effect was found in this structure.

Jahn-Teller distortions are explained by crystal field theory. Any non-linear molecular system in a degenerate electronic state will be unstable and will undergo distortion to form a system of lower symmetry and lower energy, thereby removing the degeneracy (Sharpe). In an octahedral field, d orbitals are split into two different energy groups. One is composed of d_{xy}, d_{yz}, d_{xz} and the other is composed of $d_{x^2-y^2}$ and d_{z^2} . When d_{z^2} and $d_{x^2-y^2}$ are unequally populated in stable species, the interactions along the z direction are different from those in the x-y plane, and the distortions appear. Jahn-Teller distortions mostly appear in d orbital species because the energy splitting of d orbitals is much larger than that of f orbitals. The distortions origining from f orbitals are very small. On the other hand, it is very rare for the p orbital to be unequally populated (especially in transition metal oxides), so the p orbitals are not important for Jahn-Teller distortions. There are only three electrons in d orbitals for Mn^{+4} and these electrons occupy d_{xy}, d_{yz} and d_{zx} orbitals. There are four electrons in d orbitals for Mn^{+3} and one electron occupies the d_{z^2} orbital. So $LiMnO_2$ structures which have Mn^{3+} usually have Jahn-Teller distortions.

The second structure of $LiMnO_2$ was prepared by chemical lithiation of the spinel $LiMn_2O_4$ to make $Li_2Mn_2O_4$ (Thackeray, David, Bruce and Goodenough). $Li_2Mn_2O_4$ has a tetragonal unit cell (a=5.662Å and c=9.274 Å) and a rock-salt superstructure. The cation arrangement is the same as that in $Li_2Ti_2O_4$. But $Li_2Mn_2O_4$ is not cubic because of a Jahn-Teller distortion. The third structure has been prepared at 65 kbar and 1000°C from the

orthorhombic phase $LiMnO_2$. This phase has the statistical distorted rock-salt structure (a=4.166Å) (Hewston and Chamberland).

$LiFeO_2$ has three structures. α-$LiFeO_2$ has the statistically disordered rock-salt structure (a=4.158Å) (Anderson and Schieber). γ-$LiFeO_2$ is tetragonal as described in section 2.1. The structure of β-$LiFeO_2$ is not well understood. It seems that β-$LiFeO_2$ has a metastable structure between the other two polymorphs. A body centered tetragonal unit cell was suggested for β-$LiFeO_2$.

$LiCoO_2$ was first reported by Bongers. The structure is rock-salt related with the hexagonal layered superstructure (a=2.81 Å and c=14.0 Å). The cation arrangement is the same as that in $LiNiO_2$. Recently a second compound with the same stoichiometry $Li_2Co_2O_4$, was reported (Rossen, Reimers and Dahn). This structure also has the rock-salt related structure and the cation arrangement is the same as that in $Li_2Ti_2O_4$.

$LiNiO_2$ has the layered structure and is hexagonal (a=2.878 Å and c=14.19 Å) (Dyer, Borie and Smith) as described in the former section. The c/a ratio is 4.93, which is just slightly different from 4.90 for the perfect cubic structure.

There are no reports of $LiCuO_2$, although the larger alkali metal analogs $NaCuO_2$, $KCuO_2$, $RbCuO_2$ and $CsCuO_2$ are known (Hestermann and Hoppe).

2.3 Other Important Structures

$LiMn_2O_4$, is cubic and has a space group Fd3m and a=8.240 (Ohzuku, Kitagawa and Hirai). $LiMn_2O_4$ also has the true spinel structure with each Li tetrahedrally surrounded by four oxygens and each Mn octahedrally surrounded by six oxygens. The Mn and O atoms are in the same positions as the Ti and O atoms in spinel $Li_2Ti_2O_4$. Figure 2.7 shows the structure (Thackeray et al.) of $LiMn_2O_4$. In this structure, three dimensional tunnels are formed as shown in figure 2.7, and the Li is located on 8a sites within the tunnels. When further lithium is intercalated into these tunnels, $Li_2Mn_2O_4$ is obtained and the structure distorts from cubic to tetragonal because of the Jahn-Teller effect as described in section 2.2. When lithium is deintercalated from $LiMn_2O_4$, λ-MnO_2 is obtained. The positions of oxygen and manganese do not change significantly from $LiMn_2O_4$. λ-MnO_2 (a=8.04 Å) also has cubic close-packed oxygen and has manganese arranged as shown in figure 2.6a with the black sites full and the white sites empty.

β-MnO_2 is tetragonal and has space group P4/mmm with a=4.396Å and b=2.871Å. β-MnO_2 has a distorted hexagonal closed packed (hcp) oxygen lattice. Figure 2.8 shows the structure of β-MnO_2. In this structure, "1x1" tunnels are formed. Mn occupies 2a sites and O occupies 4f sites (Wyckoff).

Ramsdellite-MnO_2 is orthorhombic and has space group Pbnm. Ramsdellite-MnO_2 also has a distorted hexagonal close packed oxygen lattice. Figure 2.9 shows the structure of Ramsdellite-MnO_2 (Glover, Schumm., Kozawa and Kozawa). In this structure, only "1x2" tunnels are found. Mn, O(1) and O(2) all occupy 4c sites $\pm$[u,v,1/4; 1/2-u, v+1/2,1/4] with parameter u=-0.036, v=0.140 for Mn, u=0.27, v=-0.20 for O(1), and u=-0.21, v=-0.05 for O(2) (Wyckoff).

EMD (Electrolyte Manganese Dioxide) is normally γ-MnO_2. γ-MnO_2 is an important material. It is used as the cathode for Zn/MnO_2 primary cells, such as the Eveready Energizer and the Duracell Alkaline cells. Figure 2.10 shows the structure of γ-MnO_2. In this structure, 1x1 and 1x2 tunnels are mixed more or less randomly together. The proportions of 1x1 and 1x2 tunnel structures in EMD can be varied, depending on the synthesis conditions.

γ-Li_xMnO_2 has a structure similar to γ-MnO_2. The manganese and oxygen in γ-Li_xMnO_2 are located in the same position as in γ-MnO_2 except for a slight distortion. Lithium then occupies the tunnel sites as shown in figure Figure 2.10. Figure 2.11 (Thackeray et al.) shows the structures of Ramsdellite-MnO_2 and γ-$Li_{0.9}MnO_2$

2.4 Applications in Batteries

Lithium transition metal oxides, Li-M-O (M=Sc, Ti, V, Cr, Mn, Fe, Co, Ni, Cu) have been studied as cathodes in lithium rechargeable batteries since the 1970's (Desilvestro and Haas). All the first row transition metals have more than one common oxidation state, which is apparently a requirement for lithium intercalation in their oxides.

Titanium oxides have been studied as cathode materials. $Li_{4/3}Ti_{5/3}O_4/Li$ cells have a voltage plateau at 1.6V versus Li metal and show a very good cycling life (Ohzuku and Ueda). Theoretical capacity is calculated to be 175 mAh/g. Practical capacity is about 160 mAhr/g.

Vanadium oxides have been studied extensively as cathode materials. The common vanadium oxides and lithium vanadium oxides include V_2O_5, V_6O_{13} and LiV_3O_8. The crystalline form of V_2O_5 shows several steps in $V(x)$ during the intercalation of Li in $Li/Li_xV_2O_5$ cells. A limiting composition of $Li_3V_2O_5$ can be formed, which corresponds to a charge density of 440 mAhr/g. Primary Li/V_2O_5 cells have theoretical energy densities up to 650 mWhr/g during slow discharge (Voorn). However, good cycling behavior is observed only if x in $Li_xV_2O_5$ is limited to less than about 1 (Sakurai, Okada, Yamaki and Okada). $Li_{1+x}V_3O_8$ can also be used as a cathode material for Li cells (Nassau and Murphy). Three more lithium atoms can be intercalated in every LiV_3O_8 unit using butyllithium (Paner, Pasquali and Pistoia). The theoretical value of the charge density is 280 mAhr/g for Li/LiV_3O_8 cells. The disadvantages of these cells include low electronic conductivity for the oxide and high oxidizing capability which may result in electrolyte decomposition (Pistoia, Pasquali, Tocci, Manev and Moshtev). V_6O_{13} was used as cathode material by Murphy et. al (Murphy, Christian, DiSalvo and Carides). Each

V_6O_{13} unit can accommodate up to 8 Li. However, it appears that only six Li can be inserted reversibly in V_6O_{13} (Abraham, Goldman and Dempsey). The discharge profile is divided into three main steps corresponding to the consecutive transfer of one, three, and four electrons. V_6O_{13} is practically insoluble in organic solvents in comparison to V_2O_5. This gives a low self-discharge rate and good shelf life. VO_2(B) is yet another intercalation compound, Li/VO_2(B) cells have a single voltage plateau at 2.6 V and have a practical specific capacity of 140 mAhr/g (Dahn, Buuren and von Sacken).

MnO_2 is the most popular cathode material for galvanic cells since it is cheap and has reasonable capacity and electrode potential. Currently eight billion primary zinc/manganese dioxide cells are produced each year (Kordesch, Harer, Taucher, Tomantscher). MnO_2 has been investigated as a cathode material in primary Li cells since the 1970's. Such Li/MnO_2 primary cells are now widely produced for camera applications. Sony used to produce prototype secondary Li batteries based on γ-MnO_2. These AA cells offered very high practical energy densities of 125 Wh/kg and 240 Wh/l at discharge rates of C/2.5h (sufficient to discharge the entire capacity in 2.5 hours) with an average voltage of 2.8 V. It is claimed that these cells can achieve 1000 recharge cycles (Desilvestron and Haas). Self-discharge is low, at about 1 % per month. However, there are still some serious safety problems to solve before these cells can be really successful products (Battery&EV Technol). Moli Energy's Li/γ-MnO_2 cells (Molicel) were similar in performance to the Sony cells.

Another important MnO_2 is λ-MnO_2, which has the spinel structure as described in the section 2.3. Li/λ-MnO_2 cells have an average voltage of 4.0V

(Hunter). Tarascon and Guyomard reviewed $Li_{1-x}Mn_2O_4$ /C Li-ion rechargeable battery systems.

γ-Li_xMnO_2 is also an important material as cathode in lithium rechargeable cells. Li/γ-Li_xMnO_2 cells show good capacity and cycle life (Nohma, Yamamoto, Nishio, Nakane and Furukawa).

Recently, a new orthorhombic $LiMnO_2$ was prepared by reacting γ-MnOOH and $LiOH{\cdot}H_2O$ at 350°C. Li/$LiMnO_2$ cells show a reversible specific capacity of 190 mAh/g between 2.5 and 4.2 V (Ohzuku, Ueda and Hirai). Orthorhombic $LiMnO_2$ prepared by ion exchange between LiOH and γ-MnOOH also shows similar cell performance (Reimers, Fuller, Rossen and Dahn).

Li/Li_xCoO_2 cells provide an open circuit voltage as high as 4.7 V for x=0.07 (Mizushima, Jones, Wiseman and Goodenough). Theoretical energy densities of 1070Whkg^{-1} can be obtained based on $\Delta x=1$ and an average discharge voltage of 3.9 V. But the high discharge voltage and oxidizing power of Li_xCoO_2 can degrade the electrolyte, forming polymeric films on the electrode surface (Thomas, Bruce and Goodenough), and corroding the underlying metal support. Nevertheless, at least two companies (Sony) and (A&T Battery) are now exploiting the highly promising characteristics of $LiCoO_2$ for practical rechargeable Li-ion batteries (Nagaura and Tozawa; Kuribayashi).

Nickel oxides are a successful cathode material in commercial secondary cells. Ni/Cd cells are now used world-wide and their sales have reached US$ 1.3 billion per year. Even though nickel oxide has been considered as a cathode material in alkaline cells since 1887 (Falk and Salkind) their electrochemistry is not yet fully understood (Huggins). Lithium nickel oxide has also been used as a cathode material in lithium-ion rechargeable cells

(Dahn, von Sacken, Juzkow and Al-Janaby). The $LiNiO_2/C$ cells have high energy density, long cycle life, and low self-discharge rates.

As we will show later, the electrochemical performance of cathode materials strongly depends on the their crystal structures. It is therefore important to understand the structures of lithium transition metal oxides. In the next chapter, a lattice gas model is used to understand the rock-salt related $LiMO_2$ structures.

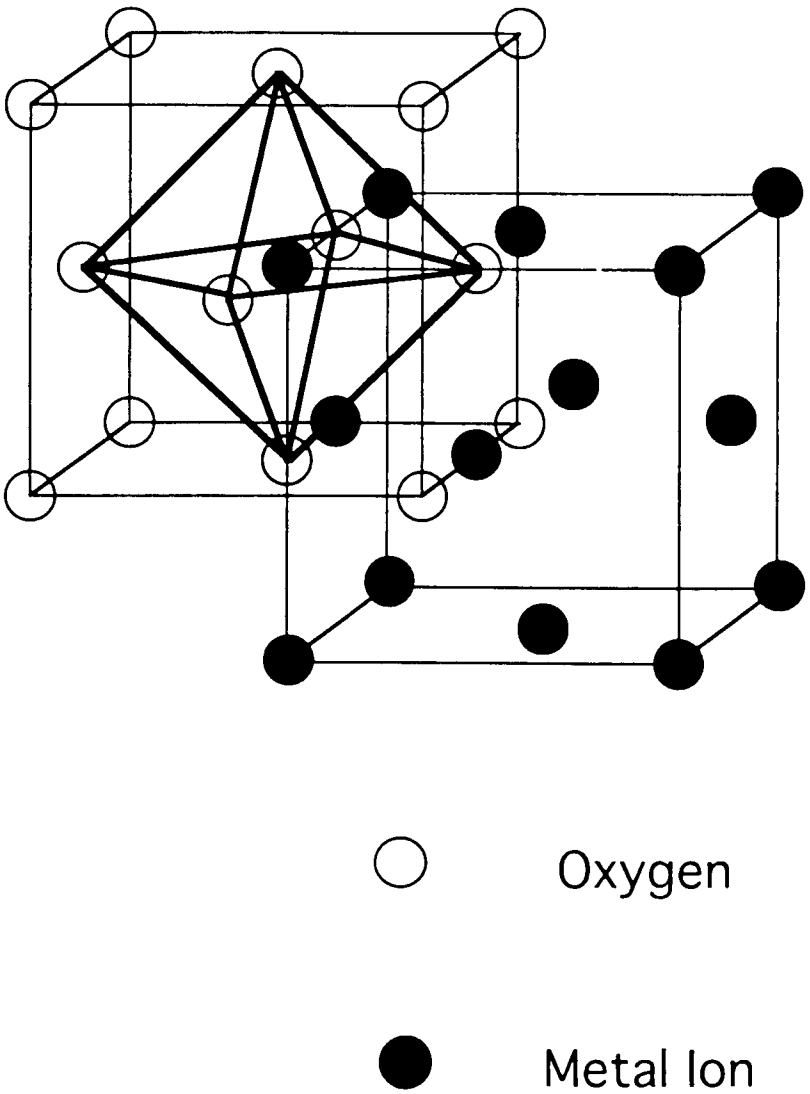

Figure 2.1 The rock-salt structure with cation (black) occupying one fcc sublattice and anions (white) occupying the other fcc sublattice. The thick lines show an octahedron.

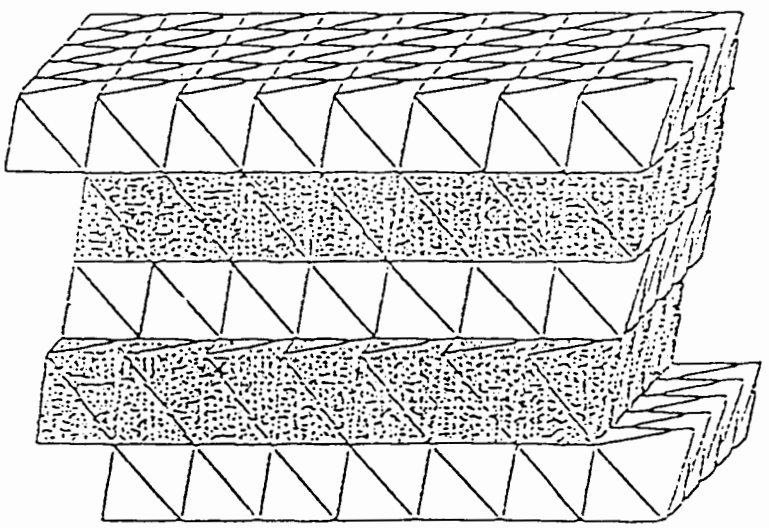

Figure 2.2a. The layered structure represented by close-packed oxygen octahedra. Li occupys the octahedral interstices in white layers and transition metal occupys the octahedral interstices in black layers (Thackeray et. al).

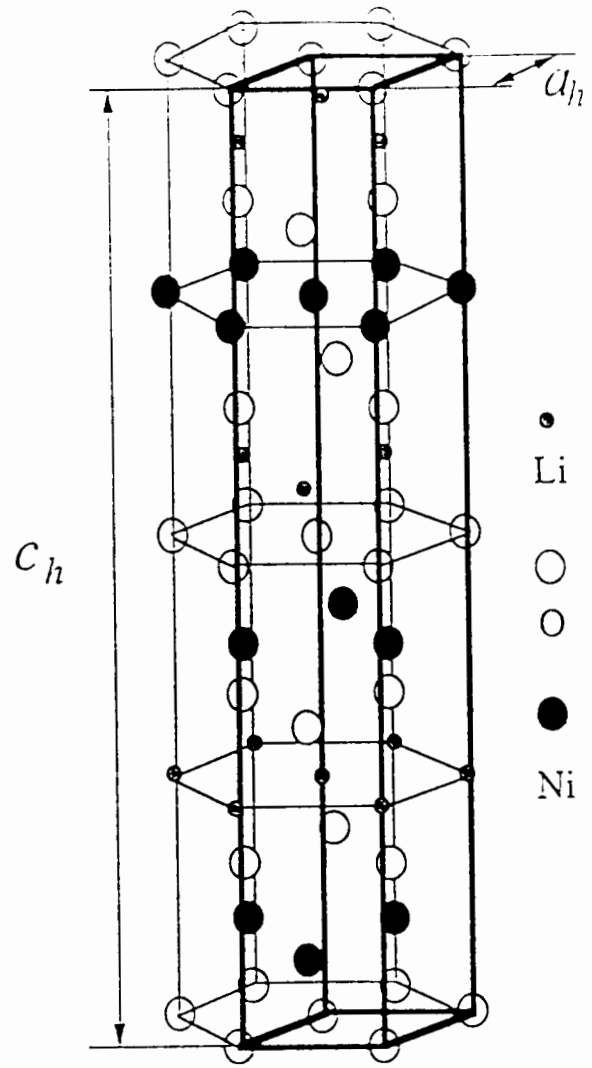

Figure 2.2b. Crystal structure of $LiNiO_2$ as one example with the layered structure.

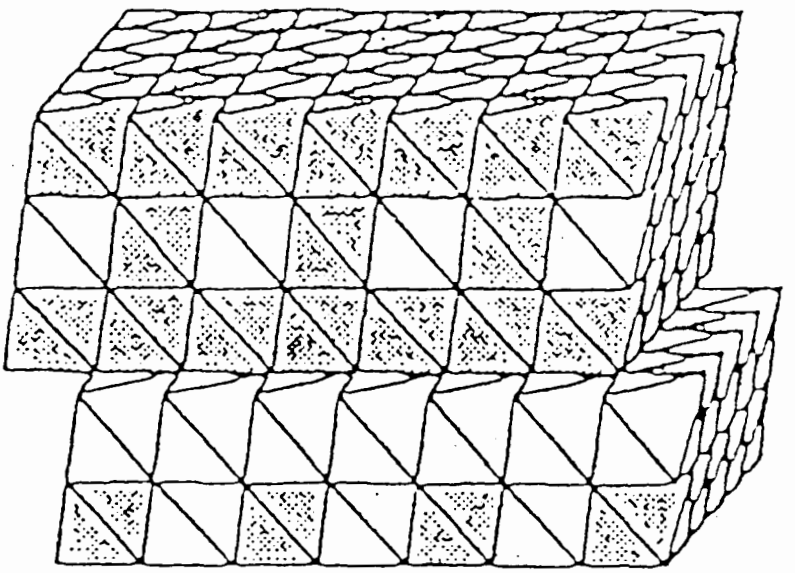

Figure 2.3a. The spinel (or atacamite) structure with close packed oxygen octahedra. Li occupys the octahedral interstices in white layers and transition metal occupys the octahedral interstices in black layers (Gummow, Liles and Thackeray).

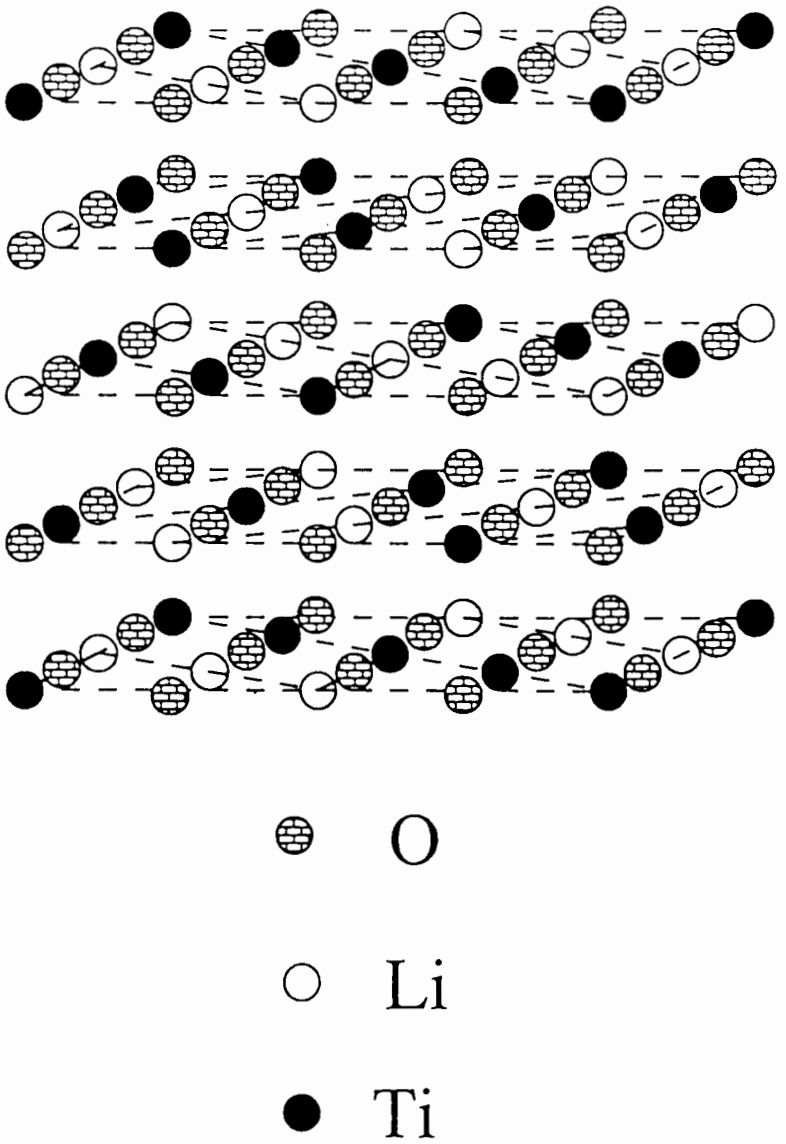

Figure 2.3b. Crystal structrue of $Li_2Ti_2O_4$ as one example with the spinel (atacamite) structure.

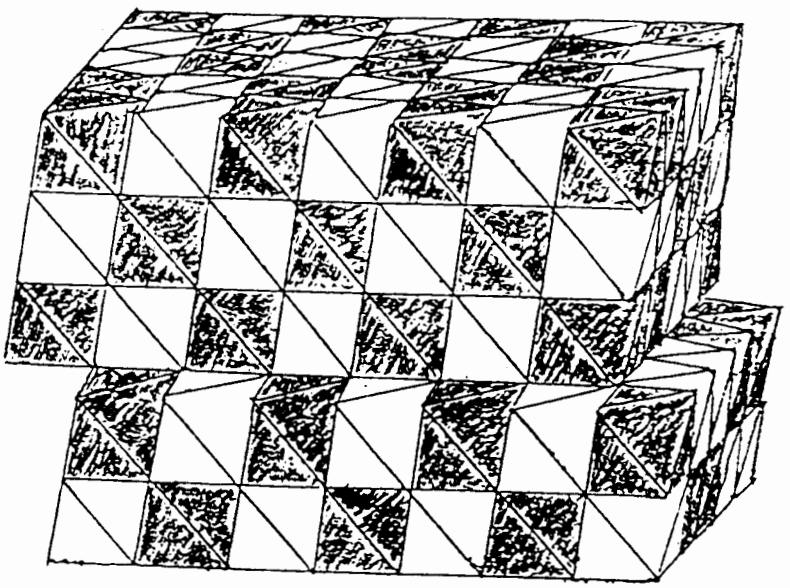

Figure 2.4a. Crystal structure of γ-$LiFeO_2$ represented by close-packed oxygen octahedra.

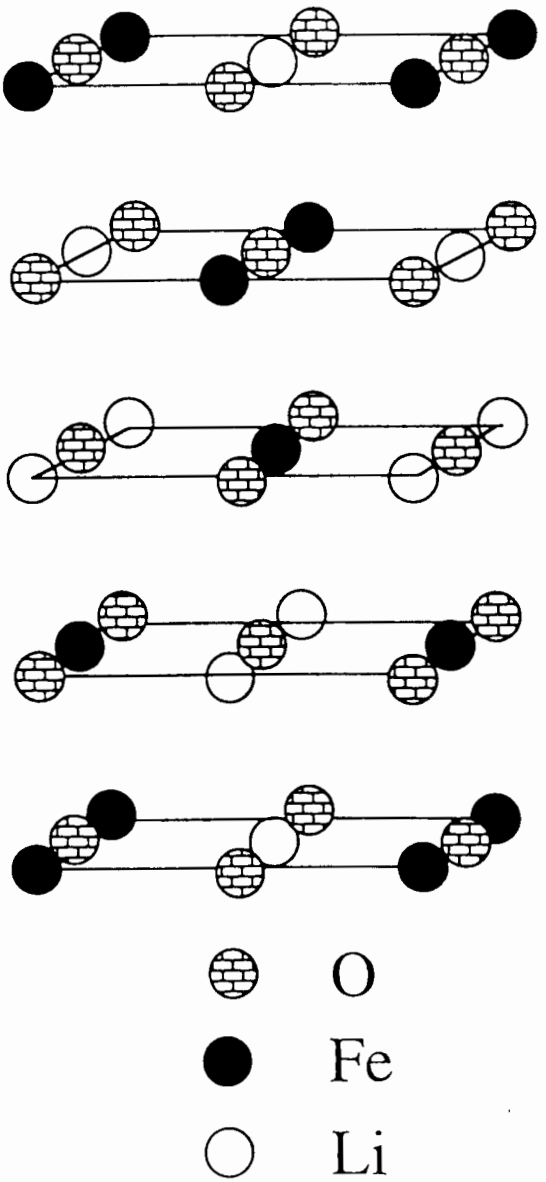

Figure 2.4b. Crystal structure of γ–$LiFeO_2$ in a tetragonal unit cell. (After Hewston and Chamberland).

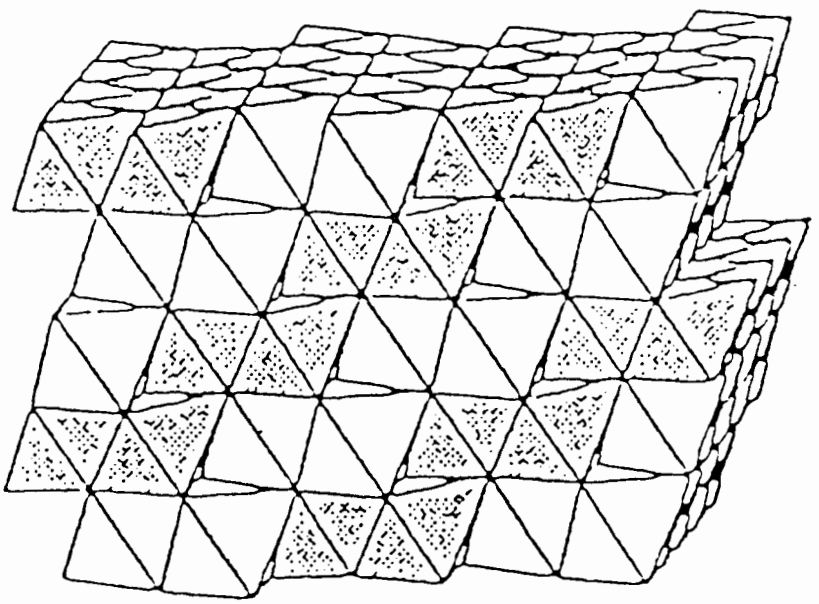

Figure 2.5a. Crystal structure of the orthorhombic $LiMnO_2$ represented by close-packed oxygen octahedra (Gummow, Liles and Thackeray).

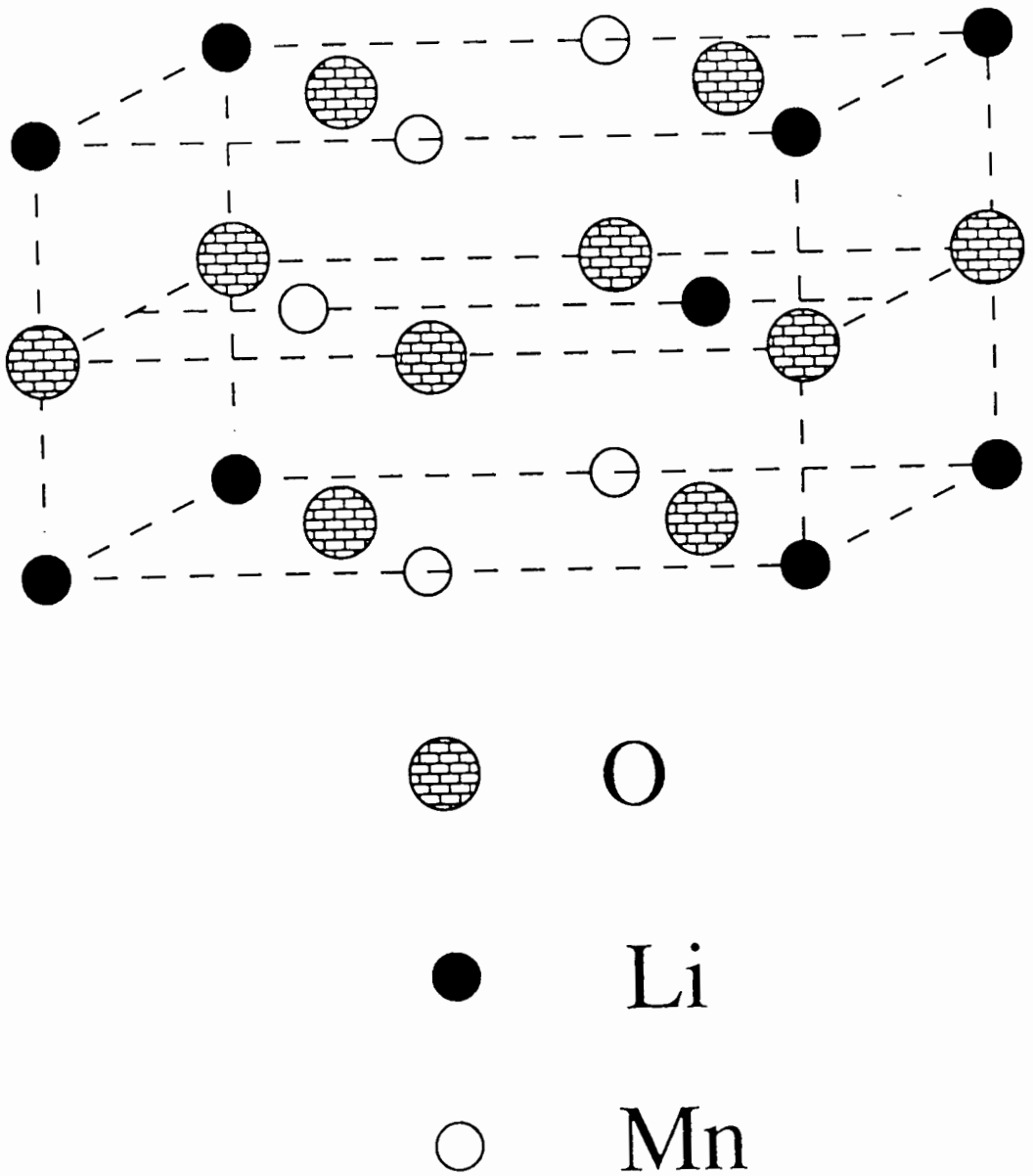

Figure 2.5b. Crystal structure of orthorhombic $LiMnO_2$ (After Hoppe, Brachtel and Jansen).

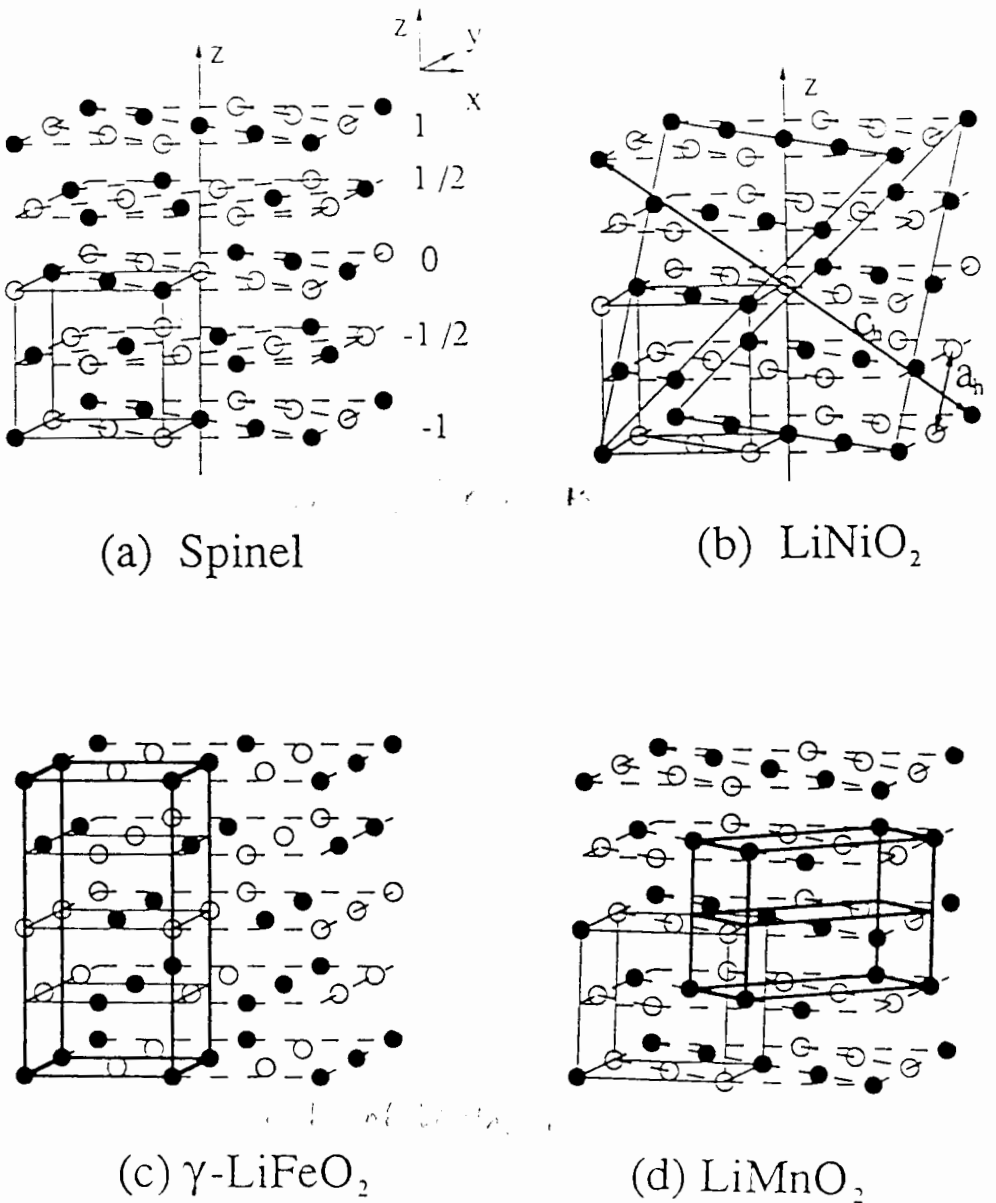

(a) Spinel (b) $LiNiO_2$

(c) γ-$LiFeO_2$ (d) $LiMnO_2$

Figure 2.6. The 2x2x2 cubic supercell showing the cation positions only in (a) spinel structure (e. g. $Li_2Ti_2O_4$) (b) layered structure (e. g., $LiNiO_2$) (c) γ–$LiFeO_2$ structure and (d) orthorhombic $LiMnO_2$. In (a) the conventional unit cell is equal to the size of the 2x2x2 cell, while the conventional cells in (b), (c) and (d) are indicated with thick lines. The conventional fcc lattice is indicated in thin lines.

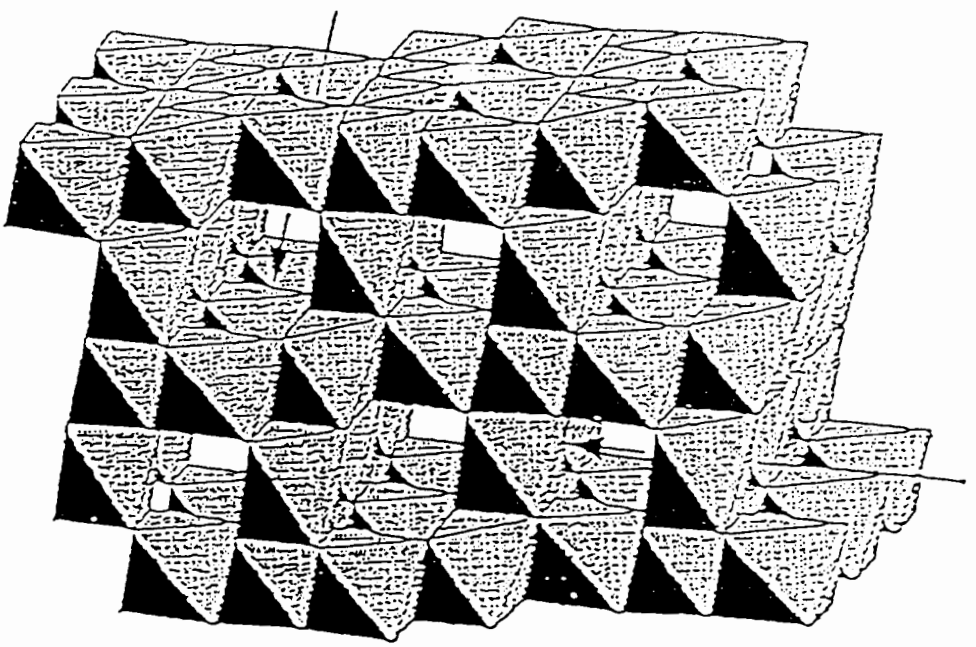

Figure 2.7. The crystal structure of the spinel $LiMn_2O_4$ represented by the oxygen octahedra (Thackeray et al.).

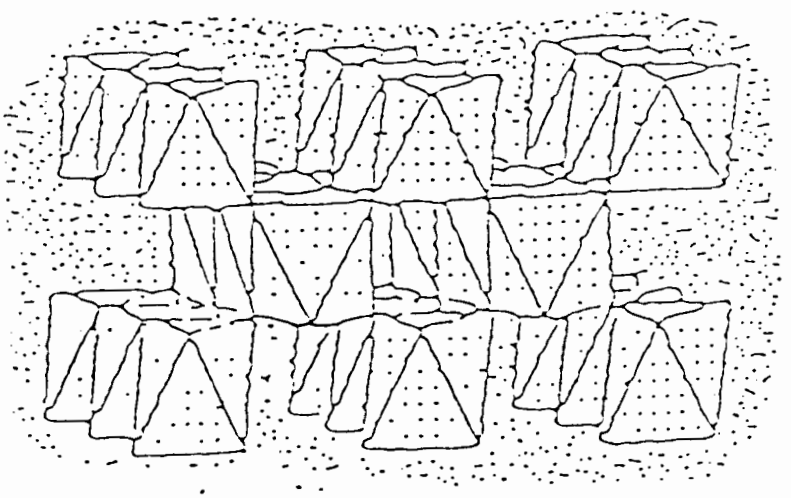

Figure 2.8. Crystal structure of β–MnO_2 represented by hexagonal closed packed oxygen octahedra.

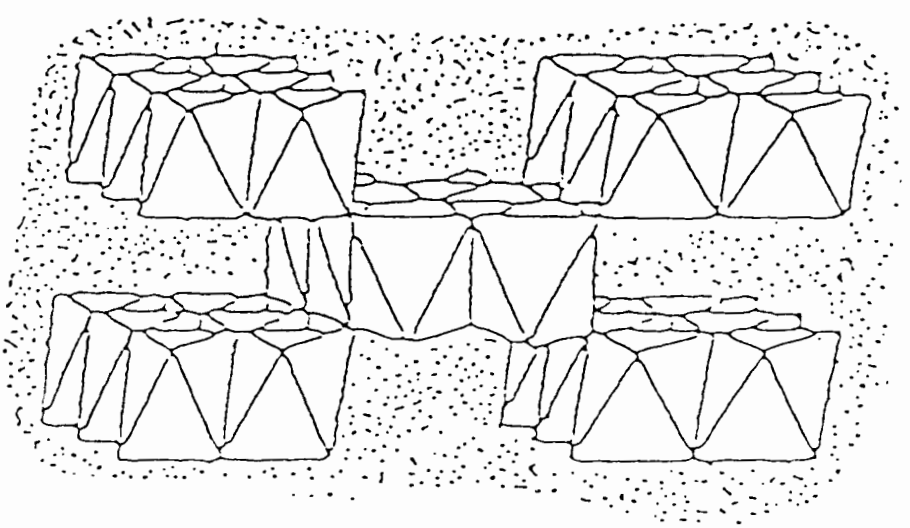

Figure 2.9. Crystal structure of Ramsdellite-MnO_2 represented hexagonal closed packed oxygen octahedra.

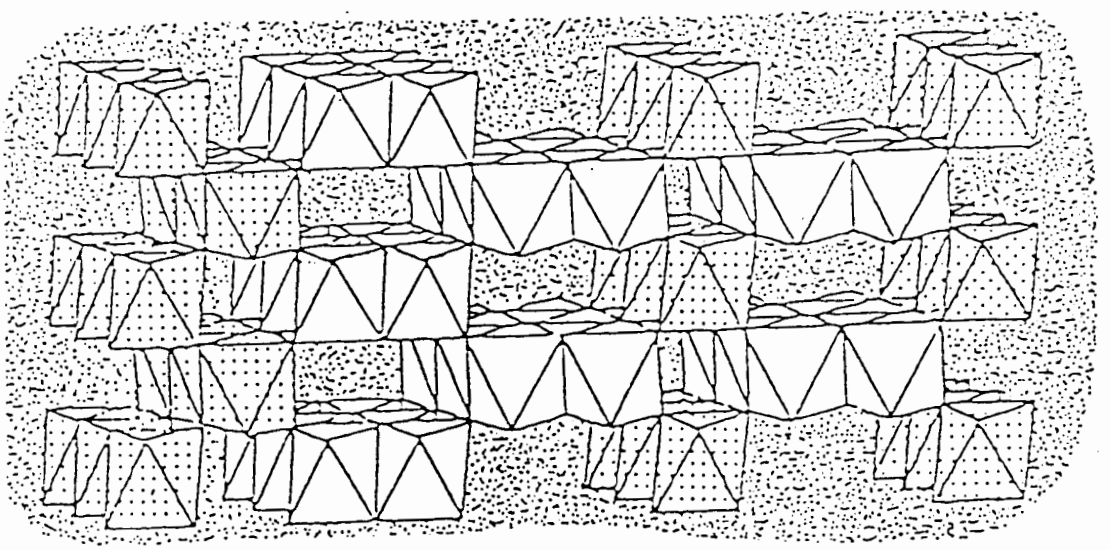

Figure 2.10. Crystal structure of γ-MnO_2 represented by hexagonal closed packed oxygen octahedra (Glover).

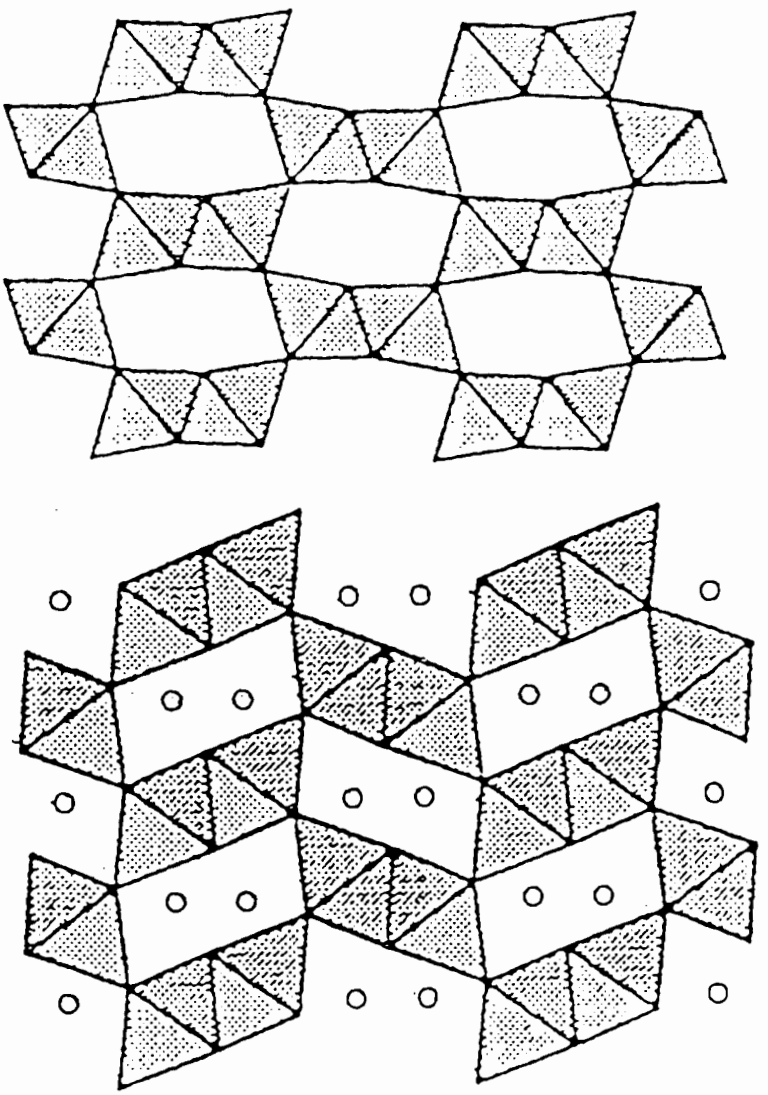

Figure 2.11. The structures of Ramsdellite-MnO_2 (drawn in two dimension from figure 2.9) and of γ–$Li_{0.9}MnO_2$ (Thackeray, Rossouw, Gummow et. al). The circles are for the lithium atoms.

Chapter 3. Lattice Gas Model Approach to Understanding the $LiMO_2$ Structures

3.1.1 Previous Applications to FCC systems

As mentioned in Chapters 1 and 2, the crystal structures of cathode materials affect their electrochemical performance. Many theories have been used successfully to explain crystal structures. One example is the Ising model which is used to simulate magnetic systems and A-B binary alloys. Although it is easy to write down the Hamiltonian for such models, approximate methods are needed to solve for thermodynamic observables in most cases. These approximations include mean-field theory (Clapp and Moss), the cluster-variation method (W. Shockley), and Monte Carlo simulations (Phani, Lebowitz and Kalos). Binary alloys with fcc structures are simple chemical systems which have been understood with a lattice-gas model. Ducastelle recently reviewed the studies of the application of lattice gas models to *A-B* alloys.

Figure 3.1 shows the fcc structure and the 12 nearest neighbors and the 6 second-nearest neighbors to a site at the origin. J_1 and J_2 are defined as the interaction energies between the nearest neighbor atoms and second-nearest neighbor atoms respectively. In lattice-gas models of the type considered here, the sites are occupied by A atoms or by B atoms, and therefore a particular structure can be described by the site occupations. The site occupation in the lattice-gas model (A or B) corresponds to the spin state (up or down) in the Ising model. Furthermore, the chemical potential μ , which is analogous to the magnetic field in the Ising model, is used in the lattice-gas model to

control the stoichiometry of the lattice. Lattice-gas models use the same physical ideas as the Ising model (Binder).

Clapp and Moss studied an Ising model of alloy ordering and observed maxima in the short-range-order diffuse scattering in disordered alloys corresponding the positions of the minima in $J(\mathbf{k})$, which is the Fourier transform of the pairwise interatomic potential $J(\mathbf{r})$. They located the minima of $J(\mathbf{k})$ as a function of the ratio J_2/J_1. In such a way, they determined a phase diagram for the fcc (faced centered cubic) lattice and for the bcc (body centered cubic) lattice.

The phase diagram of an Ising fcc antiferromagnet in a field was studied by Monte Carlo simulation to determine the ground state of a lattice (Binder). When only nearest-neighbor interactions are included, many ordered phases or their mixtures are stable in the ground states. Three ordered phases (A_3B, AB, AB_3) occur corresponding to Cu_3Au, CuAu, $CuAu_3$ in the Cu-Au system. A Monte Carlo model with nearest neighbor and next nearest neighbor interactions was used to study a substitutional binary fcc solid solution (Gahn). Many stoichiometric structure types related to binary alloys were reported. Multiatom interactions in the fcc Ising binary alloy were studied by Monte Carlo simulations to determine the low temperature behavior (Styer, Phani and Lebowitz).

The cluster variation method (CVM) was used to calculate the phase-diagram of the fcc lattice-gas with first and second nearest neighbor interactions (Sanchez and de Fontaine). Furthermore, the tetrahedron and octahedron cluster variation method was used to calculate the phase diagrams of binary fcc lattice-gases with first (positive) and second nearest neighbor interactions (Mohri, Sanchez and De Fontaine).

Lattice gas and spin models were solved by mean field theory to determine the highest temperature ordered phases on stacked triangular lattices (Reimers and Dahn, 1992). The ordered structures which form on AAA, $ABAB$ and $ABCABC$ stacked layers were obtained as a function of J_1, J_2 and J_3 (J_3 is the third nearest neighbor interaction constant) . For $ABAB$ and $ABCABC$ stacking, the inter-plane interaction, J_3 causes the frustration of ordered structures within the planes and the possibility of incommensurate order just below the critical temperature.

A lattice-gas model was used successfully to explain the order-disorder transition in $Li_xNi_{2-x}O_2$ (Li, 1992). In this model the solid solution, $Li_xNi_{2-x}O_2$ can be rewritten as A_xB_{1-x} where the oxygen atoms are ignored to simulate a binary alloy. The neglect of the oxygen atoms is justified because their locations do not depend on x. The structure of $Li_xNi_{2-x}O_2$ was also measured by x-ray diffraction experiments. The Rietveld structure refinement procedure was used to obtain a least-squares fit between the calculated and observed profile intensities. In x-ray Rietveld analysis, the best fit is obtained by adjusting cell constants, atomic coordinates, site occupancies, peak shapes, background, etc. The location of Li and Ni atoms could thus be accurately determined and compared to the theoretical predictions. The lattice-gas model was solved both by the mean-field theory and by the Monte Carlo method to compare to experiment and we (Li, Reimers and Dahn, 1992) found that the order-disorder transition in $Li_xNi_{2-x}O_2$ could be well modeled. This model reproduced the data very well for appropriate choices of J_1 and J_2. Furthermore, the short-range cation ordering in $Li_xNi_{2-x}O_2$ was further studied using synchrotron x-ray diffraction (Reimers, Li, Dahn, 1993). Both short range and long range ordered structures appear near the phase transition point.

3.1.2 Application to LiMO_2

The rock-salt related LiMO_2 structures described in Chapter 2 have similar fcc oxygen frames and differ only in the cation arrangement. Therefore a lattice-gas model can be used to study these structures when only the cation arrangement is considered.

We start with a lattice-gas model Hamiltonian:

$$H = \frac{1}{2}\sum_{\mathbf{r},\mathbf{r}'} t_{\mathbf{r}} t_{\mathbf{r}'} J(\mathbf{r}-\mathbf{r}') + \mu \sum_{\mathbf{r}} t_{\mathbf{r}} \qquad (3.1)$$

where $\mathbf{r}$ is a position vector in the cation lattice, $t_{\mathbf{r}}$ has two states, $t_{\mathbf{r}}=1$, and $t_{\mathbf{r}}=0$ to designate that the site is filled by a transition metal or a lithium respectively, $J(\mathbf{r}-\mathbf{r}')$ is the interaction potential between sites $\mathbf{r}$ and $\mathbf{r}'$ and μ is the chemical potential of the transition metal atoms in the lattice. We use the convention that positive J corresponds to a repulsive interaction. Li-Li interactions are accounted for through the absence of M-M interactions (Li, Reimers and Dahn, 1992). [Since $t_{\mathbf{r}}=\pm 1$ in the Ising model and $t_{\mathbf{r}}=1,0$ in the lattice-gas model, the lattice-gas-interaction constants (J's) will differ by a factor of 4 from those of an Ising model with a Hamiltonian of the form (3.1) when comparing the two models in the same units].

The fcc lattice gas has been extensively studied with application to A-B alloys (Ducastelle). The ground-state phase diagram of the fcc lattice gas with nearest-neighbor (NN) and next-nearest-neighbor (NNN) interactions has been calculated (Clapp and Moss). Studies of the fcc lattice gas with repulsive (positive) J_1 and J_2 , such that $J_2<J_1/2$, predict ground states with cations

arranged as in γ-$LiFeO_2$ (Sanchez and de Fontaine). For repulsive J_1 and J_2 such that $J_2 > J_1/2$, the ground state has cations segregated into alternate planes normal to the cubic <111> directions as in CuPt. This is the cation arrangement observed in $LiNiO_2$. Furthermore, by analogy with their statements about CuPt, Richards and Cahn imply without proof that the spinel atom arrangement found in LT-$LiCoO_2$ and in $Li_2Ti_2O_4$ is energetically equivalent to the layered arrangement like $LiNiO_2$. Clapp and Moss did not mention the spinel phase in their work, but did identify phases with atoms arranged as in $LiNiO_2$ and γ-$LiFeO_2$. The ground states of the fcc lattice gas with first- and second-neighbor interactions listed in Ducastelle include the degenerate layered and spinel structures. Ducastelle states that the degeneracy is lifted if tetrahedron interactions are introduced. Gahn used Monte Carlo computer simulations to study the ground states of binary fcc structures with first- and second-nearest-neighbor interactions. For $J_2/J_1 > 0.5$ and $J_1 > 0$, he reported that after cooling from the high-temperature disordered phase, only the layered structure appears. On the other hand, Phani and Lebowitz reported, based on privately communicated unpublished results, that the spinel phase weakly dominates at low temperatures for the same set of interactions used by Gahn. Finel used the low-temperature series-expansion method to predict that the layered structure is the most stable for $J_1 > 0$, and the spinel is most stable for $J_1 < 0$. Clearly, there is some confusion in the literature about the relative stability of these phases at finite temperature. This problem is settled here in this chapter.

3.2 Ground States

The lattice-gas model Hamiltonian (3.1) can be solved using the mean field approximation. Following the steps from the reference (Reimers and Dahn, 1992), the free energy is obtained in the mean field approximation:

$$F(T,\mu)=\frac{1}{2}\sum_{\mathbf{r},\mathbf{r}'}x_{\mathbf{r}}x_{\mathbf{r}'}J(\mathbf{r}-\mathbf{r}')+\mu\sum_{\mathbf{r}}x_{\mathbf{r}}$$
$$+k_BT\sum_{\mathbf{r}}[x_{\mathbf{r}}\ln x_{\mathbf{r}}+(1-x_{\mathbf{r}})\ln(1-x_{\mathbf{r}})] \qquad (3.2)$$

where $x_{\mathbf{r}}$ is the thermally averaged occupancy of site $\mathbf{r}$. We express $x_{\mathbf{r}}$ in terms of a non-uniform component $\eta_{\mathbf{r}}$, which is related to the ordered super-lattice structures which may form, and a uniform component x=1/2 with a selected μ.

$$x_{\mathbf{r}}=1/2+\eta_{\mathbf{r}} \qquad (3.3)$$

and

$$\sum_{\mathbf{r}}\eta_{\mathbf{r}}=0 \qquad (3.4)$$

The goal is now to find the set $\eta_{\mathbf{r}}$, which minimizes F(T,μ,) for a particular μ and T. In order to diagonalize the second order term in η, in the free energy expression, we use the Fourier transform:

$$\eta_{\mathbf{r}}=\sum_{\mathbf{q}}\eta_{\mathbf{q}}\exp(i\mathbf{q}\cdot\mathbf{r}) \qquad (3.5)$$

where the prime on the summation symbol indicates that q=0 is not included in the summation. We require that $\eta_{-q}=\eta_q^*$ to ensure that η_r is real. Combining equations (3.2-3.5) we have:

$$F/N = f(T) = \frac{1}{2}\sum_{\mathbf{q}}{}'(4k_BT + J_{\mathbf{q}})\eta_{\mathbf{q}}\eta_{-\mathbf{q}} + \frac{4k_BT}{3}\sum_{\mathbf{q}_1\mathbf{q}_2\mathbf{q}_3}\eta_{\mathbf{q}_1}\eta_{\mathbf{q}_2}\eta_{\mathbf{q}_3}\eta_{\mathbf{q}_4}\delta(\mathbf{q}_1+\mathbf{q}_2+\mathbf{q}_3+\mathbf{q}_4+\mathbf{K}) + O(\eta^6) \tag{3.6}$$

where

$$J_{\mathbf{q}} = \sum_{\mathbf{r}} J(r)\exp(i\mathbf{q}\cdot\mathbf{r}) \tag{3.7}$$

and **K** is an fcc reciprocal lattice vector. Terms not involving the Fourier amplitudes, $\eta_{\mathbf{q}}$, have been dropped from the free energy.

An ordered phase appears upon cooling with $\eta_{\mathbf{q}}\neq 0$ once $4k_BT+J_{\mathbf{q}}<0$. Therefore, to find the ordering wavevector, **q**, first selected as the system is cooled, we need only find the vectors **q** which minimize $J_{\mathbf{q}}$. Figure 3.1 shows the cation lattice with the first and second neighbor interactions included. To simplify the calculation we use a rhombohedral Bravais lattice in which there is only one atom per cell. The cation lattice shown in figure 3.2 is the rhombohedral Bravais lattice with primitive vectors, $\mathbf{a}_1$, $\mathbf{a}_2$, and $\mathbf{a}_3$. We write an arbitrary wave vector, **q**, as

$$\mathbf{q}=q_1\mathbf{a}_1^*+q_2\mathbf{a}_2^*+q_3\mathbf{a}_3^* \tag{3.8}$$

where the $\mathbf{a}_i^*$ are the primitive reciprocal lattice vectors of the real-space rhombohedral lattice. Using equation 3.7, the fact that $\mathbf{a}_i^* \cdot \mathbf{a}_j = 2\pi\delta_{i,j}$ and the arrangement of the lattice, we obtain

$$\begin{aligned} J_{\mathbf{q}} = 2J_1[&\cos 2\pi q_1 + \cos 2\pi q_2 + \cos 2\pi q_3 + \cos(2\pi(q_1 - q_2)) \\ &+ \cos(2\pi(q_2 - q_3)) + \cos(2\pi(q_3 - q_1))] + 2J_2[\cos(2\pi(q_1 + q_2 - q_3)) \\ &+ \cos(2\pi(q_1 - q_2 + q_3)) + \cos(2\pi(-q_1 + q_2 + q_2))] \end{aligned} \tag{3.9}$$

The components (q_i) of the vector $\mathbf{q}$ which minimize $J_{\mathbf{q}}$ are with reference to the rhombohedral reciprocal axes. For convenience, we then convert $\mathbf{q}$ to the reciprocal lattice of the conventional cubic cell also shown in figure 3.2.

Figure 3.3 shows the ground state phase diagram for the fcc lattice gas as a function of J_1 and J_2. In each designated portion of the diagram we list one of the set of symmetry related wavevectors, $\mathbf{q}$, which minimize $J_{\mathbf{q}}$. For example, at the top of the diagram, the wavevector <1/2,1/2,1/2> designates the four symmetry related vectors (1/2,1/2,1/2), (1/2,-1/2,1/2), (-1/2,1/2,1/2) and (-1/2,-1/2,1/2). To determine the ordered arrangements which form, we must consider whether the system selects a state where only one of the $\eta_{\mathbf{q}}$ is nonzero (a single $\mathbf{q}$ from the symmetry related set) or a state where more than on of the $\eta_{\mathbf{q}}$ is nonzero (a multiple $\mathbf{q}$ state). The layered $LiNiO_2$ structure corresponds to the <1/2, 1/2, 1/2> phase with a single wavevector and the spinel $Li_2Ti_2O_4$ phase corresponds to the selection of the four <1/2, 1/2, 1/2> wavevectors with equal weight and appropriate phase.

For example, using equations (3.3), (3.5), $\eta_{q1}=1/2$, $\eta_{q2}=\eta_{q3}=\eta_{q4}=0$, a wavevector (1/2,1/2,1/2) as q_1, and $\mathbf{r}$ selected at fcc sites as shown in figures 2.6 with one fcc cell as a unit volume, we obtain the layered structure indicated by $x_{\mathbf{r}}=1$ for Li sites (or Ni sites) and $x_{\mathbf{r}}=0$ for Ni sites (or Li sites). The same

layered structure is obtained using one of the other three wavevectors (1/2,1/2,-1/2), (1/2,-1/2,1/2) and (-1/2,1/2,1/2) as q_1 with only a difference in rotation of the structure about the z axis. Using equations (3.3), (3.5) and $\eta_{q1}=\eta_{q2}=\eta_{q3}=(-\eta_{q4})=1/4$ we obtain the spinel structure indicated by $x_{\mathbf{r}}=1$ for Li sites (or Ti sites) and $x_{\mathbf{r}}=0$ for Ti sites (or Li sites) with the four <1/2,1/2,1/2> wavevectors

There are four degeneracy lines identified in figure 3.3 (Bold). Along the line $J_2=0$ and $J_1>0$, the wave vector takes the form (0, 1, q) (in directions of $\mathbf{a}_x$, $\mathbf{a}_y$, $\mathbf{a}_z$) where q is arbitrary, hence an infinite number of wavevectors are selected forming a line in the Brillouin zone. For $J_2>0$ and $J_1=2J_2$ the wavevector is $(q_1, q_2, q_3)_R$ (in directions of $\mathbf{a}_1, \mathbf{a}_2, \mathbf{a}_3$) where $\tan(q_3/2)=(2\sin q_1+2\sin q_2+\sin(q_1+q_2))/(\cos(q_1+q_2)+1)$, hence a surface is selected in the Brillouin zone. For $J_2<0$ and $J_1=0$, the wavevectors are (0,0,0) and (1,0,0) and for $J_1<0$ and $J_2=-J_1$, the wavevector is (q,q,±q) with q arbitrary.

In each of the single phase regions of the phase diagram, for example in the <1/2,1/2,1/2> region, we must consider whether a single or multiple **q** state gives the lowest free energy. In general, this is done by considering the fourth, and higher, order terms in the Landau expansion. Recalling that the Fourier amplitudes are complex we write them as

$$\eta_{\mathbf{q}_j} = \eta_j e^{i\phi_j} \qquad (3.10)$$

where j labels the ordering wavevector and η_j is real. The higher order terms will be functions of all η_j's and ϕ_j's. For systems with many degenerate ordering wavevectors the resulting many parameter minimization of the free energy becomes unmanageable. As an alternative we note that the mean field entropy at $x=1/2$ is maximized when the magnitude of all $\eta_{\mathbf{r}}$ are equal, *i.e.*

$$\eta_{\mathbf{r}}^2 = \eta_{\mathbf{r}'}^2 \qquad (3.11)$$

where r and r' are any two fcc lattice sites. This also ensures that at low temperature all sites are either pure transition metal or pure lithium. Any two structures (with $\min\{J_{\mathbf{q}}\}$ the same) that satisfy (3.11) will have the same free energy to all orders in the Landau expansion.

Substituting (3.5) into (3.11) and summing over the allowed wavevectors in each region of the phase diagram (fig. 3.3) we determine the number of wavevectors allowed and their corresponding phase angles. For the lower right corner ($J_1>0$, $J_2>0$) there are three wavevectors of the type (100). The conditions (3.11) are only satisfied when only one of the wavevectors is present (*i. e.* $\eta_1\neq 0$, $\eta_2=\eta_3=0$) with phase angle $\phi=0$ or π. This results in a total of 6 structures which are trivially related by interchanging the four fcc sublattice labels. In the region $J_1>0$ and $0<J_2<1/2J_1$, we find one wavevector solutions to (3.11) with the phase angle $\phi_2=\pi/4$. Two wavevector solutions such as $\mathbf{q}_1=(1/2,0,1)$, $\mathbf{q}_2=(1/2,1,0)$, $\eta_1=\eta_2$, $\phi_1=0$ and $\phi_2=\pi/2$ also satisfy (3.11) but yield identical real space structures as those obtained with only one wavevector. In the region at the top of the phase diagram ($J_2>0$ and $-J_2<J_1<2J_2$) there are four (1/2,1/2,1/2) ordering wavevectors. Equation (3.11) can be satisfied when only one wavevectors is present with phase angle $\phi=0$, resulting in a layered structure. However, another solution to (3.11) exists with $\eta_1=\eta_2=\eta_3=\eta_4$ and $\phi_1=\phi_2=\phi_3=0$ and $\phi_4=\pi$, or any cyclic permutation thereof. These solutions correspond to the spinel structure. Hence, within the mean field approximation the layered and spinel structures both have identical free energies. All results of this section only apply when $x=1/2$ in (3.2).

By inspection of the spinel and layer structures in figure 2.6(a) and 2.6 (b), the number of M-M contacts in each of the layered and spinel structures is equal to 6, which contributes $6J_1$ to the internal energy. Similarly, the number of second-neighbor (0) and third-neighbor (12) contacts is also identical. In fact, it can be proved that the number of M-M contacts at any distance in the two structures is the same ! This is easily shown. Consider the atom at the origin (the center of the supercell) of figure 2.6 (a). The spinel structure can be changed to the layered structure by rotating the (001) planes at $z=(n+1/2)a$ by $\pi/2$ about the z axis. **No distance from any atom to the atom at the origin is changed by this rotation.** Since this choice of origin and axes is arbitrary, any point in each of two lattices has the same number and type of M-M, M-Li, and Li-Li contacts out to infinite distance. Thus the ground-state energies of the layered and spinel structures are the same, provided only pairwise interactions are included.

The layered and spinel structures are very important for lithium transition metal oxides, and there is some confusion in the literature about the relative stability of these phases at finite temperature. Monte Carlo methods are used in the following section to investigate the structures for $x=1$ in $Li_xM_{2-x}O_2$ with first- and second-neighbor interactions. The results show that the layered and spinel structures are degenerate not just at $T=0$; but also degenerate at $T>0$. The free energy and entropy of the two structures upon warming are the same (within statistical error) in the entire range of temperature $0 \leq T \leq T_C$ for various values of J_1 and J_2. The layered and spinel structures also appear with equal probabilities in cooling runs.

3.3 Phase Diagram at Finite Temperature

Here Monte Carlo methods (Binder, 1986) are used to calculate the J_1-J_2-T phase diagram.

In thermodynamic fluctuation theory, the distribution function of any macroscopic variable will be sharply peaked around its average value; e. g., for the energy E itself, the distribution will be peaked at $<E>_T$, which is proportional to N, while the width of the distribution will be proportional to $\sqrt{N}$. The Ising model is one of the typical samples studied with the Monte Carlo method. On a scale of energy per spin in Ising model, the width of the distribution shrinks to zero as $1/\sqrt{N}$ for N tending to infinity. Thus, at any temperature, a rather narrow region of the configuration space of the system contributes significantly to the averages; If states were generated randomly, very small fraction of the generated states would actually lie in this important region of configuration space.

In the Metropolis method (Binder, 1986), the sample is chosen with a probability proportional to the Boltzmann factor itself, i.e. , the states are distributed according to a Gaussian distribution around the appropriate average value. In the Ising-model example, one starts with some initial spin configuration. Thermal fluctuations are simulated by repeating the following six steps again and again:

1) Choose one spin to be considered for flipping (S_i to $-S_i$)

2) Calculate the energy change ΔH relative to that flip

3) If $\Delta H<0$, flip the spin, otherwise calculate the transition probability defined by $W=\exp(-\Delta H/k_B T)$ for that flip

4) Generate a random number p between zero and unity

5) If $p<W$ flip the spin, otherwise do not flip

6) Calculate the averages as desired with the resulting configuration

The Metropolis method is used here to calculate the J_1-J_2-T phase diagram The J_1-J_2-T phase diagram for the fcc lattice-gas model is shown in figure 3.4. The center of the diagram corresponds to the high-temperature disordered phase with the rocksalt (NaCl) structure. No new ordered phases that do not exist at T=0 appear at finite temperature for x=1/2 in $Li_xM_{1-x}O$. For many values of J_1 >0, the critical temperatures have been reported previously (Phani and Liebowtiz; Mohri, Sanchez, and de Fontaine).

The critical temperatures have also been calculated here for J_1<0 using the Monte Carlo method on an 8x8x8 fcc lattice (N=8^3x4). Critical temperatures were determined from the maximum in the fluctuations of the order parameter (i.e., the maximum in the ordering staggered susceptibility) which is defined as

$$\chi_q = <\eta_q^2 - <\eta_q^2>>^{1/2} \qquad (3.12)$$

The composition x=1/2 was maintained by fixing the transition-metal chemical potential,

$$\mu = -6J_1 - 3J_2 \qquad (3.13)$$

To compare the critical temperatures here with those of much of the previous work, one must remember that lattice-gas-interaction constants (J's) will differ by a factor of 4, from those of an Ising model with a Hamiltonian of the form (3.1).

As the layered and spinel structures are rather common for $LiMO_2$ materials, we feel it is important to study the relative stability of the

structures at finite temperature. Just because the ground states are equal in energy by no means implies that the free energies or entropies are the same at finite temperature. If one structure has a higher density of low-lying excited states it will have a higher entropy at finite temperature, hence being stabilized *and* preferentially selected upon slow cooling. As mentioned above, some conflicting work on this question exists in the literature and, to our knowledge, no published Monte Carlo work exists for the case $J_1<0$ (Li, Reimers and Dahn, 1994). Here we use both conventional Monte Carlo and recently introduced histogram Monte Carlo methods (Ferrenberg and Swendsen) by which the density of states and the entropy can be calculated directly.

As stated previously, the spinel structure can be converted to the layered structure by simply rotating every other layer [i.e., those labeled by half integers in Figure 2.6 (a)] by 90°, about the z direction. One can also extend this idea to excited states. Any low-lying excited state above the spinel ground state can be converted, by 90° rotation, to a corresponding low-lying excited state above a layered ground state. When $J_1=0$, the neighboring layers are uncoupled and there is no change in energy upon such rotation of any excited state. As a result, for every low-lying excited state above the spinel ground state there is a corresponding excited state above one of the layered ground states, with exactly the same energy. This one to one correspondence means that the density of low-lying excited states is identical, and also that no thermal selection will occur upon slow cooling, when $J_1=0$. When $J_1\neq0$, the neighboring layers become coupled and our simple proof no longer applies. Nevertheless, this rigorous result for $J_1=0$ provides an important test of the Monte Carlo methods described below, which is used to address the question of thermal selection when $J_1\neq0$. Indeed, it is true that for $J_1=0$, the Monte

Carlo method predicts an identical (within statistical error) low-temperature entropy and density of low-lying excited states. This gives us confidence in our Monte Carlo results for the case $J_1 \neq 0$.

The transition-metal atom densities for the spinel and layered structures are described by the same set of four wave vectors, with Fourier amplitudes η_1, η_2, η_3, and η_4, respectively. Layered structures are described by any one of the four modes, and the spinel structure has equal contributions from all four modes. The root-mean squared Fourier amplitude,

$$\eta = (\eta_1^2 + \eta_2^2 + \eta_3^2 + \eta_4^2)^{1/2} \qquad (3.14)$$

makes no distinction between the two phases. However, the order parameter,

$$\Delta = 2(|\eta_1| + |\eta_2| + |\eta_3| + |\eta_4|) - 3(\eta_1^2 + \eta_2^2 + \eta_3^2 + \eta_4^2)^{1/2} \qquad (3.15)$$

is 1 for perfect spinel order and -1 for perfect layered order.

For interactions in the spinel and/or layered region of the phase diagram, slow annealing with the Monte Carlo method resulted in both the spinel and layered phases with 50 % probabilities. The result was independent of the sign of J_1. This implies that the free energies of the spinel and layered phases are equal near T_c. Figure 3.5 shows the probability distribution of Δ, $[P(\Delta)]$, at temperatures near and below T_c. The area under the peaks in the distribution is (50±2) % at any temperature. This shows that within statistical errors, the system is fluctuating between the two phases below T_c with equal probability. The number of Monte Carlo steps needed for a fluctuation between phases increases rapidly below T_c , making low-temperature studies of this problem with conventional Monte Carlo methods difficult.

The energy-probability distribution $P_\beta(E)$ at inverse temperature $\beta=1/kT$ can be calculated approximately by Monte Carlo methods using

$$P_\beta(E) = \frac{H_\beta(E)}{\sum_E H_\beta(E)} \qquad (3.16)$$

where the energy E is distributed over a finite number of discrete bins, and $H_\beta(E)$ is the number of Monte Carlo configurations generated with energy E during the simulation, i.e., $H_\beta(E)$ is an energy histogram obtained from a simulation at inverse temperature β. If $P_\beta(E)$ is known then the density of states can also be calculated from (Ferrenberg and Swendsen)

$$P_\beta(E) = \frac{W(E)e^{-\beta E}}{\sum_E W(E)e^{-\beta E}} = \frac{W(E)e^{-\beta E}}{Z_\beta} \qquad (3.17)$$

where $W(E)$ is the density of states and Z_β is the partition function. In practice, $H_\beta(E)$ will contain statistical noise due to the finite duration of the simulation. Assuming Poisson statistics, the statistical error in $H_b(E)$ is simply $H_\beta(E)^{1/2}$. Since $P_\beta(E)$ is strongly peaked near $\langle E\rangle_\beta$, the counting statistics in the wings of the distribution will be very poor. This problem can be overcome by combining histograms from simulations at many different temperatures selected in such a way that all energy bins receive sufficient sampling. The histograms are then combined in an optimal manner, described in the reference (Ferrenberg and Swendsen), resulting in an estimate for the density of states $W(E)$ or the entropy S_β.

Here we use an 8x8x8 fcc lattice (Li, Reimers and Dahn, 1994). The spinel and the layered structures are introduced in the lattice at very low temperature (0.1 T_c). The system is then gradually warmed up to a very high temperature (10000 T_c). The temperatures are properly chosen to ensure that all energy bins receive sufficient sampling. The relative uncertainty of $W(E)$ is proportional to $1/\sqrt{H_i(E)}$. For each temperature, $5\text{x}10^4$ Monte Carlo steps are summed, giving $2\text{x}10^6$ configurations over a total of 40 temperature points.

The spinel and layered ground states are each eightfold degenerate. Hence the total degeneracy of the ground state is 16, and the entropy equals ln16 at T=0. When T is infinite, the entropy of the system is Nln2 (N is the total number of the sites). Therefore, the entropy of the layered phase and the spinel phase equal each other at T=0, and T=∞, without dependence of J_1 and J_2. The difference in the entropy of spinel and layered structures at low temperatures is calculated by warming up from their ground states, and by equalizing the entropy at T=0 for the two structures. This can be thought of as a low-temperature expansion calculated by Monte Carlo methods.

The Monte Carlo method is used to calculate $W(E)$ and the entropy of the spinel and layered structures for J_1=0, J_1<0, and J_1>0, respectively. Figure 3.6(a) shows the results of the ratio of $W(E)$ for the two structures after warming for J_1=-(1/2)J_2<0. The results are similar for cases of J_1=0 and J_1>0. The statistical error estimation is shown at the same time with two dashed lines. E_0 is the ground-state energy. For $(E\text{-}E_0)/NJ_2$ near zero, the error estimation is quite large since some energy bins were sampled very infrequently. For $(E\text{-}E_0)/NJ_2$ near 0.8, which corresponds to very high-temperature excitations, the error estimation is also large because these bins are at energies greater than $\langle E\rangle_{T=\infty}$ and are, therefore, infrequently sampled. The arrow indicates the average energy at the critical temperature $\langle E\rangle_{Tc}$.

Clearly, the difference between $W(E)_{spinel}$ and $W(E)_{layer}$ for $E<<E>_{Tc}$ is within the estimated error. That means there is no difference in the density of excited states for the layered and spinel structures within statistical error. Figure 3.6(b) shows the entropy per site S/N vs temperature for the layered and spinel structures. For the entire range of the temperature, the difference of S/N for two structures is on the order of $5.0 \times 10^{-5}\ k_B$, which is too small to see in figure 3.6(b). That means the spinel and layered structures have identical free energy and entropy in the region of where $-J_2<J_1<2J_2$ and $J_2>0$.

The structures of lithium transition-metal oxides $LiMO_2$ are related to those of binary alloys, and can be explained with the lattice-gas model. The spinel and layered structures, which are common in $LiMO_2$ compounds, have energetically identical ground states, for arbitrary pairwise interactions out to any distance. Furthermore, we (Li, Reimers and Dahn, 1994) proved that the spinel and layered structures have identical free energies and entropies for $J_1=0$. Using Monte Carlo methods, we extend the conclusion to the region of $-J_2<J_1<2J_2$ and $J_2>0$ where the spinel and layered structures also have identical free energy and entropy (with statistical error) in the entire range of temperature. In the next section, we show that the theoretical results can explain the experimental results very well.

3.4 The Layered and Spinel Phases of $LiCoO_2$

Layered $LiCoO_2$ is prepared by reacting stoichiometric mixtures of Li_2CO_3 and $CoCO_3$ in air at 850°C (Mizushima, Jones, Wiseman and Goodenough) and it is called HT-$LiCoO_2$. Another phase called LT-$LiCoO_2$ was prepared by spray drying a solution of $LiNO_3$ and $Co(NO_3)_2{\cdot}6H_2O$ followed by heating to 400°C in air (Reimers, Li, Rossen and Dahn). LT-$LiCoO_2$ can also be prepared by heating a stoichiometric mixture of $LiOH{\cdot}H_2O$ and $CoCO_3$ in alumina boats, to 400°C in extra dry air for 90 hours. Neutron diffraction studies determined that LT-$LiCoO_2$ was structurally similar to the normal high temperature form of HT-$LiCoO_2$ (Gummow, Thackeray, David and Hull). The structural difference between LT-$LiCoO_2$ and HT-$LiCoO_2$ is that the hexagonal cell constants, $c/a \approx 4.9$ for LT-$LiCoO_2$, were consistent with an ideal cubic close packed oxygen lattice, and $c/a \approx 5.0$ for HT-$LiCoO_2$, was slightly distorted from the ideal cubic close packed oxygen lattice. Figure 3.7 (Reimers, Li, Rossen and Dahn) shows the observed x-ray powder diffraction profile, calculated profile, and difference profile for LT-$LiCoO_2$ and for HT-$LiCoO_2$. Comparing the x-ray powder diffraction profiles of LT-$LiCoO_2$ and HT-$LiCoO_2$, one finds that the peak intensity ratios and peak positions for both materials are almost identical. For example, the peaks 003, 101, 104, 015, 113 in LT-$LiCoO_2$ have the same peak intensity ratios and almost the same positions as those in HT-$LiCoO_2$, respectively. The peaks 006 and 102, split when $c/a \neq 4.9$, are merged when $c/a = 4.9$. The sum of the 006 and 102 intensities in HT-$LiCoO_2$ is equal to that of the the 006/102 merged peak in LT-$LiCoO_2$. The 018 and 110 peaks behave similarly.

The electrochemical behavior of the two $LiCoO_2$ materials is markedly different. Figure 3.8 (Reimers, Li, Rossen and Dahn) shows the voltage versus

composition Δx in $Li_{1-x}CoO_2$ for both LT-$LiCoO_2$ and HT-$LiCoO_2$. It is hard to understand how two materials with very similar powder diffraction patterns can exhibit such large differences in electrochemical behavior.

The puzzle is solved if one abandons the assumption that LT-$LiCoO_2$ adopts a layered structure. The spinel structure has identical free energy and entropy according to the results from sections 3.2 and 3.3 so it might be formed instead of the layered structure. The hexagonal distortion is, of course, absent in the spinel structure. However, do we expect the diffraction intensities for the layered and spinel structures to be so similar? We consider this point below.

In the spinel structure, the oxygen atoms form a cubic-close-packed array which is identical to the oxygen network in the layered structure of HT-$LiCoO_2$ when we neglect the small hexagonal distortion. The contributions from the oxygen atoms to the x-ray diffraction are therefore identical. Since the layered and spinel structures have the same number and type of Co-Co, Co-Li, and Li-Li contacts out to infinite distance, the intensities of the Bragg peaks can be easily proved to be identical for both structures using the Debye formula (Reimers, Li, Rossen and Dahn), as we show below.

The Debye formula is valid for both small clusters of atoms and extended crystal structures. The scattered intensity, I(q), at wave vector $q=4\pi\sin\theta/\lambda$ is given by (Warren)

$$I(q) = \sum_{i,j} f_i(q) f_j(q) \frac{\sin(qr_{i,j})}{qr_{i,j}} \qquad (3.18)$$

where f_i and f_j are the atomic scattering factors for the atoms at sites i and j, and $r_{i,j}$ is the distance between sites i and j. Another way of writing (3.18) is

as a sum over coordination shells (*i.e.* nearest neighbor, next nearest neighbor, etc.)

$$I(q)=\sum_m [N_m(Co-Co)f_{Co}^2+N_m(Co-Li)f_{Co}f_{Li}+N_m(Li-Li)f_{Li}^2+...]\frac{\sin(qr_m)}{qr_m} \quad (3.19)$$

where $N_m(Co\text{-}Co)$ is the number of *Co-Co* contacts in the mth coordination shell and r_m is the distance to the mth coordination shell. The two lattices have the same number and type of *Co-Co* , *Li-Co* and *Li-Li* contacts out to infinite distance as we showed earlier. The further terms in 3.19, indicated by "+...", corresponding to *O-O* and *O*-cation contacts, are also clearly the same for both the spinel and layered structures. Therefore $I(q)$ is identical for the spinel and the layered structures. This conclusion is independent of the scattering probe. For example, powder patterns for the spinel and the layered structures are identical if measured with either x-ray or neutron scattering.

Figure 3.9 shows the simulated x-ray powder patterns (Reimers, Li, Rossen and Dahn) for both the spinel structure and the "cubic layered structure". The cubic layered structure is identical to the layered HT-$LiCoO_2$ structure except that the O-Li and O-Co layer spacings are fixed to be identical and the cell constant ratio is fixed at its ideal cubic value $c/a=\sqrt{24}\approx 4.9$. The simulated powder patterns shown in figure 3.9 are absolutely identical. The conclusion is also valid for neutron powder patterns.

In this chapter, a lattice gas model was used to explain the structures of some lithium transition metal oxides. The spinel and layered structures were proved to be energetically identical which explains why spinel and layered $LiCoO_2$ exist. HT-$LiCoO_2$ is the thermodynamically stable phase because it is stabilized by the hexagonal distortion which is not included in the theory in

this chapter. Furthermore, the theoretical results were used successfully to explain the similarity between the x-ray diffraction patterns of HT-$LiCoO_2$ and LT-$LiCoO_2$. We also showed that the crystal structure is very important for determining the electrochemical behavior of the materials. In the following chapter, in-situ x-ray diffraction methods are used to study electrochemically the structures of $Li_{1-x}NiO_2$.

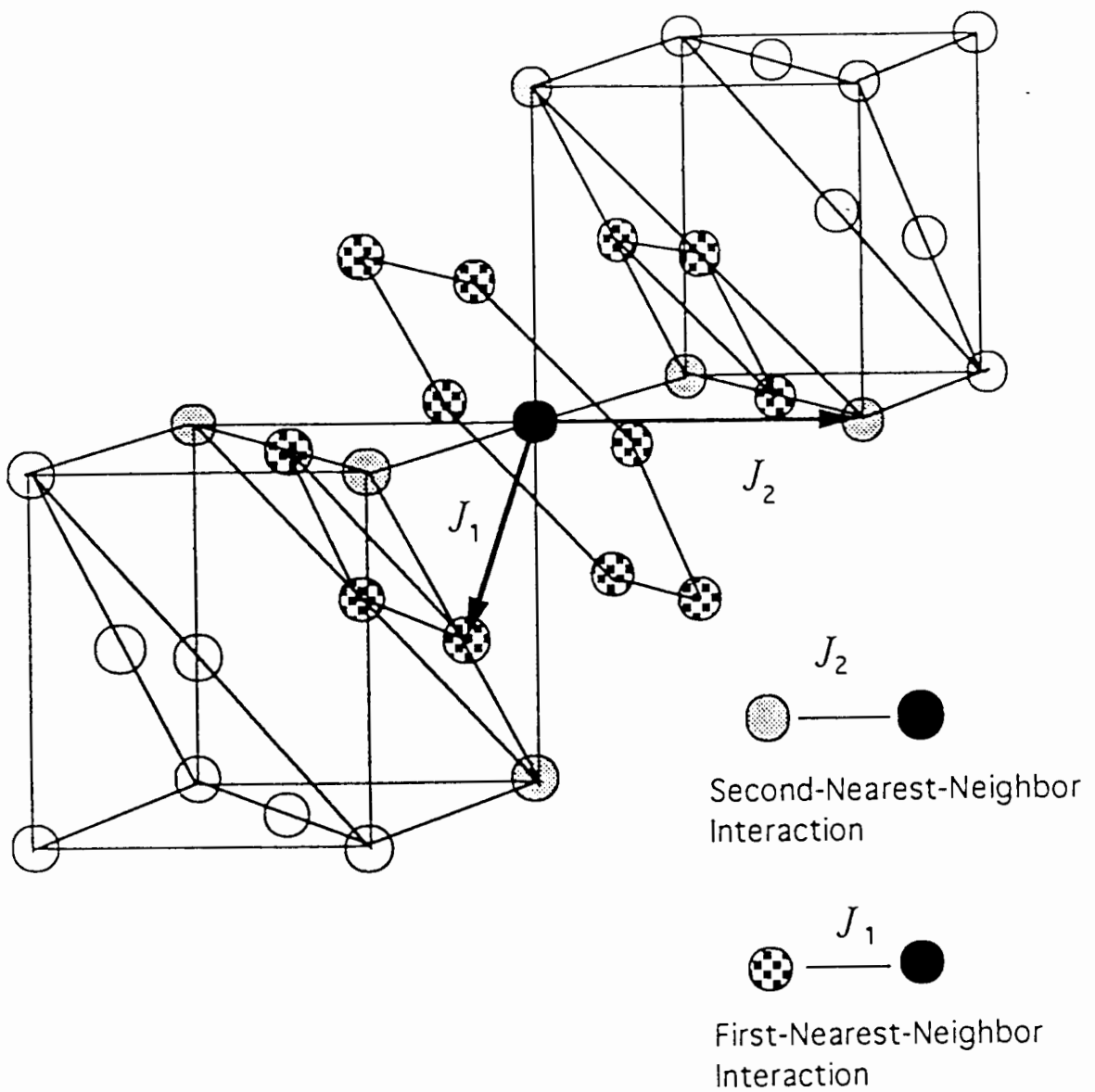

Figure 3.1. The first-nearest-neighbor- and the second-nearest-neighbor interactions are shown for the black site in the cation lattice. The gray balls are the second-nearest-neighbor sites and the checkerboard balls are the first-nearest-neighbor sites.

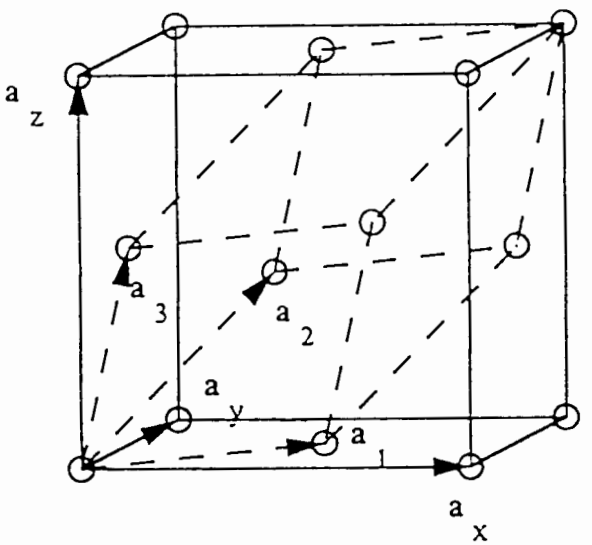

Figure 3.2. The vectors $\mathbf{a}_1$, $\mathbf{a}_2$, $\mathbf{a}_3$ are shown for the rhombohedral primitive lattice (dashed lines). The vectors $\mathbf{a}_x$, $\mathbf{a}_y$, $\mathbf{a}_z$ for the conventional fcc cubic lattice are shown at the same time.

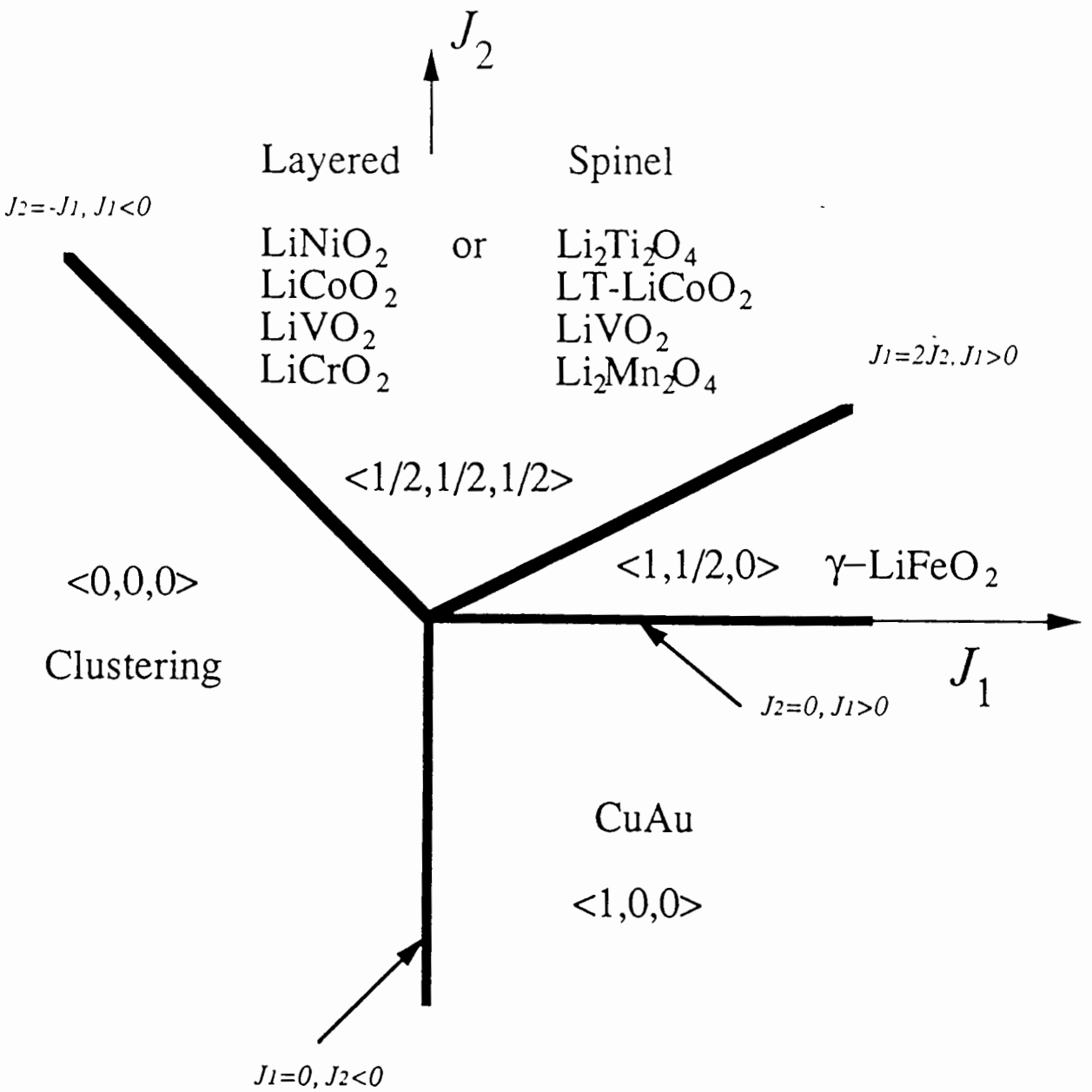

Figure 3.3. The phase diagram of the fcc lattice predicted by mean-field theory as a function of J_1 and J_2. The positions of the layered, spinel, and γ–$LiFeO_2$ structures have been indicated as have the family of ordering wave vectors in each single-phase region.

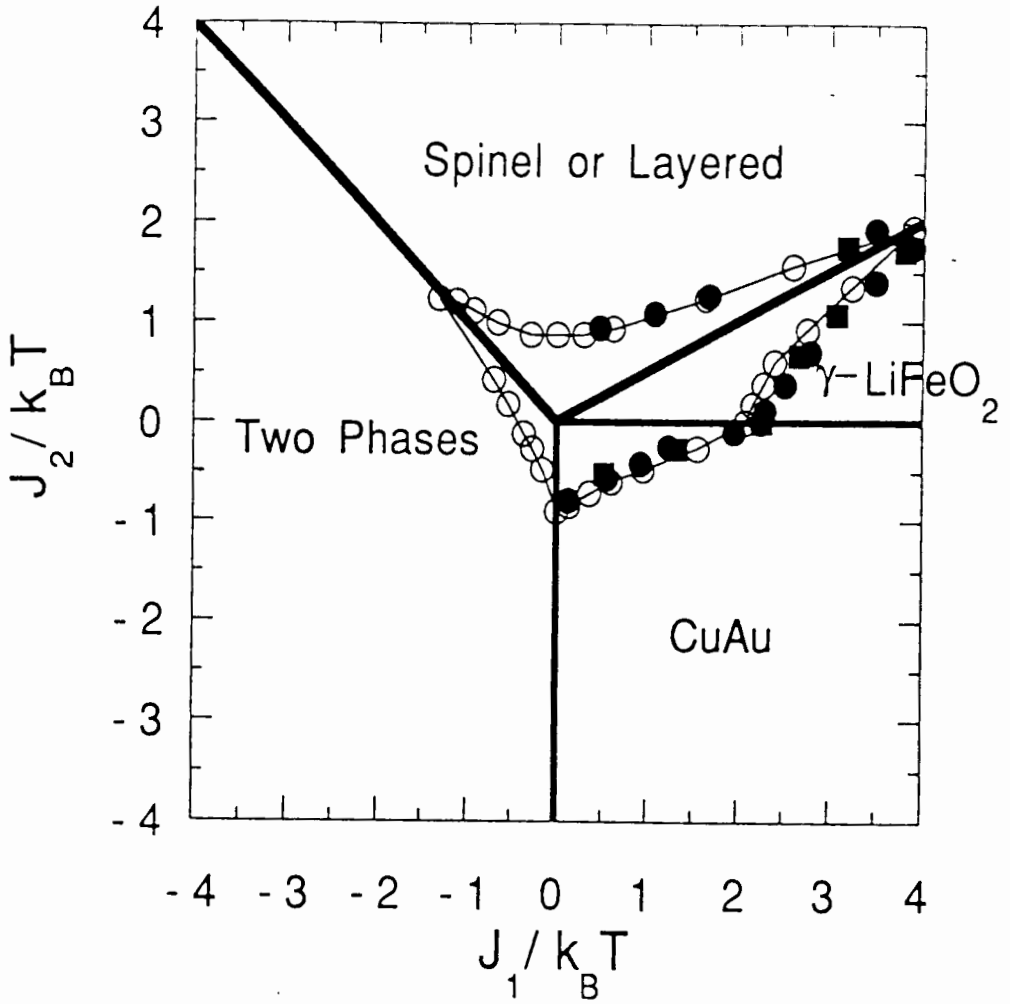

Figure 3.4. The phase diagram calculated by Monte Carlo methods. The region inside the data points around the origin (0, 0) is the high-temperature disordered phase. Outside the data points, where careful calculations were made, the ordered structures indicated are formed. The black circle data points are from Phani et. al, and the black square data points are from Mohri et. al.

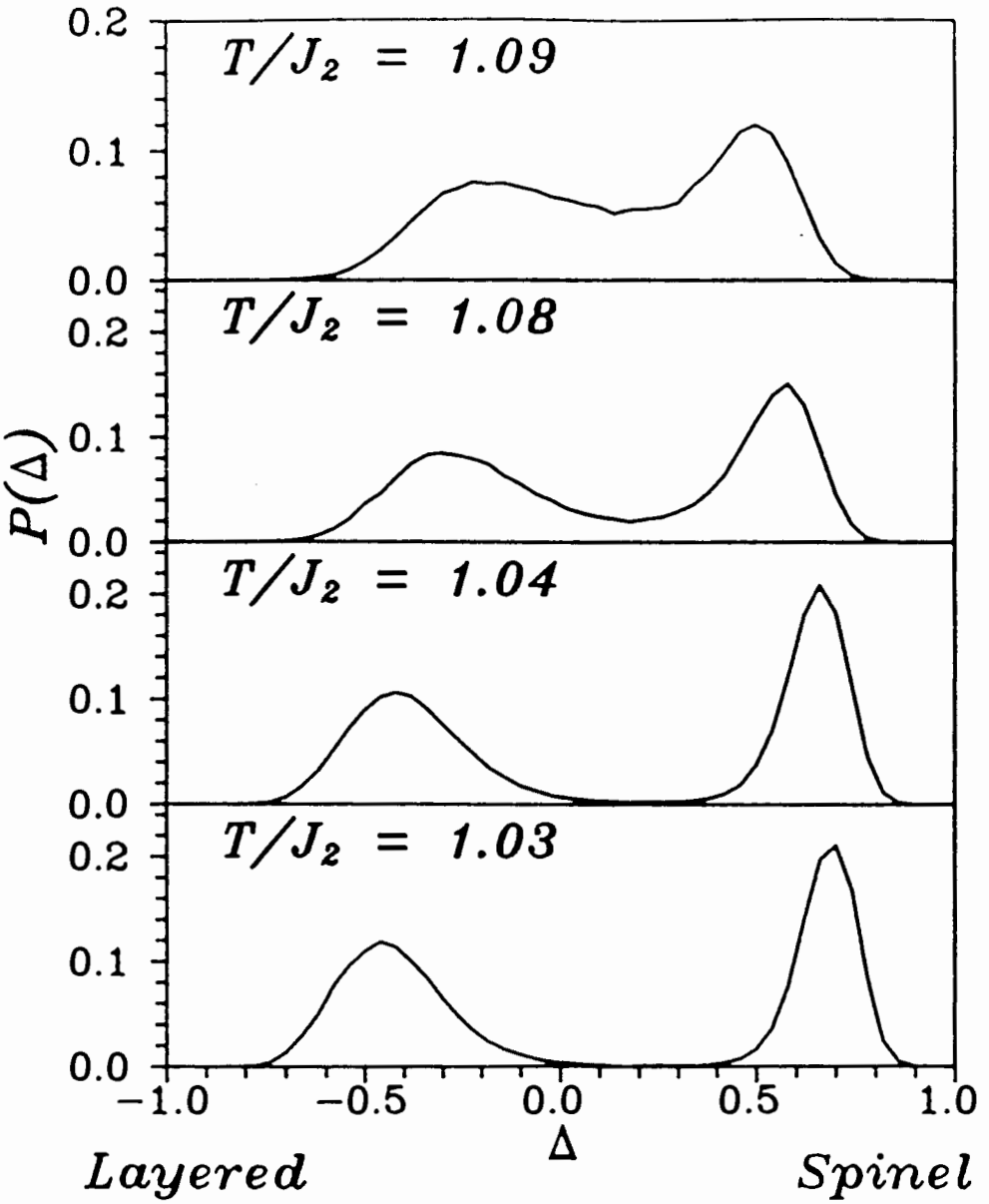

Figure 3.5. The probability $P(\Delta)$ of finding a particular value of Δ. The layered and spinel phases appear with equal probability for various temperatures below T_c. The calculation is for an 8x8x8 lattice using J_1=0. 1.0x10^6 Monte Carlo steps per site were used to generate the probability distribution. Similar results are obtained for various values of J_1, provided one stays in the region of stability of the spinel and layered phases.

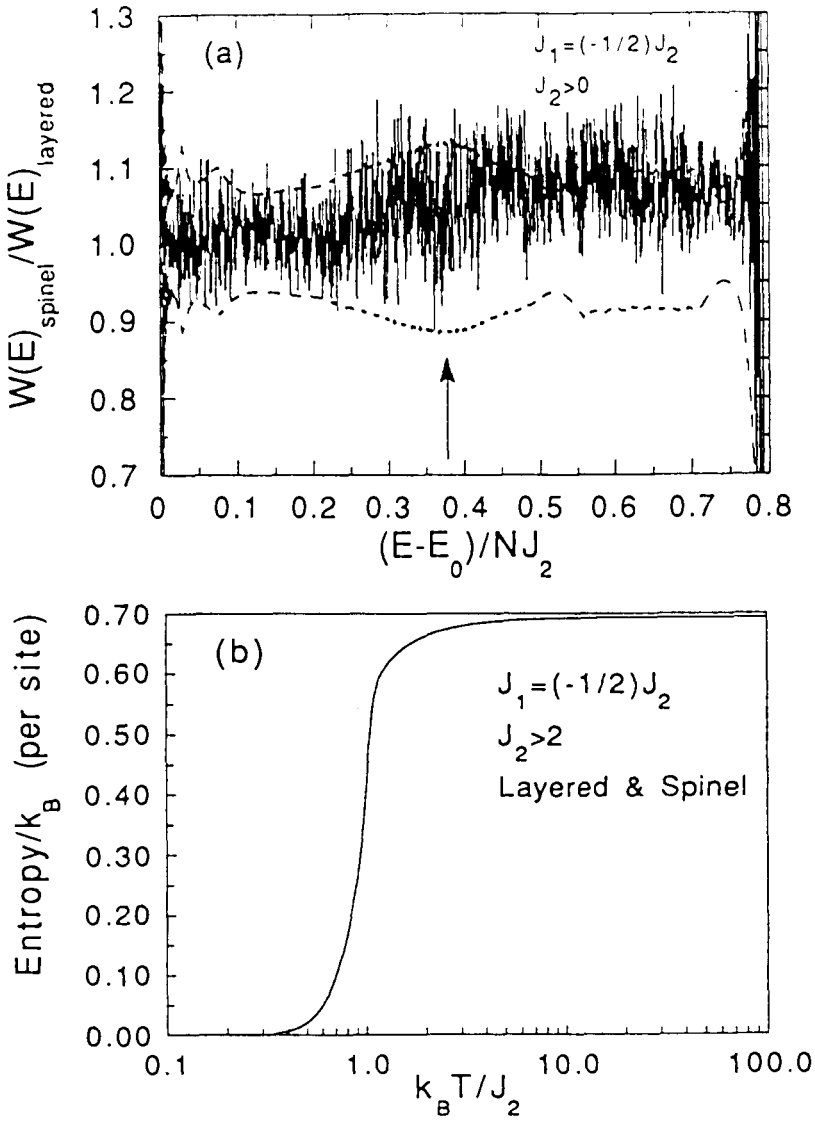

Figure 3.6. (a) Ratio of density of states $W(E)$ for spinel and layered structures are shown as calculated using Monte Carlo methods. The dashed lines show the positive and negative ($\pm\sigma$) error estimations. E_0 is the ground-state energy. The arrow indicates the value of $\langle E-E_0\rangle_{T=T_c}/NJ_2=0.376$. (b) Entropy per site S is shown vs k_BT/J_2 for layered and spinel structures. The difference in S/N for the two structures is less than $5\times10^{-5}k_B$.

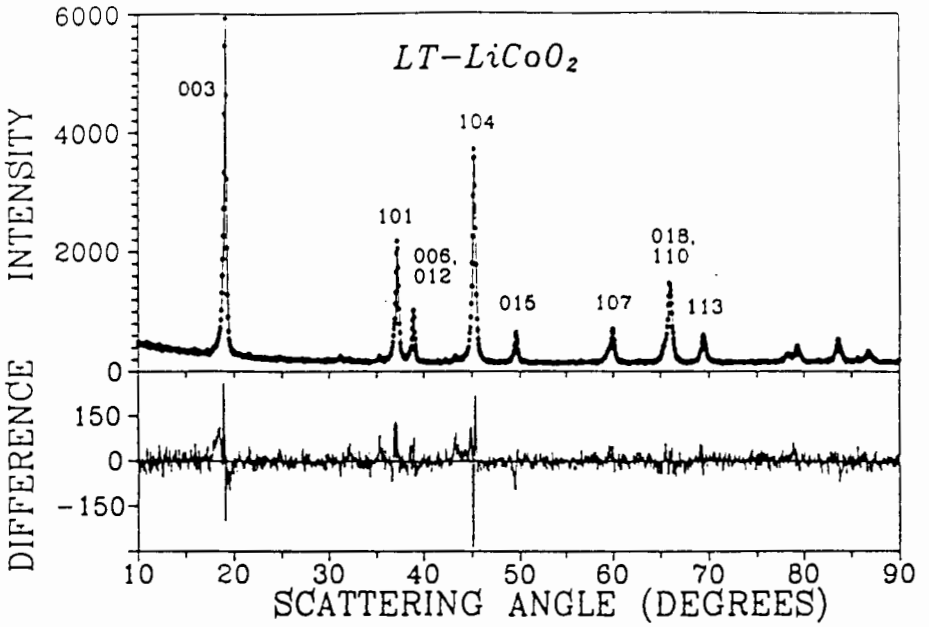

Figure 3.7a Observed x-ray powder diffraction profile, Calculated profile, and difference profile for LT-$LiCoO_2$ indexed with the hexagonal layered structure.

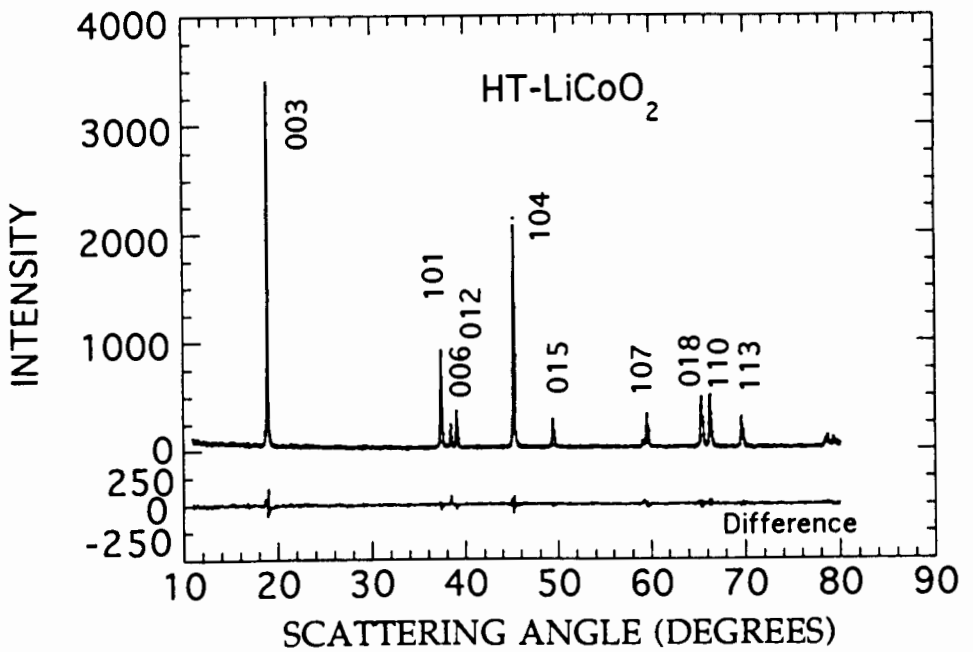

Figure 3.7b. Observed x-ray powder diffraction profiles, Calculated profile, and difference profile for HT-$LiCoO_2$ indexed with the hexagonal layered structure.

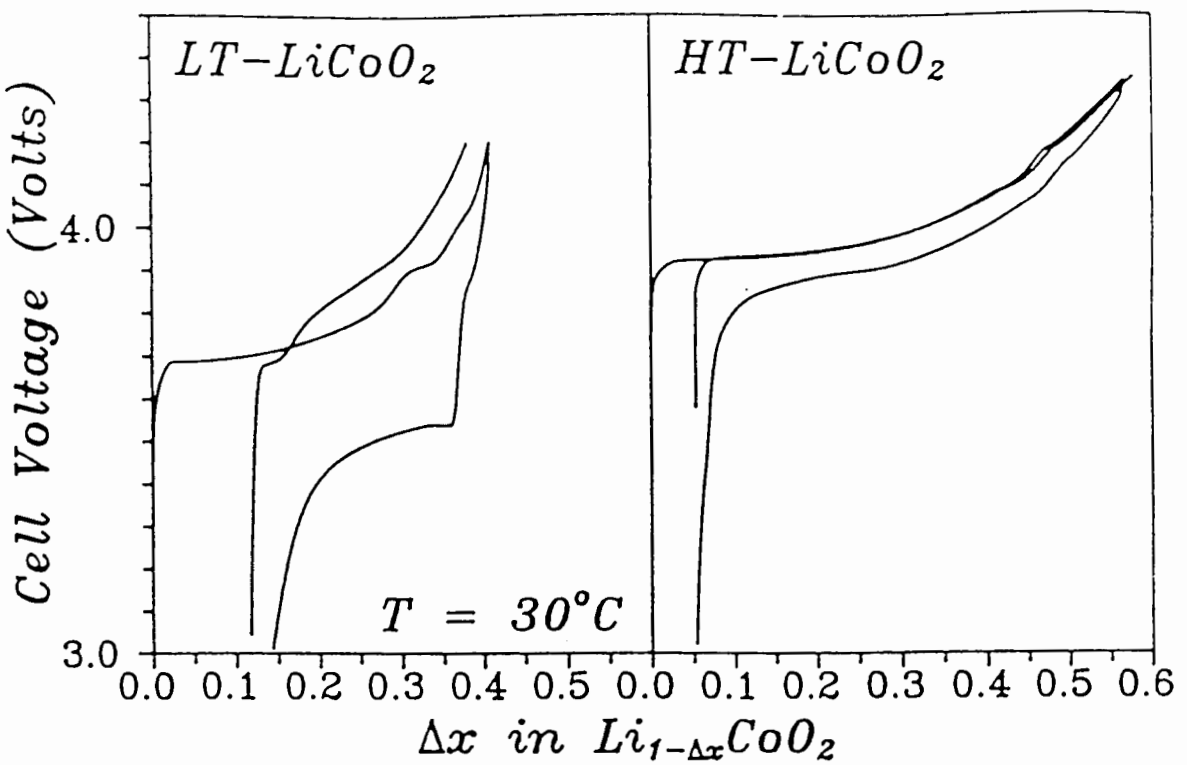

Figure 3.8. Voltage versus composition Δx in $Li_{1-\Delta x}CoO_2$ for $Li/LiCoO_2$ cells with LT (left) and HT (right) forms of $LiCoO_2$ as cathodes.

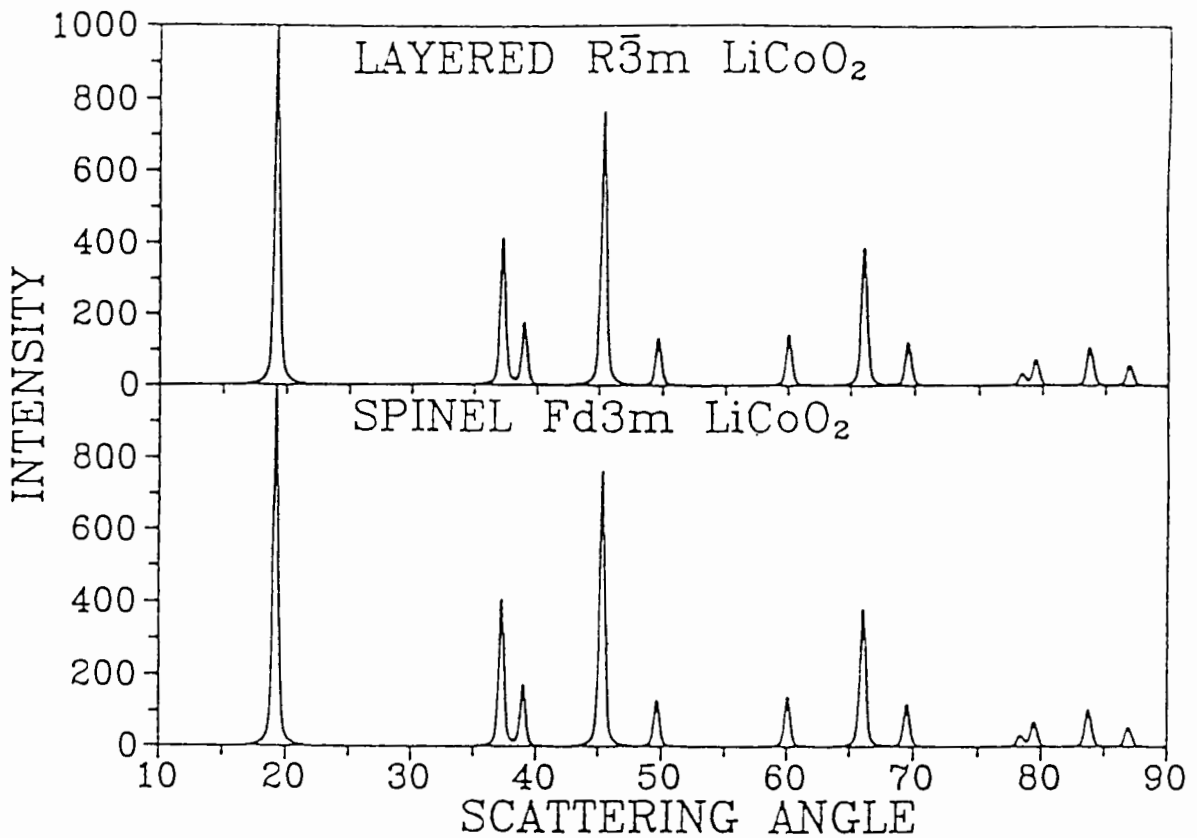

Figure 3.9. Simulated x-ray powder diffraction profiles of modified cubic layered HT-$LiCoO_2$ and spinel (Fd3m) LT-$LiCoO_2$ (or $Li_2Co_2O_4$).

Chapter 4. In Situ X-ray diffraction and Electrochemical Studies of $Li_{1-x}NiO_2$

4.1 Introduction

As described in Chapters 1 and 2, $LiNiO_2$ is one of the current candidates for an electrode material for use in advanced rechargeable batteries. The crystal structure changes which occur as a function of x in $Li_{1-x}NiO_2$ have been studied with much less precision in two previous reports (Dahn, von Sacken and Michal; Ohzuku, Ueda and Nagayama). In the former one, the structure was found to be single phase for $0 \leq x \leq 0.6$ in $Li_{1-x}NiO_2$ because insufficient resolution and counting statistics were used in the X-ray measurements. In the more precise measurements of the latter one, studies on separate samples showed evidence for a monoclinic phase and two-phase regions between this phase and neighboring hexagonal phases. However, two-phase regions were not indicated on the phase diagram presented in the reference (Ohzuku, Ueda and Nagayama).

We used in situ x-ray diffraction to study the structures of $Li_{1-x}NiO_2$ (Li, Reimers and Dahn, 1993). The original x-ray cell design (Dahn, Py and Haering) works well to study low voltage cathode materials like Li_xTiS_2 where the voltage of the electrode is below 3.0 V with respect to Li metal. For cathodes like $Li_{1-x}CoO_2$ and $Li_{1-x}NiO_2$, which operate near 4.0 V, corrosion of the beryllium and stainless steel cell hardware is severe (Reimers and Dahn, J. Electrochem. Soc., 1992) and makes cell life short. Here, a new improved in situ x-ray cell design is used to minimize corrosion of the cell hardware.

4.2 Experimental

$LiNiO_2$ was prepared by reacting stoichiometric mixtures of $LiOH{\cdot}H_2O$ (FMC, Bessemer City, NC, USA) and $Ni(OH)_2$ (Aldrich Chemical Company Inc. Milwaukee, WI, USA). The powders were ground with a mortar and pestle and were then heated at 700°C for two hours in air (Li, Reimers and Dahn, 1992). Cathodes were prepared by mixing $LiNiO_2$ powders with 5 % by weight of Super S carbon black (Chemetals Inc., Baltimore MD, USA) and a (2 % by weight) binder solution of EPDM (ethylene propylene diene terpolymer) in cyclohexane, to make a slurry of the electrode powder mixture. The slurry was spread on aluminium foil and allowed to dry. Typical cathodes had a coverage of 20 mg/cm^2 and were 1.2x1.2 cm^2 in size. A 1 M solution of $LiPF_6$ in equal volumes of propylene carbonate and ethylene carbonate was used as electrolyte in these in situ x-ray cells. 2325-size coin cells using these electrodes as described by Dahn et al. were also used to test the $LiNiO_2$.

Figure 4.1 shows the new design used here for the in situ x-ray cell. The cathode is attached to the cell base where the elevated area (Al base in figure 4.1) of the base is exactly the same size as that of the cathode. The electrochemical corrosion reaction is apparently very sensitive to the pressure and distance between the anode and cathode. This design minimizes the possible corrosion reaction area between the cell base and the beryllium window since the area within the O-ring not covered by the cathode is widely separated (2 mm) from the beryllium window. The cells are not flooded with electrolyte. Hence, the electrochemically active space is only the area of the cathode and the lithium foil. The beryllium window is not corroded at Li potential but is strongly corroded at 4 V. Thus, the Li is placed in contact with the Be.

X-ray diffraction measurements were made using a Phillips powder diffractometer with a diffracted beam monochromator. Cu Kα radiation was used and the x-ray beam penetrated through the beryllium window, lithium foil and the separator to reach the cathode. Beryllium and lithium are light elements, the separator is a 50 micron film of Celgard #2502 microporous polypropylene, so we can still observe a strong diffraction signal from the cathode (Dahn, Py and Haering). The small loss in x-ray intensity, associated with placing the anode next to the beryllium, is greatly offset by the much improved electrochemical reliability of the cell.

X-ray diffraction data points were recorded every 0.05° of 2θ and one x-ray diffraction scan took about 80 min, which corresponded to about Δx=0.01 at the small current which was used. About 80 x-ray diffraction patterns were obtained during both charge and discharge to allow careful observations of the $Li_{1-x}NiO_2$ structure changes.

The structure of the $LiNiO_2$ starting material was characterized by Rietveld profile refinement as described previously (Li, Reimers and Dahn, 1992). Figure 4.2 shows the structure of $LiNiO_2$. The hexagonal unit cell is drawn with thick lines and a monoclinic unit cell needed to index $Li_{1-x}NiO_2$ for $0.25 \leq x \leq 0.50$ is shown with dashed lines. Another monoclinic unit cell used by Ohzuku et al with the same a_M and b_M, but with a different choice for the other axis specified by c' and β', is also shown. $LiNiO_2$ is not perfectly ordered as shown in figure 4.2, there are about 2 % of the lithium atoms in the nickel layers and 2 % of the nickel in the lithium layers (Li, Reimers and Dahn, 1992).

4.3 Results

Figure 4.3a shows V(x) for several cycles of a Li/$Li_{1-x}NiO_2$ coin cell cycled at a 100 hour rate (at the current chosen, it would take 100 hours to change x by Δx=1). The $V(x)$ profile shows several pronounced plateau regions which are more clearly observed when dx/dV is plotted versus V as shown in figure 4.3b (dx/dV on discharge and -dx/dV on charge). For figure 4.3, x is calculated from the cathode active mass and the charge transfer. During the x-ray experiment, the cell voltage and x corresponding to the middle of each scan were recorded. It is our goal to understand the origin of the structure in $V(x)$ and the peaks in dx/dV. The labelling of the peaks and single phase regions in figure 4.3b will be made clear in our subsequent discussions. Sharp peaks in -dx/dV correspond to phase transitions and minima correspond to single phase regions (Berlinsky, Unruh, McKinnon and Haering).

Some (every 3rd scan) of the in situ data for the $(003)_H$ peak (H for hexagonal structure) is shown in figure 4.4 for the charge from 3.4 V to 4.25 V, which corresponds to $0.0 \leq x \leq 0.82$. Between 3.4 and 4.04 V, the $(003)_H$ peak shifts to lower angle as Li is deintercalated. Above 4.04 V, the peak begins to shift back to higher angle, and then near 4.18 V, its intensity begins to diminish as a new peak near 19.7° appears, in a two-phase region. This two-phase region corresponds to the highest voltage peak in dx/dV shown in figure 4.3b.

Figure 4.5 shows the data in the region of the $(101)_H$ and $(006)_H$ peaks. As the cell is charged above 3.65 V the original $(101)_H$ peak begins to shrink and initially coexists with two new peaks, $(20\bar{1})_M$ and $(1\bar{1}1)_M$, (subscript M denotes the monoclinic phase) which take its place. These two peaks remain, and shift smoothly until near 4.04 V when they coalesce into a single peak again. The

two peaks referred to above have a 1:2 intensity ratio. The weak $(006)_H$ peak shifts smoothly to lower angle, consistent with the behavior of the $(003)_H$ peak, as the cell is charged from 3.4 V until it becomes "buried" under the two peaks derived from $(101)_H$.

Figure 4.6 shows the data in the region of the $(105)_H$ peak. The difference between $(101)_H$ and $(105)_H$ is that there is no significant peak splitting for $(105)_H$ during the whole range of charge. However, the $(105)_H$ peak becomes broad between 3.65 V and 4.04 V, and it becomes sharp again above 4.04 V. It disappears from the angular range plotted above 4.18 V, since it shifts to higher angle, consistent with the behavior of the $(003)_H$ peak.

Figure 4.7 shows the data in the region of the $(107)_H$ peak at the same voltages and lithium concentrations as in figure 4.5. Consistent with the behavior of the $(101)_H$ peak, the $(107)_H$ peak splits into two peaks above 3.65 V, which have a 1:2 intensity ratio again. Above 4.04 V these peaks merge again into a single peak. As the cell is charged through the final (highest) peak in dx/dV (figure 4.3b), the peak weakens and disappears as a new 107 peak at higher angle (not shown) appears and strengthens. This latter behavior is consistent with the behavior of the $(003)_H$ and $(105)_H$ peaks in the same voltage range.

Finally, figure 4.8 shows the behavior of the $(110)_H$ and $(113)_H$ peaks (a portion of the data near the $(110)_H$ peak at the lower voltages was not measured and is unavailable). Below 3.65 V a single $(113)_H$ peak is observed. The peak splits into two broad peaks in the voltage range between 3.65 V and 4.04 V. Again, these peaks merge into a single peak above 4.05 V. Above 4.18 V, this peak disappears as a new $(113)_H$ peak appears at above 70.0°. The $(110)_H$ peak also splits into two peaks (1:2 ratio) between 3.65 V and 4.04 V.

From the information shown in figures 4.4-4.8 it is now possible to completely determine the unit cell of $Li_{1-x}NiO_2$ as a function of x. The 101, 107, 113 and 110 peaks all split in the region between 3.65 and 4.04 V. Most important is the splitting of the 110 peak which means that the distortion of the unit cell is primarily in the plane perpendicular to the hexagonal c axis. Figure 4.2 shows the monoclinic cell consistent with this distortion. In the other voltage ranges the unit cell is hexagonal, and has the same structure type, neglecting lithium, (judging by the peak intensities) as the original $LiNiO_2$ structure. Now we concentrate on the monoclinic phase.

In a hexagonal structure, the $(101)_H$ powder peak is 12-fold degenerate; The degenerate reflections are $\pm(1,0,\pm1)_H$, $\pm(0,1,\pm1)_H$, $\pm(1,\bar{1}, \pm1)_H$. In the space group R 3m, only six of the reflections, $(1,0,\bar{1})$, $(\bar{1}, 0,1)$ $(0,1,1)$, $(0,\bar{1},\bar{1})$, $(1,\bar{1},1)$ and $(\bar{1},1,\bar{1})$ have non-zero intensity. Similarly, $(107)_H$ and $(110)_H$ powder peaks also have six non-zero degenerate reflections. On the other hand, $(113)_H$ has twelve non zero degeneracies. [In R 3m structures, it is customary to label the indices of allowed $10l$ powder peaks as $(10\bar{1})$, (102), $(10\bar{4})$, (105), etc. It has not been done so here explicitly, and instead, when referring to $(101)_H$ and $(102)_H$, that means we are referring to the allowed peaks $[10l]$). In the monoclinic structure, the degeneracy is different from that in R 3m. The transformation between hexagonal unit cell vectors and monoclinic cell vectors describing the undistorted structure shown in figure 4.2 is given by:

$$\begin{bmatrix} \mathbf{a}_M \\ \mathbf{b}_M \\ \mathbf{c}_M \end{bmatrix} = \begin{bmatrix} -1 & 1 & 0 \\ 1 & 1 & 0 \\ 0 & 0 & 1 \end{bmatrix} \begin{bmatrix} \mathbf{a}_H \\ \mathbf{b}_H \\ \mathbf{c}_H \end{bmatrix} \qquad (4.1)$$

where $|a_H| = |b_H|$ for hexagonal unit cell. Hence, the Miller indices transform according to equation (4.2) below:

$$\begin{bmatrix} h_M \\ k_M \\ l_M \end{bmatrix} = \begin{bmatrix} -1 & 1 & 0 \\ 1 & 1 & 0 \\ 0 & 0 & 1 \end{bmatrix} \begin{bmatrix} h_H \\ k_H \\ l_H \end{bmatrix} \qquad (4.2)$$

Using equation (4.2), the six non-zero $(101)_H$ reflections transform to 4 $(1\bar{1}1)_M$ and 2 $(20\bar{1})_M$ reflections. Moreover, the six $(107)_H$ reflections transform to 4 $(1\bar{1}7)_M$ and 2 $(20\bar{7})_M$, and the 6 $(110)_H$ reflections to 2 $(020)_M$ and 4 $(310)_M$. The 12 $(113)_H$ reflections transform to 8 $(310)_M$ and 4 $(023)_M$. The ratios of the intensities of the neighboring monoclinic peaks derived from a single hexagonal powder peak are simply given by the ratios of the multiplicities:

$$(1\bar{1}1)_M/(20\bar{1})_M=(1\bar{1}7)_M/(20\bar{7})_M=(310)_M/(020)_M=(313)_M/(023)_M=2 \qquad (4.3)$$

For the case of the $(105)_H$ peak, the splitting between $(\bar{1}15)_M$ and $(205)_M$ is not large enough to be seen, but the peak becomes broad in the monoclinic phase. The behavior of the $(102)_H$ peak (not shown here) is also similar to that of the $(105)_H$ peak. The peaks used here for least square fitting the unit cell parameters in the monoclinic phase include (003), $(20\bar{1})$, $(1\bar{1}1)$, (006), (202), $(\bar{1}12)$, (205), $(\bar{1}15)$, $(20\bar{7})$, $(1\bar{1}7)$, (208), (310), (020), (313) and (023). The measured positions of $(\bar{1}12)$ and (202) were taken to be the same since no peak splitting of $(102)_H$ was observed. The same was done for (205) and $(\bar{1}15)$. The difference between measured and calculated peak positions is always less than 0.10°, and usually less than 0.03°, even for the broad peaks in the monoclinic phase.

Figure 4.9 shows the unit cell parameters for $0<x<0.82$, measured during the x-ray experiment as Li is removed from $LiNiO_2$. For $0<x<0.15$ in $Li_{1-x}NiO_2$, the structure is the original hexagonal one, denoted by H_1. For $0.15<x<0.25$, the hexagonal H_1 and monoclinic M phases coexist. The circular and square data points for $0.15<x<0.25$ show unit cell parameters of the coexisting H_1 and M phases respectively. For $0.25<x<0.50$, only the M phase exists. Another two-phase region appears for $0.50<x<0.57$, where the monoclinic phase and a new hexagonal (H_2) phase coexist. For $0.57<x<0.68$, the only phase present is the hexagonal H_2 phase. Another hexagonal phase, H_3, appears with H_2 phase for $0.68<x<0.82$. The original peaks $(107)_H$, $(110)_H$ and $(113)_H$ shown in figure 4.7 and 4.8 split and become broad in the monoclinic phase, so it is difficult to locate these peak positions accurately in the monoclinic phase. Therefore the unit cell parameters in the monoclinic phase are not as accurate as those in the hexagonal phases. However, the $(107)_H$ peak shown in figure 4.7 clearly splits into two broad peaks with a 2:1 intensity, which correspond to the $(1\bar{1}7)_M$ and $(20\bar{7})_M$ peaks respectively in monoclinic phase. Similarly, the original $(113)_H$ also splits into two peaks, $(313)_M$ and $(023)_M$, with 2:1 intensity ratio. The original $(110)_H$ also shows a similar splitting in the monoclinic phase.

The peaks in dx/dV shown in figure 4.3 correlate well with the positions of the two-phase regions, except for the H_1---->M transition. Here, the transition appears to be kinetically hindered during the first charge, since the peak in dx/dV corresponding to this transition is weak compared to later cycles (see figure 4.3). On the first charge the peak in dx/dV is almost completed before we see good evidence for two-phase coexistence by x-ray diffraction. On latter cycles, this is not the case, and the peak in dx/dV correlates well with the two-

phase region. Figure 4.3 shows that during the first discharge of the cell, the lithium content apparently does not return to x=0 in $Li_{1-x}NiO_2$.

Figure 4.10 shows the volumes of the three hexagonal unit cells, and half of the volume of the monoclinic unit cell plotted versus x. The square data points are for the monoclinic phase, and the circular data points are for the three hexagonal phases. As Li is deintercalated from $Li_{1-x}NiO_2$, the volume becomes smaller. Four steps in the volume versus x graph clearly indicate the four phases in $Li_{1-x}NiO_2$.

Figure 4.11 shows a phase diagram for $Li_{1-x}NiO_2$. It is easy to determine the two-phase regions for H_1+M and H_2+H_3, since we find that Bragg peaks belonging to the different phases appear at the same time. On the other hand, the two-phase region for H_2+M is less apparent, since the Bragg peaks for the two-phases are not well separated. However, there must be a two-phase region because of the large peak in dx/dV(Berlinsky, Unruh, McKinnon and Haering) in that region (H_2+M peak in figure 4.3b), and because of the discontinuity of the unit cell parameters. To obtain the values of x for the end points of the two-phase regions, we have averaged the starting points of the plateaus measured during charge and discharge for the reversible cycles shown in figure 4.3. This is consistent with the unit cell results in figures 4.9 and 4.10.

Like $Li_{1-x}NiO_2$, $Li_{1-x}CoO_2$ also undergoes a phase transition from hexagonal to monoclinic for a certain range of x (Reimers and Dahn, J. Electrochem. Soc.). For $Li_{1-x}CoO_2$, the monoclinic phase appears in a narrow area around x=0.5, and the (110) reflection does not split into two peaks. This is different from the monoclinic distortion of $Li_{1-x}NiO_2$, where the basal plane of $Li_{1-x}NiO_2$ is distorted significantly. However, the monoclinic distortions of both

are consistent with the space group C2/m (Ohzuku, Ueda and Nagayama; Reimers and Dahn J. Electrochem. Soc.).

Table 4.1 lists the unit cell parameters versus x in $Li_{1-x}NiO_2$ for the three hexagonal phases and the monoclinic one. In order to compare with the other work, we (Li, Reimers and Dahn, 1993) also transform to the monoclinic axes used in previous work (Ohzuku, Ueda and Nagayama). There are some differences between our results and theirs. We observe the two-phase coexistence regions H_1+M and H_2+M, which are not shown in their data (see figure 12 in the reference Ohzuku, Ueda and Nagayama). Our values of β' differ slightly from those of Ohzuku et al. also. One reason is that the peak indexed as $(20\bar{7})_M$ here is indexed by Ohzuku et al as (003) in the monoclinic phase, which means it is originally from $(009)_H$. Since the intensity ratio $(107)_H/(009)_H$ is about 7:1 for $LiNiO_2$, the intensity of the $(20\bar{7})_M$ peak must be larger than that of the peak originally from $(009)_H$. Hence, we believe that our Miller index assignments are correct. Our data also have much less scatter, presumably because in situ techniques were used here.

In summary, $Li_{1-x}NiO_2$ undergoes three phase transitions between $x=0.0$ and x=0.82. These are hexagonal to monoclinic, monoclinic to hexagonal and hexagonal to hexagonal. Three coexisting phase regions are found, which correspond to three first-order phase transitions. The original $(101)_H$, $(107)_H$, $(110)_H$ and $(113)_H$ peaks each split into pairs of broad peaks between $0.25<x<0.50$, which is consistent with a hexagonal to monoclinic phase transition. The electrochemical properties clearly support the x-ray diffraction analysis, indicating three strong peaks in dx/dV in the three coexisting-phase regions.

Table 4.1. Lithium compositions, x, in $Li_{1-x}NiO_2$ at which in situ x-ray data were analyzed during the first charge of a $Li/LiNiO_2$ in situ x-ray cell. The measured lattice constants are also listed and the phases are designated. The numbers in brackets are the error value.

x in $Li_{1-x}NiO_2$	a (Å)	b(Å)	c(Å)	β (Degrees)	c'(Å)	β' (Degrees)	Phase
0.014(5)	2.883(3)		14.215(9)				
0.027(5)	2.881(3)		14.229(9)				
0.055(5)	2.878(3)		14.217(9)				
0.082(5)	2.873(3)		14.222(9)				
0.109(5)	2.872(3)		14.234(9)				H_1
0.150(5)	2.871(3)		14.234(9)				
0.178(5)	2.867(3)		14.233(9)				
0.205(5)	2.869(3)		14.241(9)				
0.232(5)	2.867(3)		14.239(9)				
0.205(5)	5.002(8)	2.842(5)	14.303(9)	90.45(8)	5.051(8)	109.28(8)	
0.232(5)	5.003(8)	2.841(5)	14.306(9)	90.50(8)	5.052(8)	109.29(8)	
0.273(5)	5.000(8)	2.838(5)	14.314(9)	90.52(8)	5.054(8)	109.27(8)	
0.314(5)	4.996(8)	2.832(5)	14.340(9)	90.56(8)	5.062(8)	109.22(8)	
0.342(5)	4.992(8)	2.832(5)	14.352(9)	90.48(8)	5.065(8)	109.19(8)	
0.369(5)	4.979(8)	2.829(5)	14.377(9)	90.51(8)	5.072(8)	109.11(8)	M
0.410(5)	4.955(8)	2.831(5)	14.416(9)	90.45(8)	5.081(8)	108.98(8)	
0.437(5)	4.950(8)	2.830(5)	14.410(9)	90.43(8)	5.079(8)	108.97(8)	
0.478(5)	4.952(8)	2.820(5)	14.466(9)	90.50(8)	5.097(8)	108.91(8)	
0.519(5)	4.944(8)	2.820(5)	14.469(9)	90.45(8)	5.097(8)	108.87(8)	
0.547(5)	4.924(8)	2.824(5)	14.443(9)	90.21(8)	5.086(8)	108.83(8)	
0.519(5)	2.826(3)		14.445(9)				
0.547(5)	2.828(3)		14.416(9)				
0.574(5)	2.825(3)		14.371(9)				
0.615(5)	2.826(3)		14.397(9)				
0.656(5)	2.825(3)		14.386(9)				H_2
0.683(5)	2.824(3)		14.393(9)				
0.711(5)	2.823(3)		14.400(9)				
0.752(5)	2.824(3)		14.401(9)				
0.793(5)	2.822(3)		14.409(9)				
0.820(5)	2.825(3)		14.427(9)				
0.752(5)	2.820(3)		13.525(9)				
0.793(5)	2.819(3)		13.450(9)				H_3
0.820(5)	2.821(3)		13.434(9)				

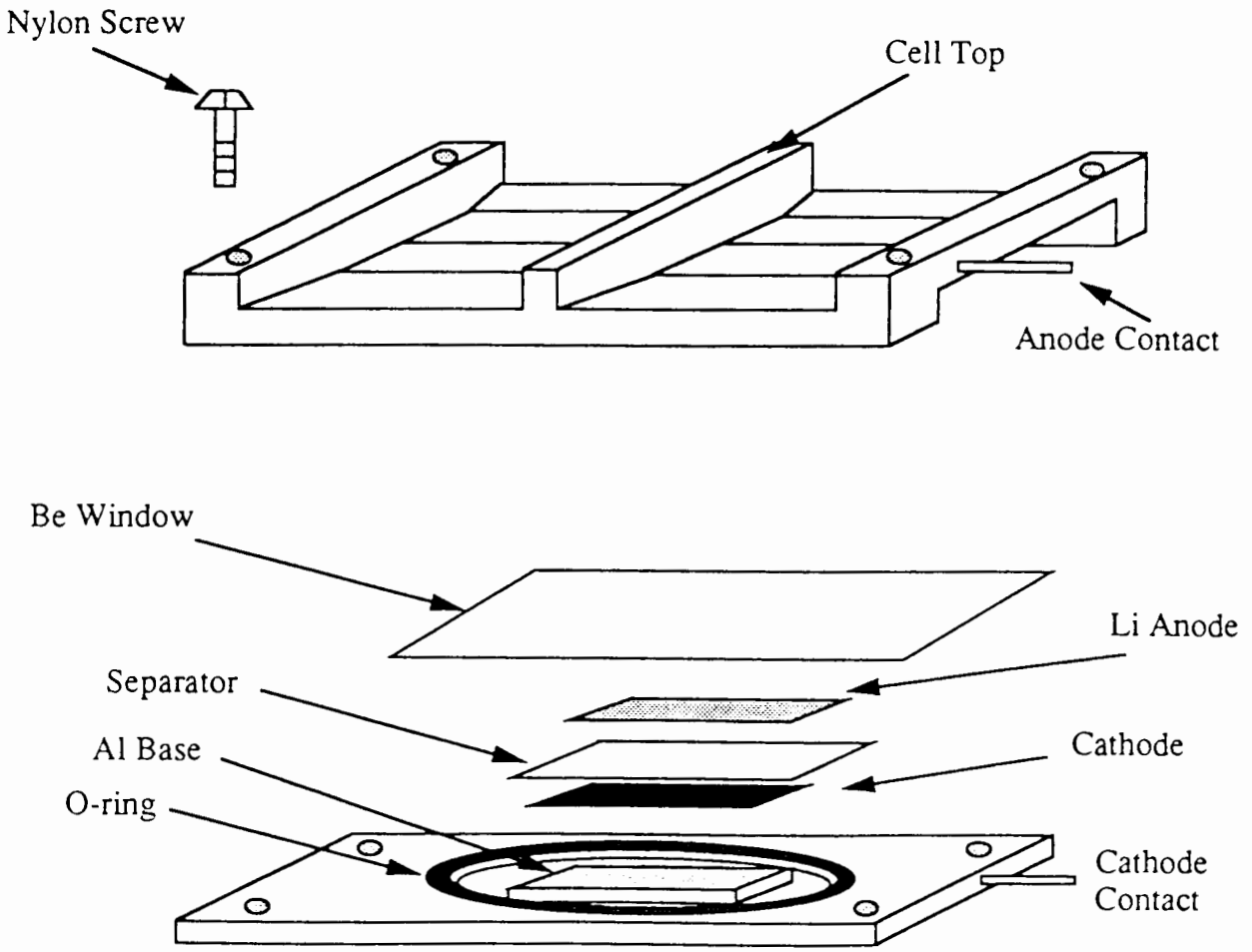

Figure 4.1. Schematic drawing of the in situ x-ray cell with the cell top, beryllium window, lithium anode, separator, cathode, aluminum base, O-ring and nylon screws. The x-rays penetrate through the beryllium window, lithium foil, and separator to the cathode. The aluminum base is the same size as the cathode to minimize any residual current and possible corrosion.

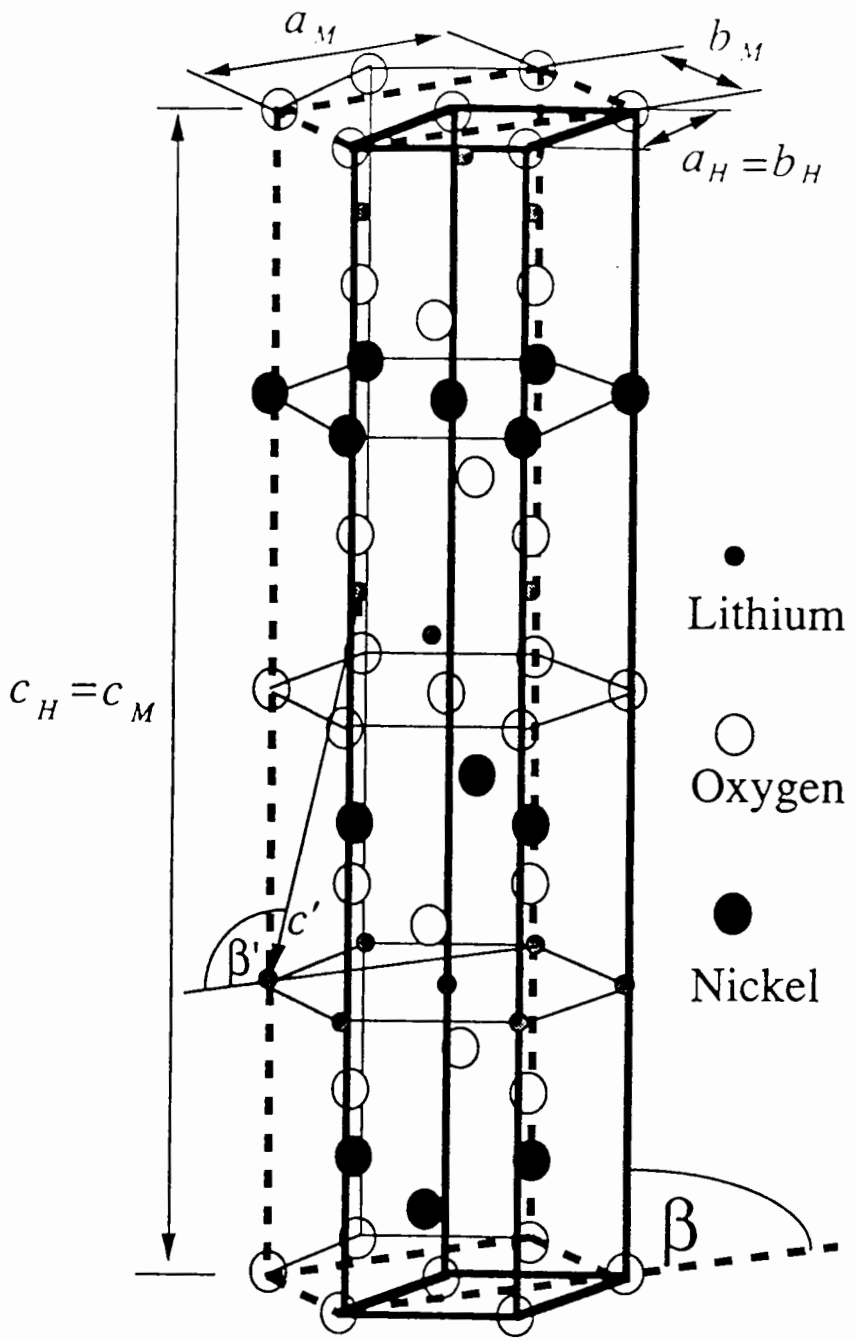

Figure 4.2. Crystal structure of $LiNiO_2$. Thick lines indicate the primitive unit cell in the hexagonal structure. The dashed thick lines outline the monoclinic unit cell. The volume of the monoclinic unit cell is twice the volume of hexagonal unit cell. The *c*-axis (labelled *c'*) and special angle (β') used by Ohzuku et al. is also shown.

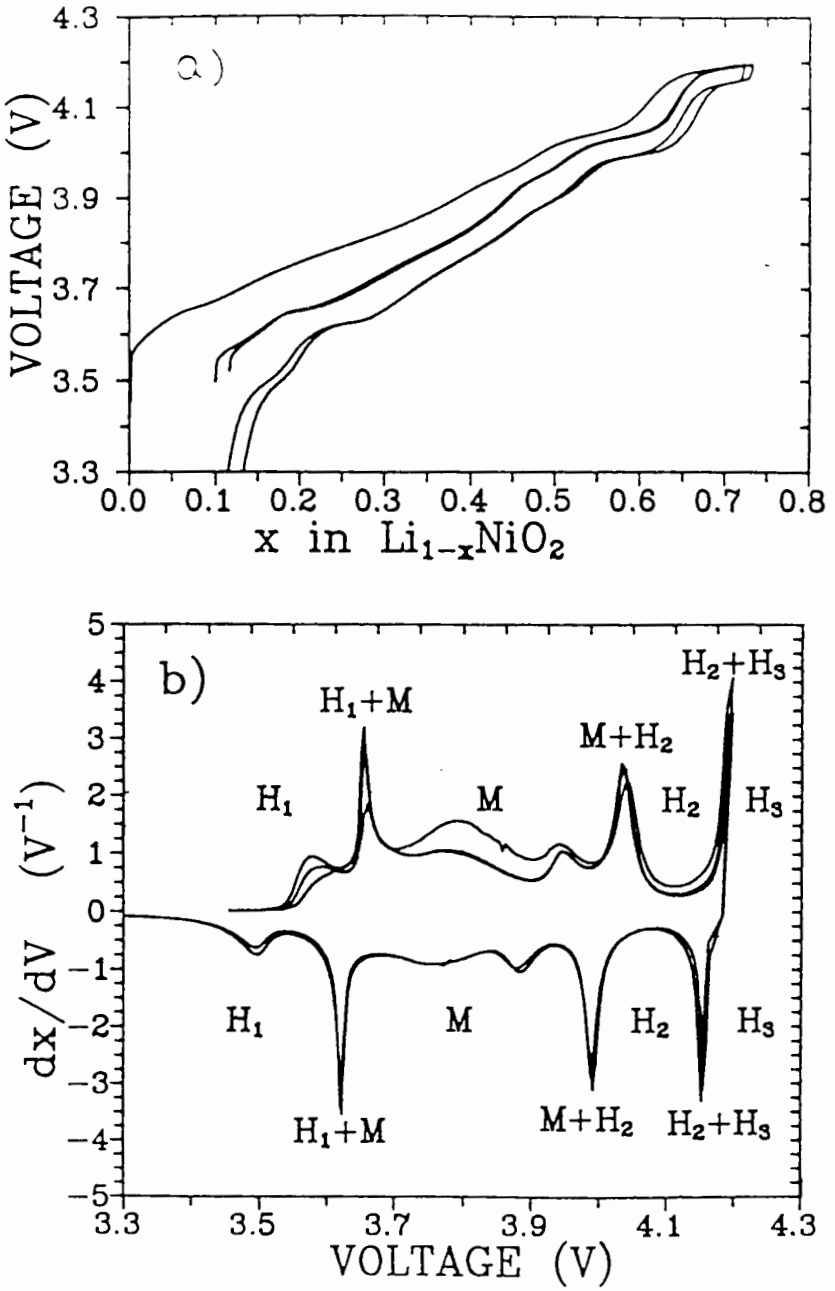

Figure 4.3 The charge and discharge curves as measured in a $Li/LiNiO_2$ coin cell for the first two cycles. A 100 hour rate was used at 30°C. The corresponding data collected for the x-ray cell is essentially the same as those of the coin cells. (b) The derivative, dx/dV, plotted versus V for the cycles shown in (a).

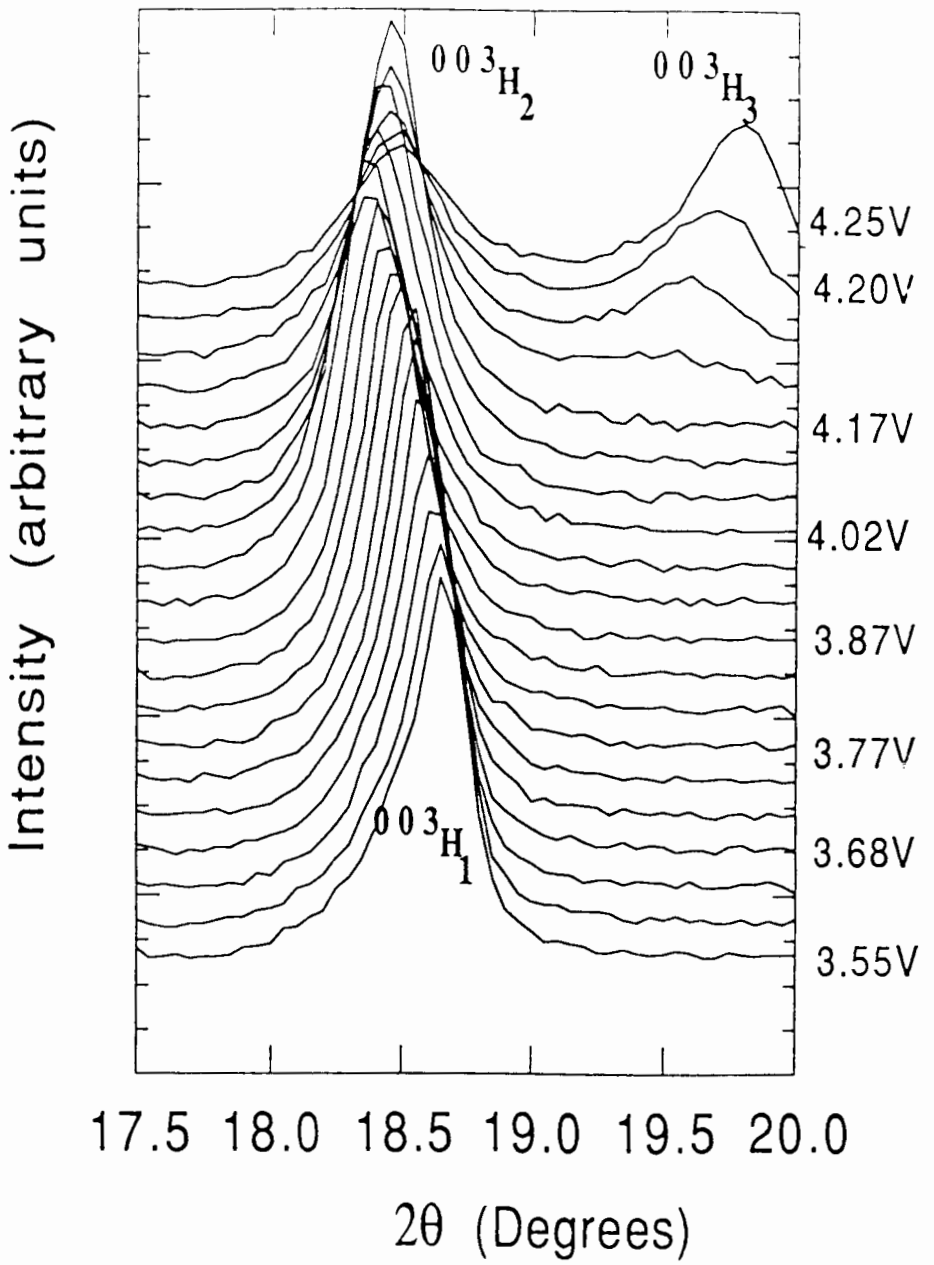

Figure 4.4. In situ x-ray scans of the original $(003)_H$ reflection over the voltage range $3.55 \leq V \leq 4.25$ V during the first charge of a $Li/Li_{1-x}NiO_2$ cell.

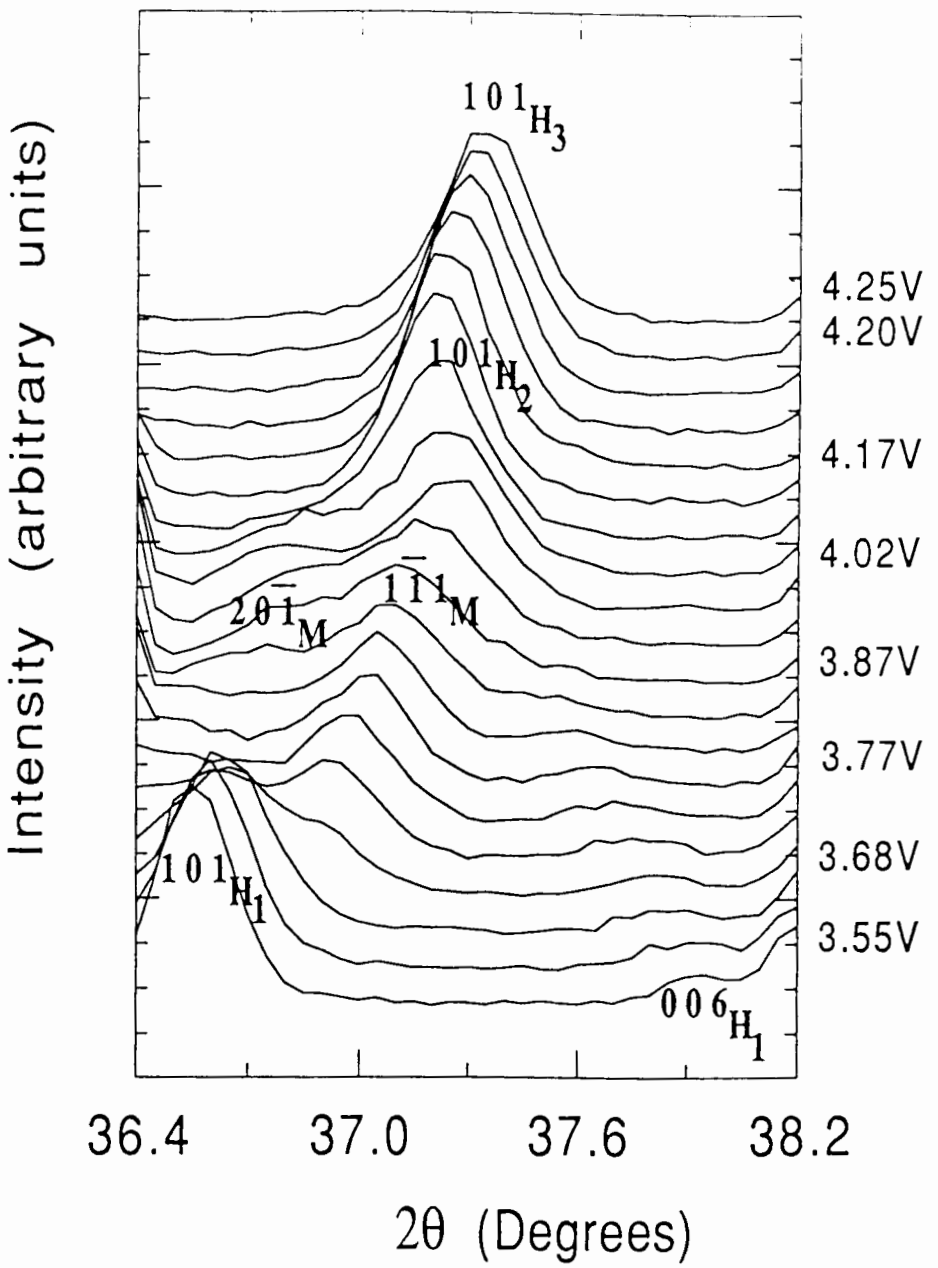

Figure 4.5. In situ x-ray scans of the original $(101)_H$ and $(106)_H$ reflections over the voltage range $3.55 \leq V \leq 4.25$ V during the first charge of a $Li/Li_{1-x}NiO_2$ cell.

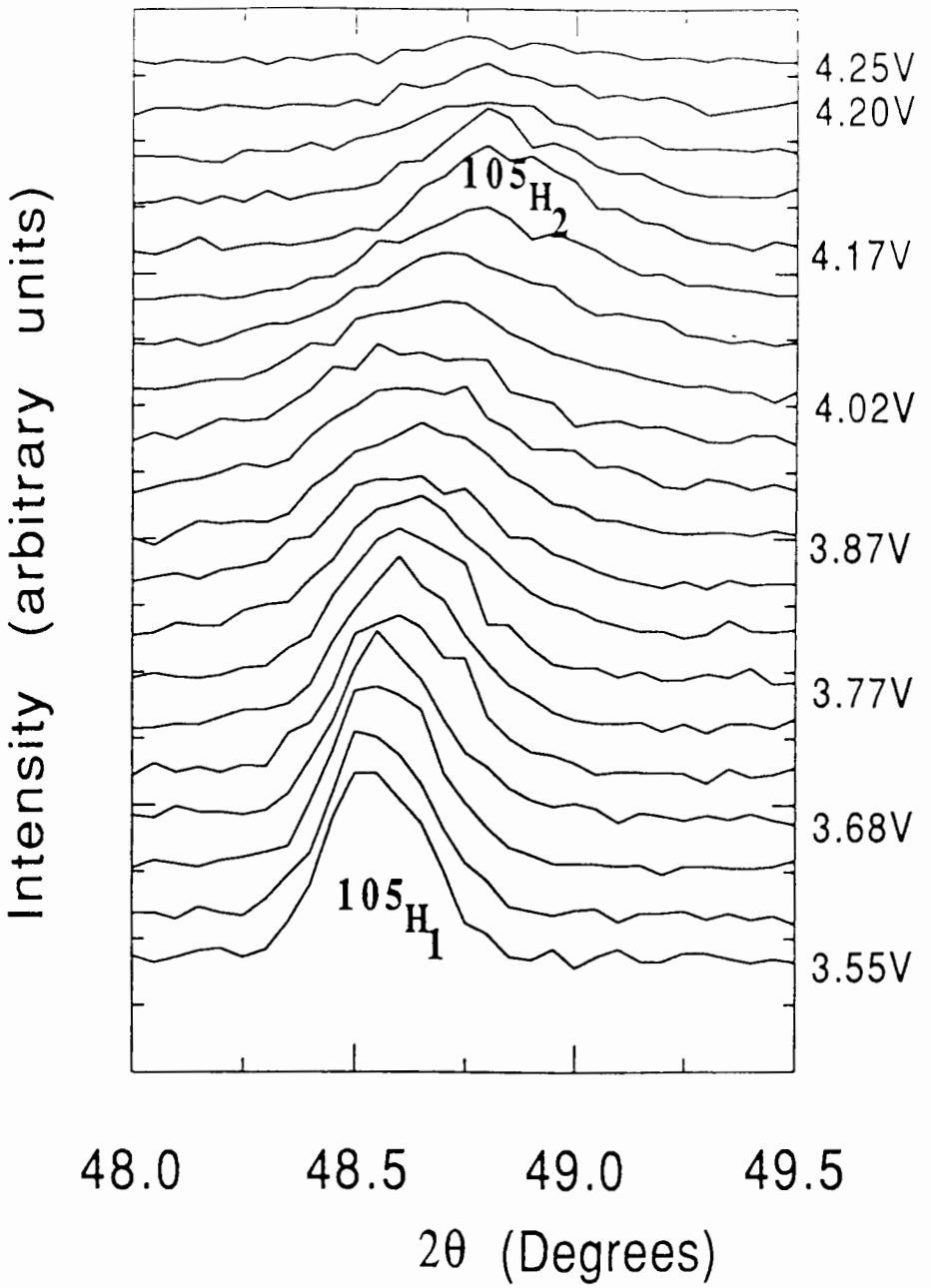

Figure 4.6. In situ x-ray scans of the orignial $(105)_H$ reflection over the voltage range $3.55 \leq V \leq 4.25$ V during the first charge of a $Li/Li_{1-x}NiO_2$ cell.

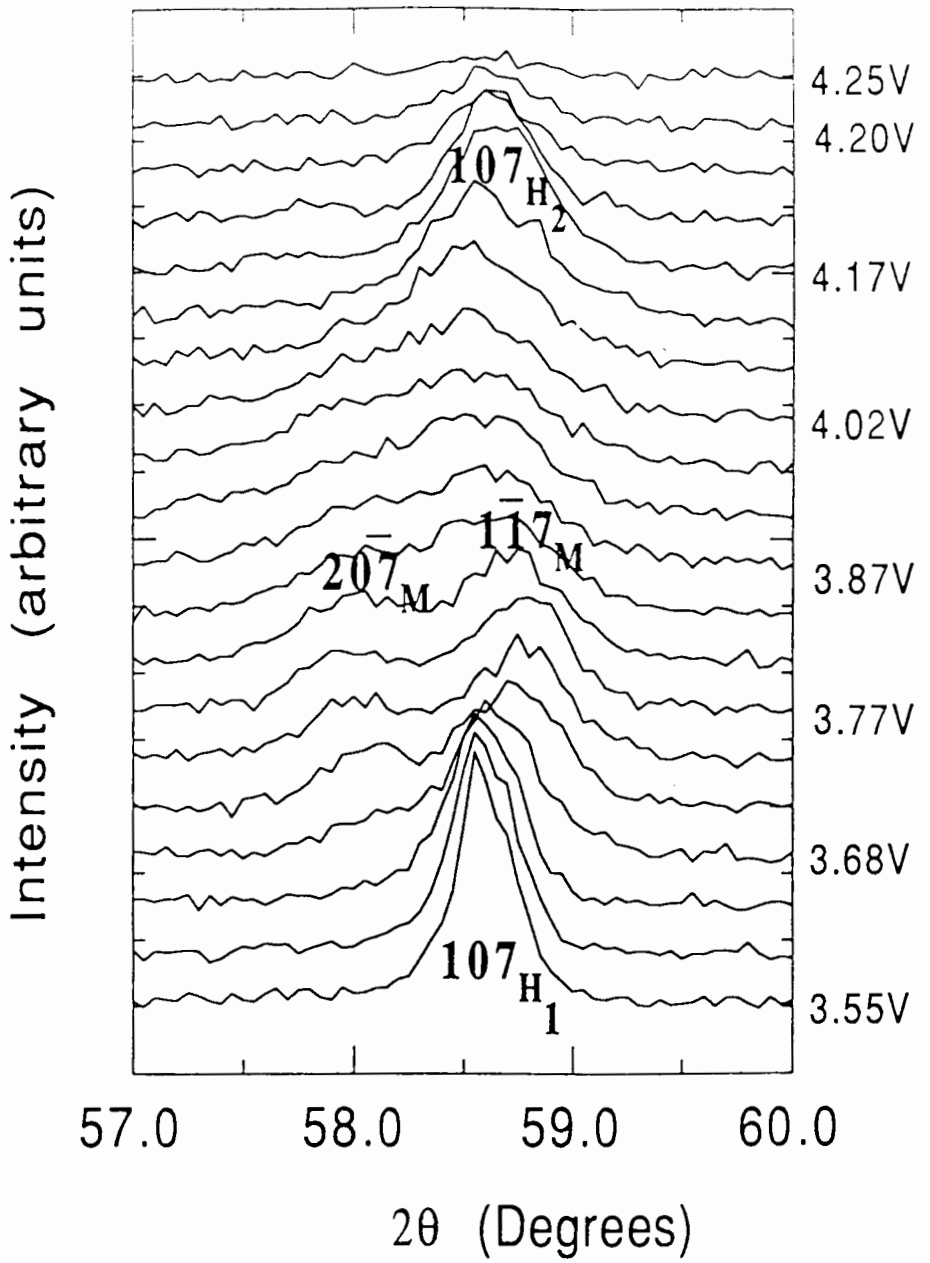

Figure 4.7. In situ x-ray scans of the original $(107)_H$ over the voltage range $3.55 \leq V \leq 4.25$ V during the first charge of a $Li/Li_{1-x}NiO_2$ cell.

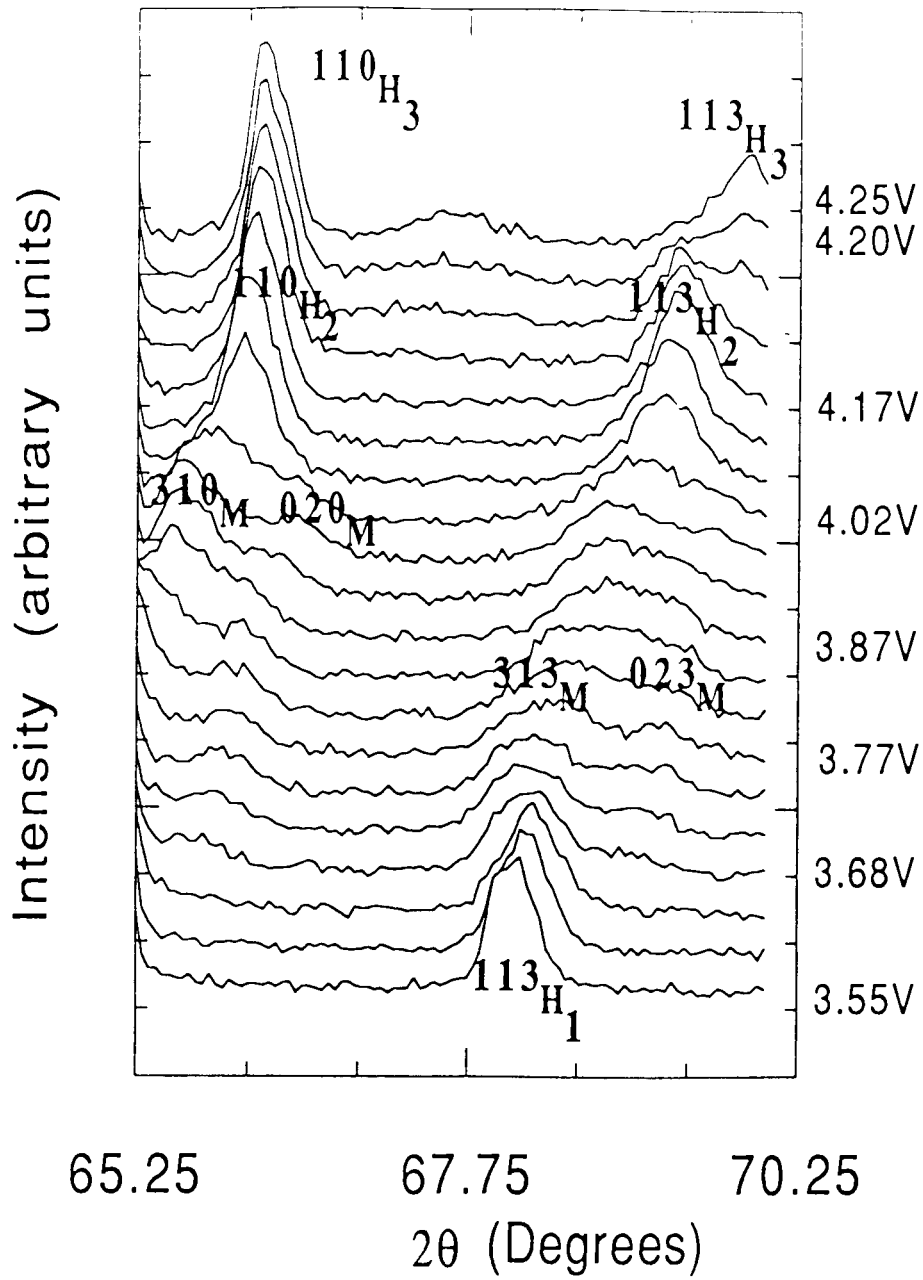

Figure 4.8. In situ x-ray scans of the original $(110)_H$ and $(113)_H$ reflections over the voltage range $3.55 \leq V \leq 4.25$ V during the first charge of a $Li/Li_{1-x}NiO_2$ cell.

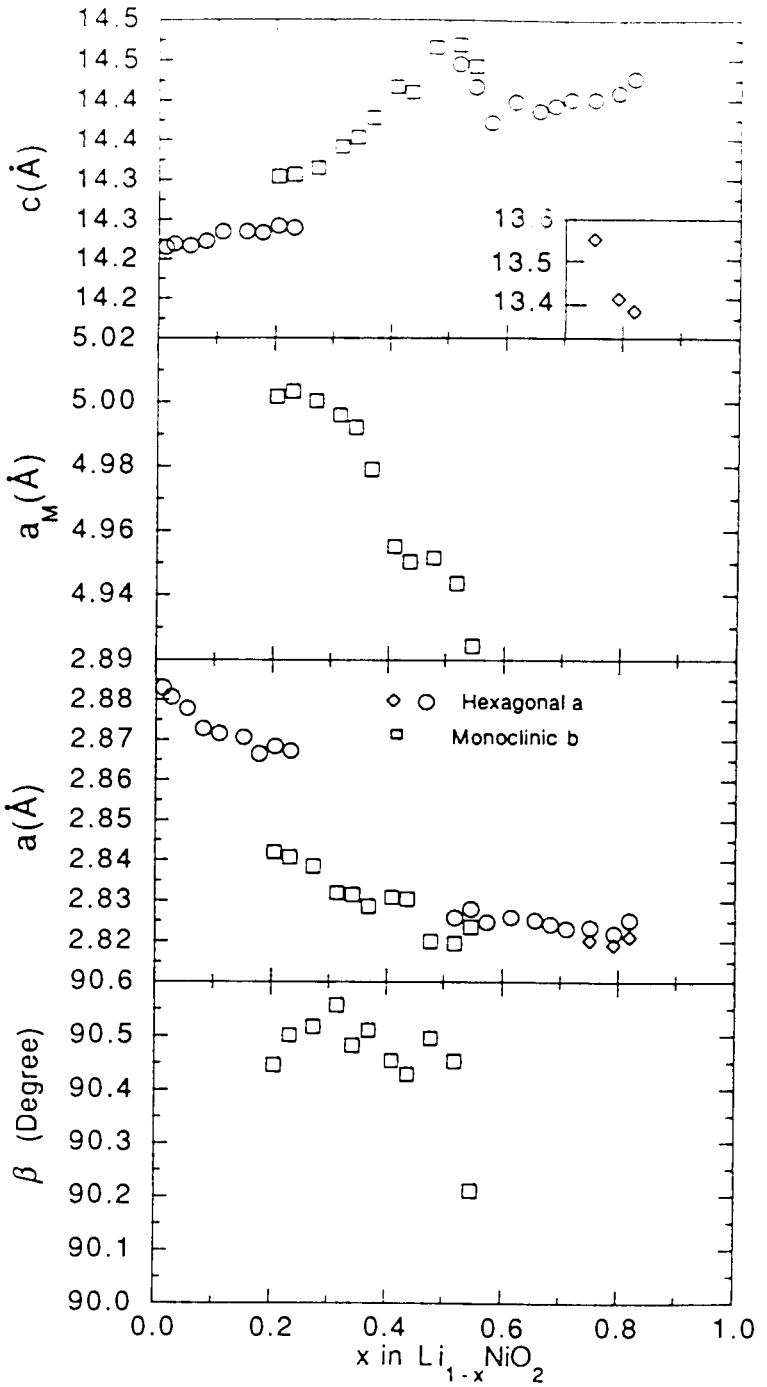

Figure 4.9. Variation of the unit cell parameters for the three hexagonal phases and one monoclinic phase observed in $Li_{1-x}NiO_2$ as a function of composition x. The hexagonal phase cell constants (c and a) are indicated with circles and diamonds, and the monoclinic phase (a_M, b_M, c_M, β) with squares.

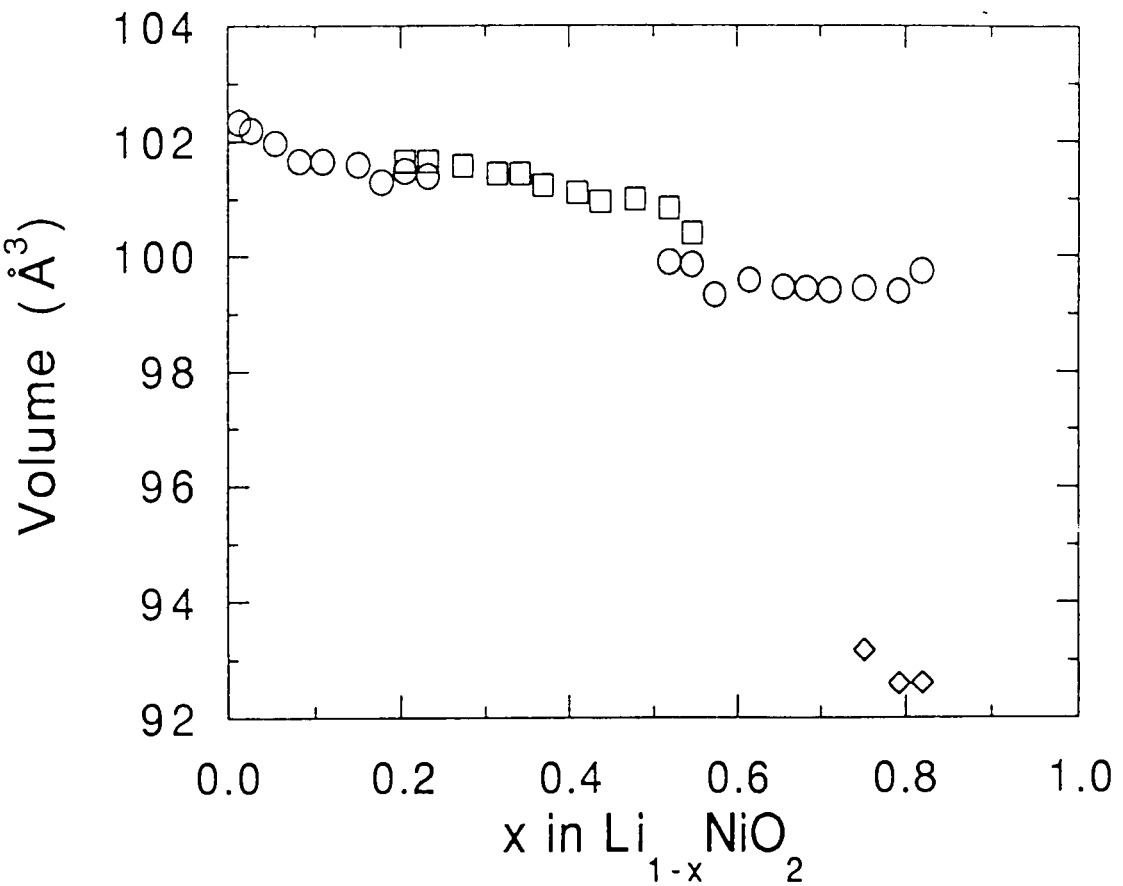

Figure 4.10. The hexagonal cell volume (circles and diamonds) and half of the monoclinic cell volume (squares) as a function composition x in $Li_{1-x}NiO_2$.

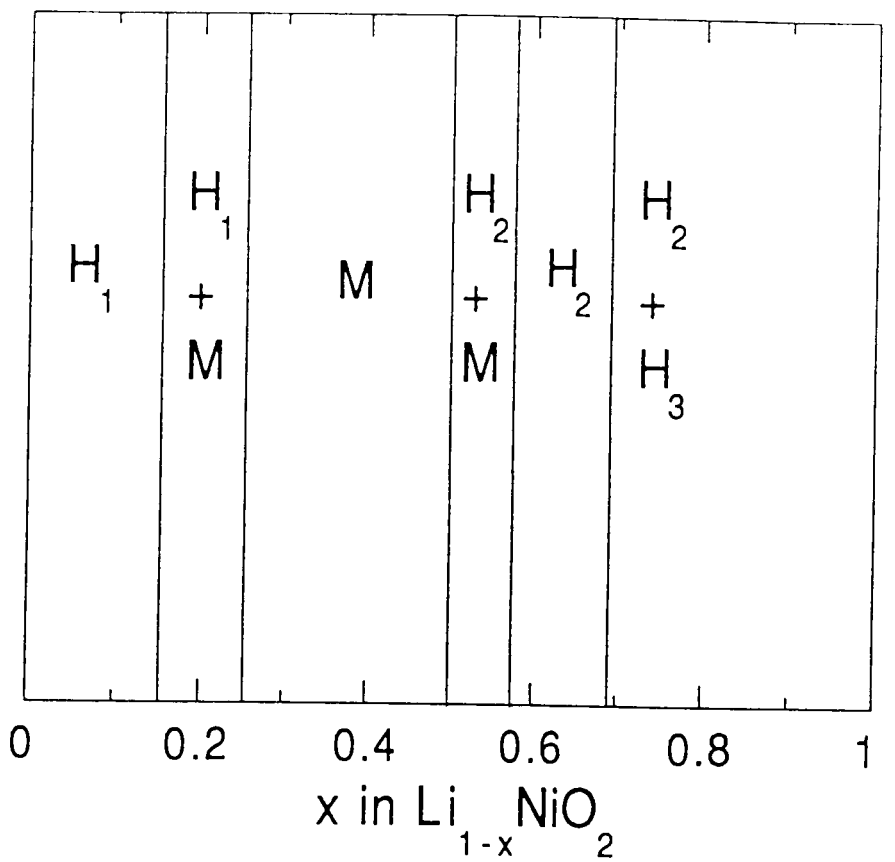

Figure 4.11. Room temperature phase diagram of $Li_{1-x}NiO_2$ showing the three single phase regions and the three coexisting phase regions.

Chapter 5. Lithium Intercalation from Aqueous Solutions

5.1 Theory

Lithium can be intercalated into a wide variety of materials using non-aqueous electrochemical cells. The use of aqueous methods is less common because of the reactivity of many lithium intercalation compounds with water. As introduced in Chapter 1, it may be better to use $Li_2Mn_2O_4$ to replace $LiMn_2O_4$ in rechargeable lithium-ion batteries. However, there was no convenient method to make $Li_2Mn_2O_4$ for lithium-ion cell applications. Here we use a new method involving lithium intercalation from aqueous solutions (Li, McKinnon and Dahn) to make $Li_2Mn_2O_4$. Other lithium transition metal oxides with high lithium contents can possibly be made for lithium-ion cell cathodes by this method.

The materials must be stable in aqueous solutions in order to be made in the solutions. Therefore, we first consider the stability of lithium intercalation compounds in aqueous alkaline solution. Then we describe the aqueous electrochemical cell we use to make $Li_2Mn_2O_4$. We show by X-ray diffraction, chemical analysis and electrochemical testing that it is possible to make $Li_2Mn_2O_4$ from $LiMn_2O_4$ in aqueous solution. Finally, we show test results for our $Li_2Mn_2O_4$ in non-aqueous Li electrochemical cells.

As shown in figure 1.3, it is well known that many lithium transition metal oxide compounds are stable in air and water (e. g. $LiMn_2O_4$, $LiNbO_3$ etc.) while others, (e. g. $LiMoO_2$, $LiWO_2$ etc.) are not. We must consider the stability of lithium transition metal oxide intercalation compounds in water

and in LiOH solutions. Following McKinnon and Haering we define the chemical potential, μ_{Li}^{int} of intercalated Li in Li_x(Host) as

$$\mu_{Li}^{int}(x) = \frac{1}{N_A}\left(\frac{\partial G^0_{Li_x(Host)}}{\partial x}\right)_{T,P}$$

where $G^0_{Li_x(Host)}$ is the Gibbs free energy of one mole of Li_x(Host) in its standard (solid) state and N_A is Avagadro's number. Integrating, we have

$$G^0_{Li_x(Host)} = G^0_{Host} + \int_0^x N_A \mu_{Li}^{int}(x)dx$$

where G^0_{Host} is the Gibbs free energy of Host in its standard state. McKinnon and Haering showed that the voltage, V(x), of a Li/Li_x(Host) intercalation cell is given by (1.1), which is rewritten here

$$V(x) = -\frac{1}{e}(\mu_{Li}^{int}(x) - \mu_{Li}^0) \qquad (5.1)$$

where μ_{Li}^0 is the chemical potential of Li in Li metal ($\mu_{Li}^0 = (\partial G_{Li}^0/\partial N)_{T,P}$) and e is the magnitude of the electron charge.

Assume we are given an intercalation compound, Li_x(Host) containing Li at some chemical potential, $\mu_{Li}^{int}(x)$. The compound is placed in water. Here, we assume that there is so much compound relative to water that x does not change appreciably when the compound reacts with water, and so $\mu_{Li}^{int}(x)$ does not vary. As intercalated Li reacts with water, the Li^+ concentration increases and the pH rises as more OH^- forms. What is the equilibrium value of the pH, or alternatively at what value of the pH will the Li no longer deintercalate from the compound?

In equilibrium, the following reaction holds

$$\text{Li(intercalated)} + H_2O \leftrightarrow Li^+ + OH^- + (1/2)H_2. \qquad (5.2)$$

Presumably, little bubbles of H_2 will form over the surface of the Li_x(Host) compound, so H_2 will be at approximately 1 atmosphere pressure, in its standard state. Therefore, in equilibrium

$$\mu_{Li}^{int}(x) + \mu_{H_2O}^0 = \mu_{OH^-} + \mu_{Li^+} + (1/2)\mu_{H_2}^0 \qquad (5.3)$$

In equation (5.3), $\mu_{H_2O}^0$ is the chemical potential of water in its standard state, μ_{OH^-} and μ_{Li^+} are the chemical potentials of OH^- and Li^+ in solution respectively, and $\mu_{H_2}^0$ is the chemical potential of H_2 in its standard state.

Charge conservation requires that

$$[Li^+] + [H^+] = [OH^-]$$

where $[Li^+]$ is the concentration of Li^+ in moles per liter. Provided the added water has pH=7, the solution will become basic, so that

$$[Li^+] >> [H^+].$$

Thus, we approximate

$$[Li^+] = [OH^-] \; . \qquad (5.4)$$

The chemical potentials of OH^- and Li^+ in solution depend on concentration through the Nernst equation, (assuming full dissociation) i. e.

$$\mu_{Li^+} = \mu_{Li^+}^0 + kT\ln[Li^+] \qquad (5.5a)$$

$$\mu_{OH^-} = \mu_{OH^-}^0 + kT\ln[OH^-] \qquad (5.5b)$$

where $\mu^0_{Li^+}$ and $\mu^0_{OH^-}$ are the chemical potentials of Li^+ and OH^- respectively in 1 molar solution. k is Boltzmann's constant and T is the Kelvin temperature. Combining equations (5.3), (5.4) and (5.5) we obtain

$$2kT\ln[OH^-] = \mu^{int}_{Li}(x) + \mu^0_{H_2O} - \mu^0_{OH^-} - \mu^0_{Li^+} - (1/2)\mu^0_{H_2}. \qquad (5.6)$$

We now recall the definition of pH

$$pH = -\log_{10}[H^+]. \qquad (5.7)$$

Equation (5.7) and $[OH^-][H^+]=10^{-14}$ are used with equation (5.6) to give

$$0.118pH = 1.657 + \mu^{int}_{Li}(x) + \mu^0_{H_2O} - \mu^0_{OH^-} - \mu^0_{Li^+} - (1/2)\mu^0_{H_2} \qquad (5.8)$$

where we have substituted kT=0.0257 eV/atom at 25°C. The units of all terms in equation (5.8) are in eV/atom. The term involving chemical potentials in equation (5.8) is easily evaluated from thermodynamic tables. Using equation (5.1), we get

$$\mu^{int}_{Li}(x) = \mu^0_{Li} - eV(x).$$

Substituting this into (5.8) gives a term

$$\mu^0_{Li} + \mu^0_{H_2O} - \mu^0_{OH^-} - \mu^0_{Li^+} - (1/2)\mu^0_{H_2}$$

This term is minus the partial molar free energy change for the reaction

$$Li_{(s)} + H_2O_{(l)} \rightarrow LiOH_{(aq,1M)} + \frac{1}{2}H_{2(g,STP)}.$$

The free energy change for this reaction is -51.23 Kcal/mole or -2.228eV/atom. Substituting in (5.8) gives

$$0.118pH=1.657-eV(x)+2.228.$$

Solving for V(x), gives the result

$$V(x)=3.885-0.118pH \text{ (volts)} \qquad (5.9)$$

What is the significance of equation (5.9)? Lithium intercalated Hosts, Li_x(Host) which have a voltage, V(x), versus Li placed in contact with H_2O will react and the resulting pH will be given by the solution of equation (5.9).

Therefore, we expect $Li_2Mn_2O_4$ which has V=2.97V versus Li metal (Tarascon), to be stable in aqueous LiOH solutions with pH greater than about 8, provided there is no oxygen or CO_2 in the environment. Equation 5.2 suggests that high LiOH concentrations and high H_2 pressures can cause intercalation of Li in solids in aqueous solution. However, the use of high hydrogen pressures can sometimes lead to safety concerns, and therefore this is discouraged.

An alternative to equation (5.9) is an expression for the molarity of the LiOH solution where a compound Li_x(Host) with voltage $V(x)$ is in equilibrium. Starting from equations (5.4) and (5.6), we find

$$V(x)=2.23-2kTln[Li^+] \text{ (Volts)} \qquad (5.10)$$

If $V(x)>2.23-2kTln[Li^+]$, no Li will deintercalate from Li_x(Host) and Li_x(Host) will be stable in the alkaline solution. Therefore $Li_2Mn_2O_4$ is stable in a 1 Molar aqueous LiOH solution.

The results given by equation 5.9 and 5.10 are important and deserve some further consideration (Li, McKinnon and Dahn). Bockris and Reddy discuss the oxygen and hydrogen evolution reactions which occur in aqueous

electrolytes in detail. Figure 5.1 shows the stability window of H_2O as a function of pH in solutions with 1 *M* Li^+ ion concentration. When the Li^+ ion concentration is 1 *M*, the potential of Li--->$Li^+ + e^-$ can be located on the figure using standard tables (Weast and Astle). Since the voltage of $Li_2Mn_2O_4$ is about 2.97 V (Tarascon and Guyomard) versus metallic Li, it can also be located on figure 5.1. Thus we expect $Li_{1+x}Mn_2O_4$ to be stable in aqueous solutions with $[Li^+]$=1 *M* at pH's as low as 2. When $[Li^+] \neq 1$ *M*, as in the case when a lithium intercalation compound is added to pure water, then the situation changes. As we have shown in the derivation of equations 5.9 and 5.10, it is reasonable to assume $[Li^+]=[OH^-]$ in this case.

Figure 5.2 shows the relevant H_2O stability diagram when $[Li^+]=[OH^-]$ obtained using the results of equations 5.9 and 5.10. In this case the potential of the Li electrode drops with respect to S.H.E. (Standard Hydrogen Electrode), as does that of $Li_2Mn_2O_4$ as the pH decreases. The potential of $Li_2Mn_2O_4$ moves closer to the H_2 evolution line as the pH is decreased and crosses it near pH=8. Therefore $Li_2Mn_2O_4$ will not be stable in water below pH=8. If a process is considered where $Li_2Mn_2O_4$ is to be purified by extended rinsing with fresh water, this rinsing step will remove lithium from the compound. Figure 5.2 is therefore complementary to equations (5.9) and (5.10).

Now let us consider an aqueous electrochemical cell for intercalating Li into $LiMn_2O_4$. Figure 5.3 shows a schematic of what such a cell could look like. Current is passed to the carbon electrode where oxygen evolution occurs by the reaction.

$$2OH^-(aq) \text{-----} > H_2O + (1/2)\,O_2(g) + 2e^- \qquad (5.11)$$

At the $LiMn_2O_4$ electrode, the reaction

$$xe^- + xLi^+ + LiMn_2O_4 \text{ ----} > xLi_2Mn_2O_4 + (1-x)LiMn_2O_4 \qquad (5.12)$$

occurs. Figure 5.4 shows how the voltage of the aqueous cell varies with charge passed between the electrode in the direction indicated in figure 5.3 assuming a 1 *M* LiOH electrolyte and V(x)=2.97 V. Eventually, however, the formation of $Li_2Mn_2O_4$ will be complete and V(x) will drop below 2.23 V, if current continues to flow. When this occurs hydrogen evolution may occur. This reaction can also be placed relative to the standard hydrogen electrode, as has been done in figure 5.4. Alternatively, some other reaction could occur as we discuss below.

When hydrogen evolution does not occur at V(x)>2.23V, the Li^+ ion concentration is much higher than the H^+ concentration in 1M LiOH aqueous solution which makes Li^+ ion intercalation the favored process. When hydrogen evolution occurs at V(x)<2.23V, there is also significant probability for finding H^+. Therefore ion exchange between H^+ and Li^+ must be considered. Further reduction of $Li_2Mn_2O_4$ may give

$$Li_2Mn_2O_4+4H_2O+2e^- \text{ ---- } >2Mn(OH)_2 +2\ Li^+ + 4OH^- \qquad (5.13)$$

or

$$2H_2O+2e^- \text{ ----> } 2OH^- +H_2(g) \qquad (5.14)$$

Although the Li^+ concentration is much higher than the H^+ concentration, it does not mean that Li^+ are certain to intercalate within the host instead of H^+. The system may have lower free energy with H^+ in the host sites instead of Li^+ like in equation (5.13), or there may be H_2 evolution instead of Li^+ intercalation like in equation (5.14). Experiments using neutron scattering described in sections 5.2 and 5.3 suggest that $Mn(OH)_2$ is formed during the over-reaction of $Li_2Mn_2O_4$.

In theory, we have shown that it should be possible to intercalate Li into high voltage (>2.3V) hosts from concentrated aqueous lithium salt solutions. We will demonstrate that this is true in the Results section. Figure 5.1 predicts that very high voltage hosts (with V(x) ≥3.5V) will spontaneously intercalate Li from LiOH solution with simultaneous evolution of O_2. Kanoh et al (Kanoh, Feng, Miyai and Ooi) found the reaction:

$$xLi^+(aq)+xOH^-(aq)+\lambda\text{-}MnO_2\text{----}>Li_xMnO_2+(x/2)H_2O+(x/4)O_2(g). \quad (5.15)$$

occurred for λ-MnO_2 in LiOH solution. λ-MnO_2 has V(x)≈4.1V>3.5V (Hunter; Tarascon and Guyomard).

5.2 Experimental

Figure 5.3 shows a sketch of the aqueous electrochemical cell used to prepare $Li_2Mn_2O_4$ from $LiMn_2O_4$. Carbon rods were used as the positive electrode and titanium bars for the negative electrode current collectors. The cell container was a pyrex beaker.

$LiMn_2O_4$ was prepared by reacting manganese dioxide (CMD, Chemetals) and Li_2CO_3 in air at 750°C (Manev, Momchilov, Nassalevska and Kozawa). The lattice constant was 8.246 Å and the material was a single phase as determined by x-ray diffraction.

$LiMn_2O_4$ electrodes were pasted onto the titanium collectors. The paste was a mixture of $LiMn_2O_4$, 10 % by weight carbon black, (Super S, Chemetals) 3 % by weight polyvinylidene flouride and N-methyl pyrrolidinone (NMP) solvent. The paste was spread on two titanium plates which were drilled with holes. Spreading the paste into the holes helps to make a good bond between the electrode ingredients and the Ti collector. The two titanium plates were then clamped together to make a Ti-$LiMn_2O_4$-Ti sandwich. The paste was then dried by placing the assembly in a drying oven at 105°C in air while NMP was evaporated. Typical electrodes used 4.0 grams of $LiMn_2O_4$ powder and had an area of 5.0x3.5 cm^2. The thickness of the starting material layer between the two titanium plates was about 4mm.

The $LiMn_2O_4$ electrode sandwiched between the Ti plates and the carbon counter electrode was immersed to a depth of about 70 mm in the electrolyte in the pyrex beaker and the beaker was covered with a lucite lid. The distance between electrodes was typically about 25 mm. The beaker was then placed in

a temperature controlled oil bath. Temperatures between 16°C and 100°C could be attained. The electrodes were connected to a current supply. Currents between 3 and 40 mA were applied to the cell. The constant currents were applied from 24 hours to 240 hours, depending on the batch of material prepared. The voltages between the positive and the negative electrodes were recorded during the electrochemical reaction. For some cells, a Ag/AgCl reference electrode (+0.222V vs. S.H.E.) was included to confirm our proposed cell reactions and to identify the sources of cell overvoltage. The number of electrons transferred between the two electrodes was calculated from the current, the mass of $LiMn_2O_4$ and the current duration.

After the aqueous electrochemical reaction, the Ti sandwich electrode was disassembled and the reacted powder was rinsed in ethanol. The solubility of LiOH in ethanol is low, so this step removes little lithium if done quickly. The powder was then dried between 80°C and 110°C under vacuum. The powder was then measured by x-ray diffraction in air and evaluated in non-aqueous Li electrochemical cells.

Electrochemical test cells were prepared using 2325 coin cell hardware as described in the reference (Dahn, Sleigh, Shi, Reimers, Zhong and Way). The separator was Celgard 2502 microporous film which had been wetted with 1M $LiClO_4$ in a 50/50 volume percent mixture of Propylene Carbonate (PC) and Ethylene Carbonate (EC) respectively. The separator was wetted using a vacuum/pressure cycle. Cathodes were made in air from the $Li_2Mn_2O_4$ powder and the Super S carbon black (10% by weight) from the original starting materials. No further carbon was added at this stage. The $Li_2Mn_2O_4$ and the carbon black were added to a solution of 4 % EPDM in cyclohexane such that 3 % of the final electrode mass would be EPDM. Excess cyclohexane

was then added until the slurry reached a smooth syrupy viscosity. The slurry was then spread on the Al foil using a doctor blade spreader and the cyclohexane evaporated at room temperature in air. Once the electrode had dried, it was compressed between flat plates at about 25 bar pressure. Test electrodes of dimension 1.2x1.2 cm^2 having thickness 100 microns were then weighed and the weight of the foil, the EPDM and the PVDF (from the aqueous treatment) and the carbon black were subtracted to obtain the active electrode mass. The entire fabrication step was carried out as quickly as possible. The electrodes were transferred to an argon filled glove box within 30 minutes of the start of their fabrication to limit reaction with air.

All cell construction and sealing with non-aqueous electrolytes was done in an Argon-filled glove box. After construction, the cells were removed from the glove box and cycle tested using constant current cyclers. Currents were adjusted to be 2.8mA/gram of active material for all tests.

As a further test of some of the materials formed, we studied some by neutron diffraction. Neutron diffraction is sensitive to light elements like lithium and deuterium, and can distinguish between the incorporation of hydrogen (deuterium) or lithium. Hydrogen has a large incoherent neutron scattering cross-section (Bacon) which leads to very high backgrounds in hydrogen containing specimens. Deuterium displays the same chemistry as hydrogen but does not have a large incoherent cross-section. The coherent neutron scattering length for Li is -0.233×10^{-12}cm, while for D it is $+0.677 \times 10^{-12}$cm, so it is easy to distinguish Li from D in diffraction measurements.

We used D_2O as a solvent, γ–$Li_{0.36}MnO_2$ as the starting electrode material, teflon binder which contains no H atoms, and $LiOH \cdot H_2O$ salts to decrease

the concentration of H, which may be in the final products. We therefore minimize the neutron scattering background from H atoms by replacing H atoms with as many D atoms as possible. In order to investigate the formation of $Mn(OD)_2$, we over reacted the starting materials γ–$Li_{0.36}MnO_2$ to $e/Mn=1.0$, to reach the low voltage plateau near $V(x)<2.23$ V (e/Mn is the number of electrons transferred per Mn atom). A charge transfer only $e/Mn=0.64$ is necessary to form $LiMnO_2$ from γ–$Li_{0.36}MnO_2$.

Neutron scattering experiments were performed at the Dualspec powder diffractometer at AECL Chalk River. Samples of about 5 grams were held in thin-walled vanadium cylindrical cans of 3/8" diameter. The Dualspec diffractometer uses an 800 position wire detector which spans an 80 degree range in scattering angle in steps at 0.1°. We positioned the detector in 4 positions, ϕ_0=5.00°, 5.05°, 40.00° and 40.05° for each specimen to obtain data from 5° to 120° in steps of 0.05°. A typical data set took 2 hours to collect. A neutron wavelength of 1.29902Å was used.

5.3 Results and Discussion

Figure 5.5a shows the terminal voltage of an aqueous carbon/$LiMn_2O_4$ cell, plotted versus the number of electrons transferred per Mn atom. Figure 5.5b shows the voltage of the $LiMn_2O_4$ electrode versus S.H.E. and the carbon electrode versus S.H.E. obtained by measuring each with respect to the Ag/AgCl reference, and correcting for the difference between S.H.E. and Ag/AgCl (Ag/AgCl=+0.222 versus S.H.E.). The reference electrode was positioned roughly midway between the two electrodes. The cell temperature was 17°C, the electrolyte was 1M LiOH and the current used was 2 mA. It took roughly 150 hours to complete the experiment shown in figure 5.5. The voltage of the $LiMn_2O_4$ electrode agrees well with that predicted in figure 5.4. Only about 0.35 Li/Mn were incorporated into this sample before the voltage dropped to the H_2 evolution plateau, not the 0.5 Li/Mn expected from figure 5.4 based on theory. However, experiments on $LiMn_2O_4$ (Ohzuku, Kitagawa and Hirai) in non-aqueous cells show that the length of the $LiMn_2O_4$-$Li_2Mn_2O_4$ plateau is substantially less than 0.5 Li/Mn. In the reference (Ohzuku, Kitagawa and Hirai), only about 0.37 Li/Mn were obtained on this plateau, while in another reference (Thackeray, Kock, Rossouw, etc.), 0.4 Li/Mn were obtained . Our result in the aqueous cell agrees well with those in non-aqueous cells as we discuss further below. There is substantial overvoltage associated with the O_2 generation at the carbon.

Hydrogen insertion within electrolytic manganese dioxide occurs in alkaline Zn/MnO_2 cells. These cells use concentrated aqueous KOH solution as electrolytes. Since the electrolyte in those cells contains very few free H^+ and still H intercalation occurs, we were concerned that H intercalation could

be occurring simultaneously with, or instead of, Li intercalation in the experiment described by figure 5.5. To check this we made an identical cell but used 1 *M* KOH as electrolyte instead of 1 *M* LiOH. Figure 5.6 shows the voltage of the $LiMn_2O_4$ electrode plotted versus S.H.E. for the cell with KOH electrolyte. For comparison, the data from figure 5.5b measured in LiOH electrolyte is also given in figure 5.6. Also shown is the voltage versus charge profile for a nonaqueous Li/$LiMn_2O_4$ cell using 1 *M* $LiPF_6$/PC/EC electrolyte. The measured voltage of the nonaqueous cell was adjusted by -3.04 V to refer it to S.H.E. The data for the two cells with 1 *M* Li^+ in the electrolyte are in striking agreement, even though one was measured in aqueous electrolyte and one in non-aqueous electrolyte. The results using KOH are markedly different and the reaction begins at lower potential than when Li^+ is present. We take this as proof that H intercalation is not occurring in the first plateau shown in figure 5.5.

Figure 5.7a shows the x-ray diffraction pattern of the $LiMn_2O_4$ starting material which indicates a well crystallized single phase material. Figure 5.7b shows the x-ray diffraction pattern of sample *A* prepared at T=17°C with *e*/Mn=0.31. If only Li intercalation is occurring, then sample *A* is $Li_{1.62}Mn_2O_4$. The x-ray pattern shown in figure 5.7b clearly indicates that two phases coexist; one is spinel $LiMn_2O_4$, and the other is $Li_2Mn_2O_4$. These results agree those where a non-aqueous electrolyte was used to prepare $Li_{1+x}Mn_2O_4$ ($0<x<1$) (Ohzuku, Kitagawa and Hirai).

The spinel $LiMn_2O_4$ needs 0.5 Li per Mn, or e/Mn=0.5 in our aqueous setup, to be intercalated to be pure $Li_2Mn_2O_4$. Figure 5.7c shows the x-ray diffraction patterns for sample *B* prepared at T=90°C with *e*/Mn=0.75. The pattern shown in Figure 5.7c is almost pure $Li_2Mn_2O_4$. The diffraction peak

positions and the cell constants of $Li_2Mn_2O_4$ prepared in the aqueous electrolyte agree very well with those of Ohzuku et al. as we show below. The *e*/Mn ratio for sample *B* is larger than 0.5, but only 0.5 Li per Mn were actually intercalated since the final product is $Li_2Mn_2O_4$. The excess electrons were mostly used to produce H_2, in accordance with our model.

In order to obtain precise unit cell constants of $Li_2Mn_2O_4$ made in the aqueous electrolyte, we used the Rietveld profile fitting program (Li; Hill and Howard) to fit the x-ray data. Figure 5.8 shows the x-ray diffraction pattern, the calculated result from the Rietveld profile fitting and their difference for sample B. The space group used was $I4_1/amd$, the same as that of Ohzuku et al. The tetragonal cell constants we obtained are a=5.656Å and c=9.242Å, which agree well with a=5.646Å and c=9.250Å reported in an earlier work (Ohzuku, Kitagawa and Hirai). Oxygen is in the 16*h* sites with x=0.479±0.002 and z=0.252±0.002. Manganese is in 8*d* sites and lithium is in 8*c* sites (International Tables for X-ray Crystallography). During the refinement, the Mn 8d site occupation was allowed to vary and the oxygen site occupation was fixed at 1.0. The manganese occupation refined to 1.0 within error, suggesting this material has 2 oxygens per manganese as expected and that no oxygen or manganese loss has occurred in the aqueous processing. The agreement between the data and the calculation in figure 5.8 is good, the Bragg R factor (Hill and Howard) is R_B=3.85.

Chemical analysis using inductively coupled plasma mass spectrometry shows that the Li/Mn ratio in sample B is 1.0±0.1, in good agreement with the x-ray diffraction results.

We studied the stability of sample B by measuring its x-ray diffraction pattern as a function of time upon air exposure. The flat-plate x-ray sample was initially measured (one scan takes 2 hours) and then remeasured periodically over the next few days. Figure 5.9 shows the data in the region of the large peak near 18.5 degrees. Initially, only the peak from $Li_2Mn_2O_4$ (labelled 2) is observed. As time proceeds, lithium deintercalates to react with air and $LiMn_2O_4$ peaks (labelled 1) grow at the expense of the $Li_2Mn_2O_4$ peaks. Figure 5.10 shows identical behavior in a second region of the pattern. A weak Li_2CO_3 peak near 21.5°, was observed in the scan measured after 4 days of air exposure.

The results in figures 5.9 and 5.10 prove that $Li_2Mn_2O_4$ is not stable in air and lithium deintercalation slowly occurs. Furthermore, they show that the deintercalation is slow on the time scale of 30 minutes, the time needed to prepare electrodes for our non-aqueous cell tests. Although $Li_2Mn_2O_4$ is not stable in air, $Li_2Cr_{0.2}Mn_{1.8}O_4$ was recently reported to be air stable even though it has the same structure (Davidson, McMillan and Murray).

In non-aqueous electrochemical cells, $Li/Li_{2-x}Mn_2O_4$ has a voltage near 2.9 V for the phase transition from $LiMn_2O_4$ to $Li_2Mn_2O_4$ ($0<x<1$) and near 3.05 V for the transition from $Li_2Mn_2O_4$ to $LiMn_2O_4$ ($0<x<1$) (Tarascon and Guyomard, J. Electrochem. Soc.). Figure 5.11 shows the charge and discharge curves for a non aqueous Li cell using sample *A* with *e*/Mn=0.31. There are two significant plateaus for the first charge curve. The first plateau at about 3.0V corresponds to the phase transition from $Li_2Mn_2O_4$ to $LiMn_2O_4$, and the upper region corresponds to deintercalation of Li from spinel $LiMn_2O_4$ to make λ–MnO_2 (Tarascon and Guyomard). The cell shows a first recharge capacity of about 200 mAh/g between 3.0V and 4.2V, followed by a cycling

capacity near 160 mAh/g between 2.0 V and 4.2 V. The cycling capacity on the 4 V plateau is near 110 mAh/g. Sample B shows similar results. The high specific capacity for the first charge is very important for Li-ion cells since the only source of Li is from the starting cathode material. We have clearly demonstrated the preparation of $Li_2Mn_2O_4$ in aqueous solutions using the starting material $LiMn_2O_4$.

Now we describe the phenomenon when e/Mn>>0.5 for $LiMn_2O_4$. Figure 5.12 shows x-ray diffraction profiles of samples with various values of e/Mn from 0 to 1.61. The x-ray diffraction profiles suggest that the phase transitions are $LiMn_2O_4$ ----> spinel $Li_2Mn_2O_4$ -----> $Mn(OH)_2$ as described in equations (5.12) and (5.13), since their x-ray patterns are consistent with these materials, respectively. As shown in figure 5.12(e) the $Li_2Mn_2O_4$ phase still dominates over the $Mn(OH)_2$ phase even when e/Mn=1.61, which does not agree with the fact that Mn needs only 1.5 electrons to totally transfer from oxidation state 3.5 in $LiMn_2O_4$ to oxidation state 2 in $Mn(OH)_2$. That means H_2 evolution is involved as described in equation (5.14). The oxygen lattice is distorted cubic close packed for $Li_2Mn_2O_4$ and hexagonal close packed for $Mn(OH)_2$. Therefore the oxygen frame has to be rearranged in the phase transition from $Li_2Mn_2O_4$ to $Mn(OH)_2$, which is perhaps difficult at room temperature.

We also used γ-$Li_{0.36}MnO_2$ as the starting material to prepare γ–$LiMnO_2$ in aqueous solutions. We suppose that e/Mn=0.64 is needed to convert γ–$Li_{0.36}MnO_2$ to γ–$LiMnO_2$. In order to further investigate if Li or H intercalates into γ–$Li_{0.36}MnO_2$, we made two identical cells but with 2.5 M KOH and 2.5 M LiOH aqueous electrolytes, respectively. Figure 5.13 shows the voltage profiles in aqueous cells with 2.5M KOH and with 2.5M LiOH.

Comparing the results from 2.5 M KOH and 2.5 M LiOH aqueous solutions, one finds that the two curves are markedly different and the voltage using LiOH solutions is higher than that using solutions KOH for e/Mn<0.75. When e/Mn>1.35, both voltages from KOH and LiOH reach the lower plateau and their difference is much smaller than that for e/Mn<0.60. This means that H_2 evolution probably occurs in both cells at e/Mn>1.35 and the difference of voltage at e/Mn>1.35 also indicates the experimental error. The experimental of the voltage measurement is much less than the difference between that for Li^+ and H^+ intercalation (for e/Mn<0.6) as shown in figure 5.13. Therefore, we believe that Li^+ dominates over H^+ during the intercalation into γ–$Li_{0.36}MnO_2$ for e/Mn<0.60, in 2.5 M LiOH solutions.

Furthermore, the voltage difference between the Li^+ ion and the H^+ ion intercalation for e/Mn<0.6 may be larger than those shown in figure 5.13. We give the following reasons. Because the Li intercalation voltage of λ–MnO_2 can be above the voltage of O_2 evolution, λ–MnO_2 can react with LiOH aqueous solutions as described in equation (5.15). Since the Li intercalation potential of γ–$Li_{0.36}MnO_2$ is very close to the O_2 evolution potential in highly concentrated basic solutions, γ–$Li_{0.36}MnO_2$ may react with LiOH solution until Li intercalation occurs below the voltage of O_2 evolution . Therefore, it is possible that some Li has intercalated into γ–$Li_{0.36}MnO_2$ at e/Mn=0 in 2.5 M LiOH aqueous solutions before the current is passed while there are no reactions between KOH and γ–$Li_{0.36}MnO_2$ without passing current (It has been demonstrated that K atoms do not fit within γ–type MnO_2 (Kao, Weibel and Root). The actual potential difference between Li^+ ion and H^+ ion intercalation into γ–$Li_{0.36}MnO_2$ for e/Mn<0.6 may therefore be larger than as shown in figure 5.13.

Figure 5.14 shows the x-ray diffraction patterns of γ–MnO_2 in (a), γ–$Li_{0.36}MnO_2$ in (b), and sample C in (c). Sample C was prepared with a starting material of γ–$Li_{0.36}MnO_2$ followed by reduction with e/Mn=0.5 in a 2.5 M LiOH aqueous solution. All the three materials shown in figure 5.14 have similar structures and slightly different lattice constants. The lattice constants for γ–MnO_2 are approximately a=4.40±0.02 Å, b=9.55±0.02 Å, and c=2.81±0.02 Å; The lattice constants for γ–$Li_{0.36}MnO_2$ are a=4.89±0.02 Å, b=9.88±0.02 Å, and c=2.82±0.02 Å. Finally, the lattice constants for sample A are a=4.96±0.02 Å, b=10.14±0.02 Å, and c=2.77±0.02 Å. This is consistent with lithium intercalation because similar lattice constants for R-MnO_2 prepared by other methods was reported (Thackeray, Rossouw, Gummow et al.).

After we further treated the γ–$Li_{0.36}MnO_2$ materials with a larger value of e/Mn in LiOH solution, which is beyond the first plateau (e/Mn>0.6) shown in figure 5.13, the structure of the products changed from orthorhombic to hexagonal. Figure 5.15 shows the x-ray diffraction pattern of the product obtained from using the starting material γ–$Li_{0.36}MnO_2$ followed by reduction with e/Mn=0.98 in 2.5 M LiOH. The products can be described by space group P -3M1 with Mn atoms in 1a sites and O atoms in 2d sites, and with a hexagonal cell of lattice constants a=3.32Å and c=4.74Å, which is close to the values a=3.34Å and c=4.68Å for $Mn(OH)_2$ (Wyckoff), and far from the values a=3.195Å and c=5.303Å in Li_2MnO_2 (David, Goodenough, Thackeray and Thomas).

In order to further investigate if H or Li is in the $Mn(OH)_2$ type materials, we used neutron diffraction to investigate the sample prepared by reducing γ–$Li_{0.36}MnO_2$ with e/Mn=0.98. We used D_2O, teflon binder $[(-CF_2-)_n]$ and $LiOH{\cdot}H_2O$ in order to minimize the H content in the sample and therefore

the background count rate of the neutron diffraction profile. Figure 5.16 shows the experimental neutron diffraction profile and the calculated profile from the Rietveld fitting program. The profiles shown figure 5.16 (a), (b) and (c) are calculated by assuming $Mn(OD)_2$, $Mn(OLi_xD_{1-x})_2$ and $Mn(OLi)_2$ respectively. The best fit is obtained in figure 5.16 (b) with x=0.22. Although we can not confirm the Li content because the statistics in the data are not accurate enough, we can conclude that the sample is not $Mn(OLi)_2$ because of the poor fit for $Mn(OLi)_2$ shown in figure 5.16 (c). We exclude two regions during the fit, from 30.50° to 40.00° and from 57.00° to 67.00°, because some strong peaks from an unknown impurity phase appear in those regions. This impurity phase did not appear in a similar sample measured by x-ray diffraction (figure 5.15). The materials can be written as $Mn(OLi_xD_{1-x})_2$, with the D content (or 1-x) in the range between 0.5 and 1.0, and the Li content (or x) in the range between 0.5 and 0.0. D. Li was assumed to share the same sites randomly with D at 2d sites in space group P -3M1. We can conclude that substantial D is in this material, $Mn(OLi_xD_{1-x})_2$, and that Li intercalation does not occur at the lower voltage plateau. Instead, H (D) intercalation and ion exchange between Li^+ and H^+ (D^+) occurs.

5.4 Summary

We have shown that $Li_2Mn_2O_4$ can be prepared from $LiMn_2O_4$ in aqueous LiOH electrolyte. The $Li_2Mn_2O_4$ prepared in this way may be useful for Li-ion cell cathodes. The voltage of the aqueous cell is in good agreement with our model predictions. We showed that lithium transition metal oxides with $3.5V \geq V(x) \geq 2.3V$ should be stable in 1M LiOH aqueous solutions. These findings suggest that many more lithium transition metal oxides with high lithium content (e. g. $Li_xV_2O_5$) could be prepared by this method as cathodes for Li-ion cells. Further work is also needed to understand the $Li_2Mn_2O_4$ ---> $Mn(OH)_2$ reaction and the γ-$Li_{0.36}MnO_2$ ---> $Mn(OH)_2$ reaction.

One especially attractive option could involve the use of electrochemical manganese dioxide (EMD). In the manufacture of EMD, deposits of MnO_2 are plated on titanium electrodes. These electrodes could be lifted from the acid bath, rinsed, possibly heat treated, dipped into LiOH solution and filled with lithium by our method. It has been shown [19] that lithiated EMD is an excellent 3 V cathode for Li batteries. If the EMD could be prepared fully lithiated by our method, then it could be used for low cost lithium-ion cells.

In this chapter we also clearly showed that the potentials of Li during intercalation from aqueous solution are the same as that from non-aqueous solution. This implies that rechargeable lithium ion cells can be made with aqueous electrolytes by using two appropriate intercalation compounds. The voltage of this cell will depend on the binding energy of Li in the compounds used as the cathode and the anode. In the next chapter, a new technology of lithium-ion cells is demonstrated based on the understanding of lithium intercalation from aqueous electrolytes.

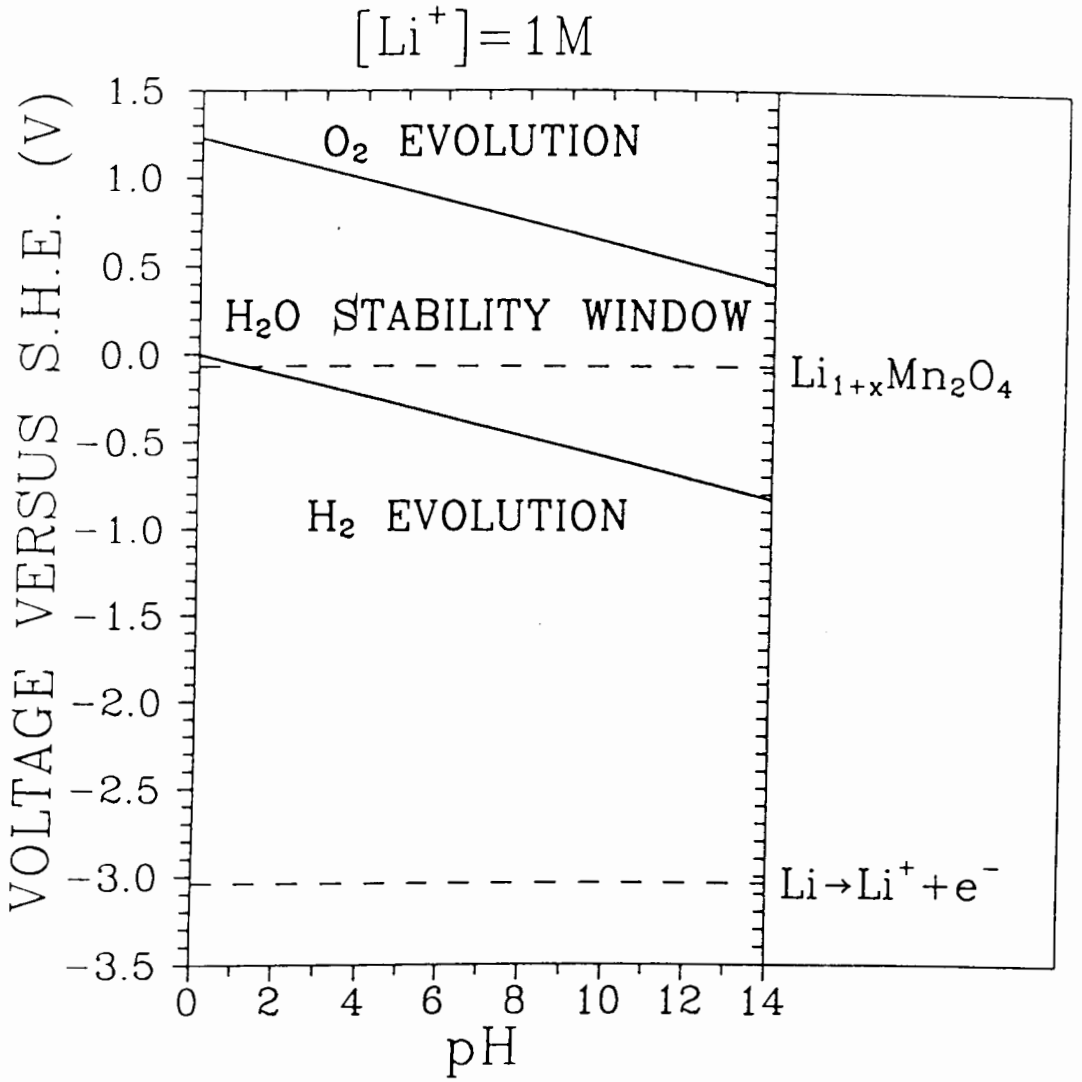

Figure 5.1. The H_2O stability window in solutions where $[Li^+]$=1M after Bockris and Reddy. Since $[Li^+]$=1M, the potentials of Li metal and $Li_{1+x}Mn_2O_4$ are easily located with respect to S. H. E. Li deintercalation coupled with H_2 evolution will begin below pH=2.

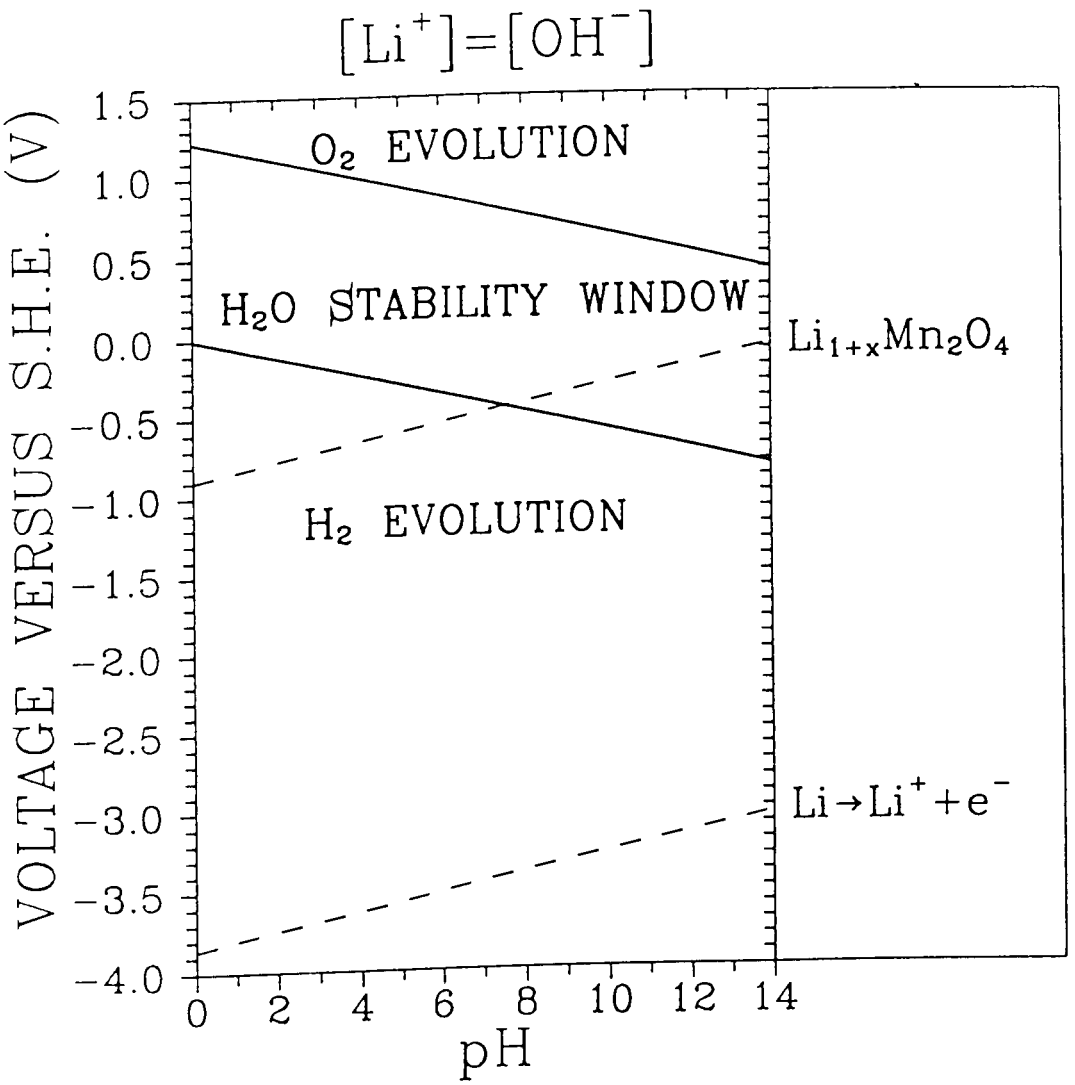

Figure 5.2. The H_2O stability window in solutions where $[Li^+]=[OH^-]$. Since $[Li^+]=[OH^-]$, the potentials of Li metal and $Li_{1+x}Mn_2O_4$ vary with respect to S. H. E. Li deintercalation from $Li_{1+x}Mn_2O_4$ coupled with H_2 evolution will begin below pH=8.

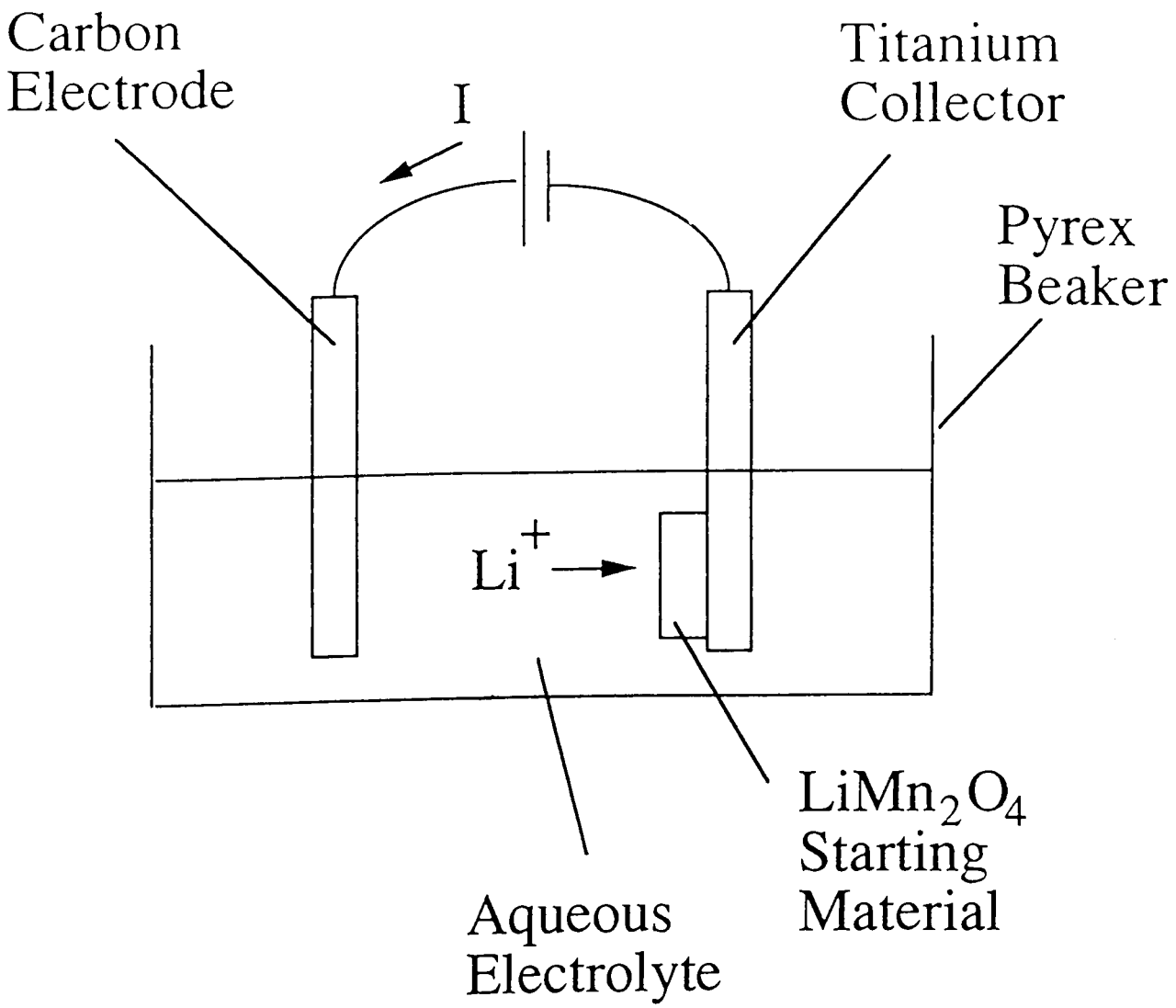

Figure 5.3. A sketch of the aqueous electrochemical cell and the current direction. A typical aqueous electrolyte is 1 M LiOH in H_2O.

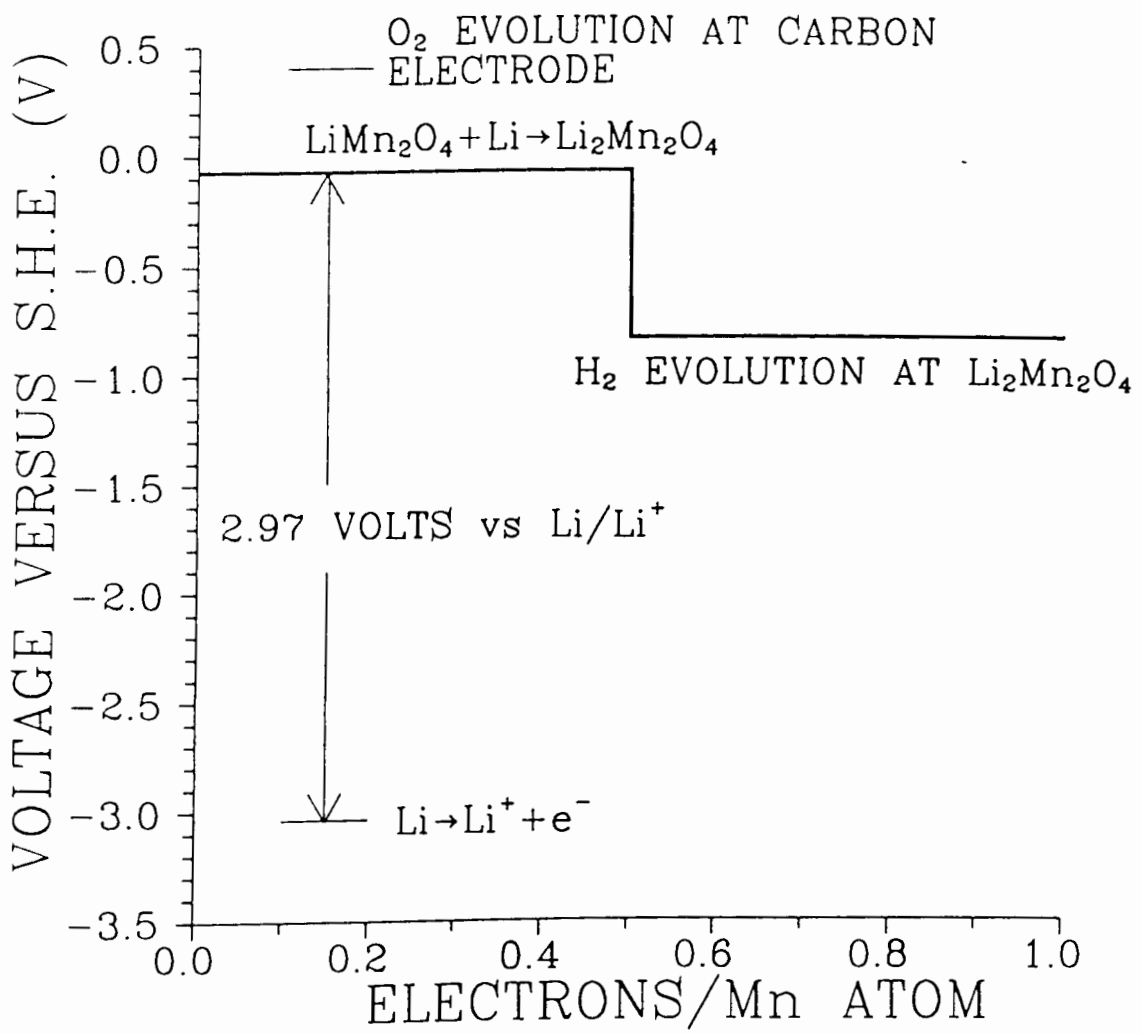

Figure 5.4. The predicted voltage of the $LiMn_2O_4$ electrode (heavy line) versus the standard hydrogen electrode as electrons and Li^+ are transferred to it. Beyond 0.5 e/Mn, H_2 evolution begins to occur at the $Li_2Mn_2O_4$ electrode. The potential for O_2 evolution at the carbon electrode is also indicated.

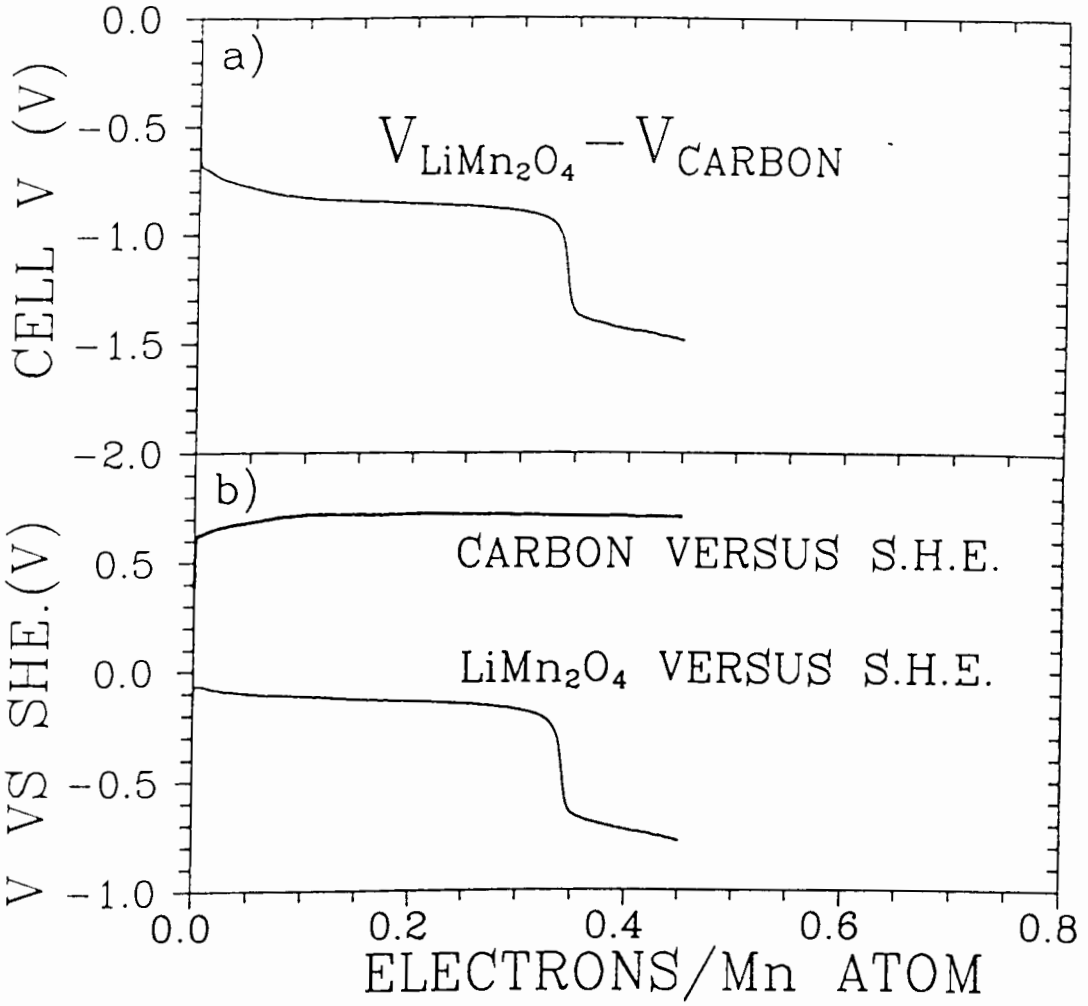

Figure 5.5. Experimental results for the aqueous carbon/$LiMn_2O_4$ cell using a 1M LiOH solution. a) The difference in voltage between the $LiMn_2O_4$ electrode and the carbon electrode. b) The potentials of the carbon electrode and the $LiMn_2O_4$ electrode versus the standard hydrogen electrode, for comparison with figure 5.4.

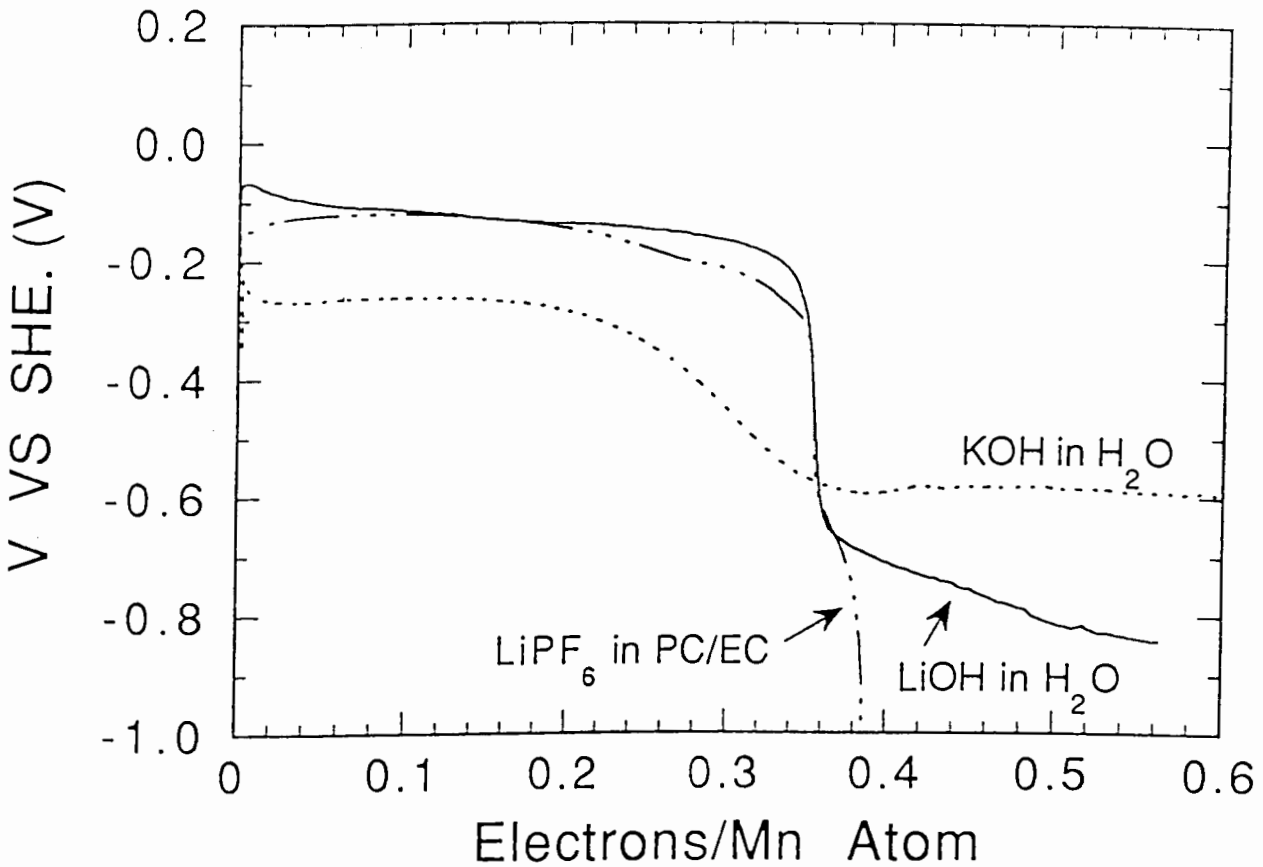

Figure 5.6. Experimental results for carbon/$LiMn_2O_4$ cells using a 1 M LiOH aqueous electrolyte (solid) and 1 M KOH aquoues electrolyte (dash). Also shown for comparison is the voltage versus charge for a Li/$LiMn_2O_4$ cell using a non aqueous electrolyte (dot-dash) of 1 M $LiPF_6$ in PC/EC. The measured data for the latter cell was corrected by adding -3.04 V to convert to potential versus S. H. E.

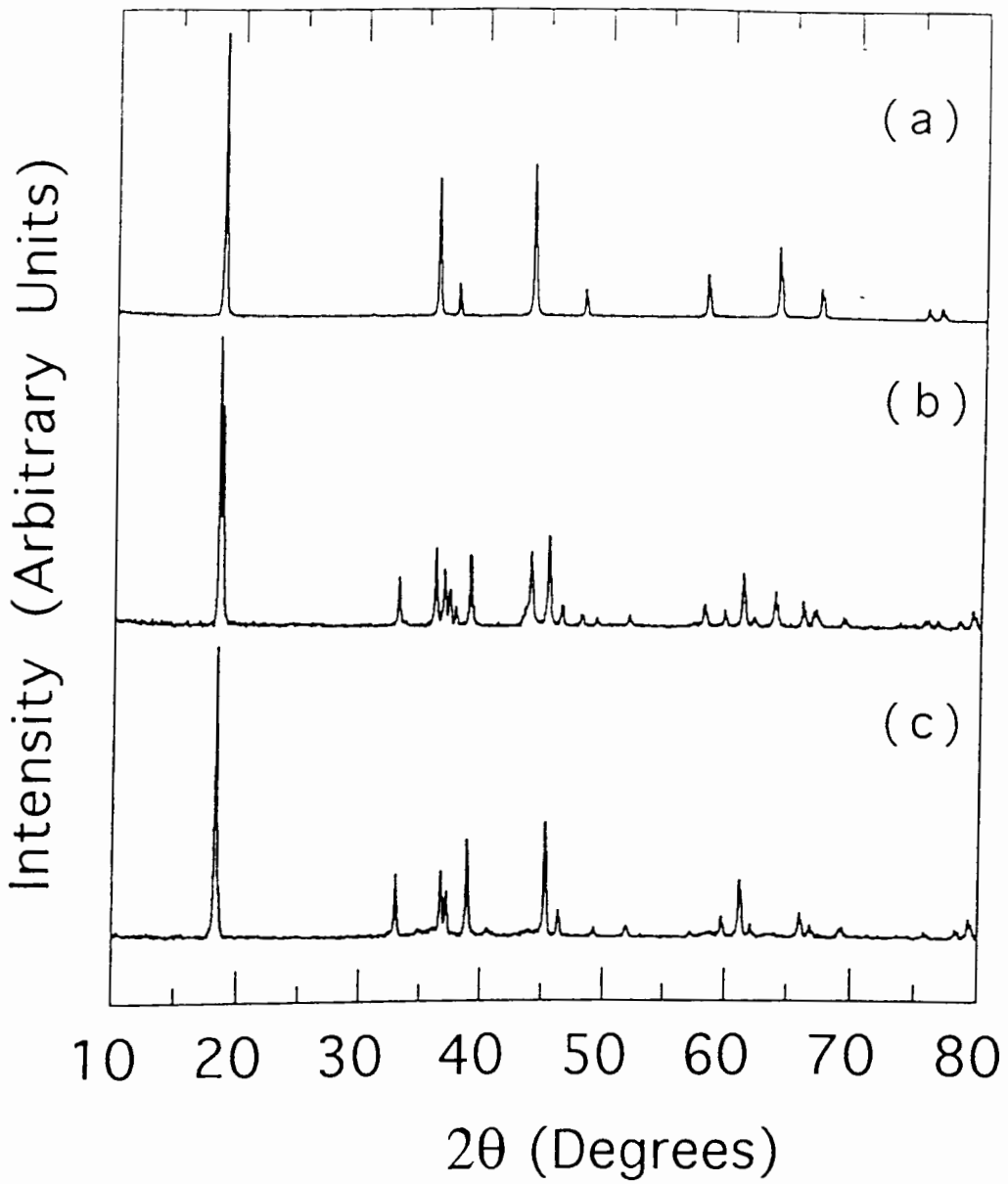

Figure 5.7. The x-ray diffraction profiles of the $LiMn_2O_4$ starting material (a), Sample A (0.31 *e*/Mn) (b) and Sample B (0.75 *e*/Mn) (c). Sample A is a mixture of $LiMn_2O_4$ and $Li_2Mn_2O_4$ and sample B is predominantly pure $Li_2Mn_2O_4$.

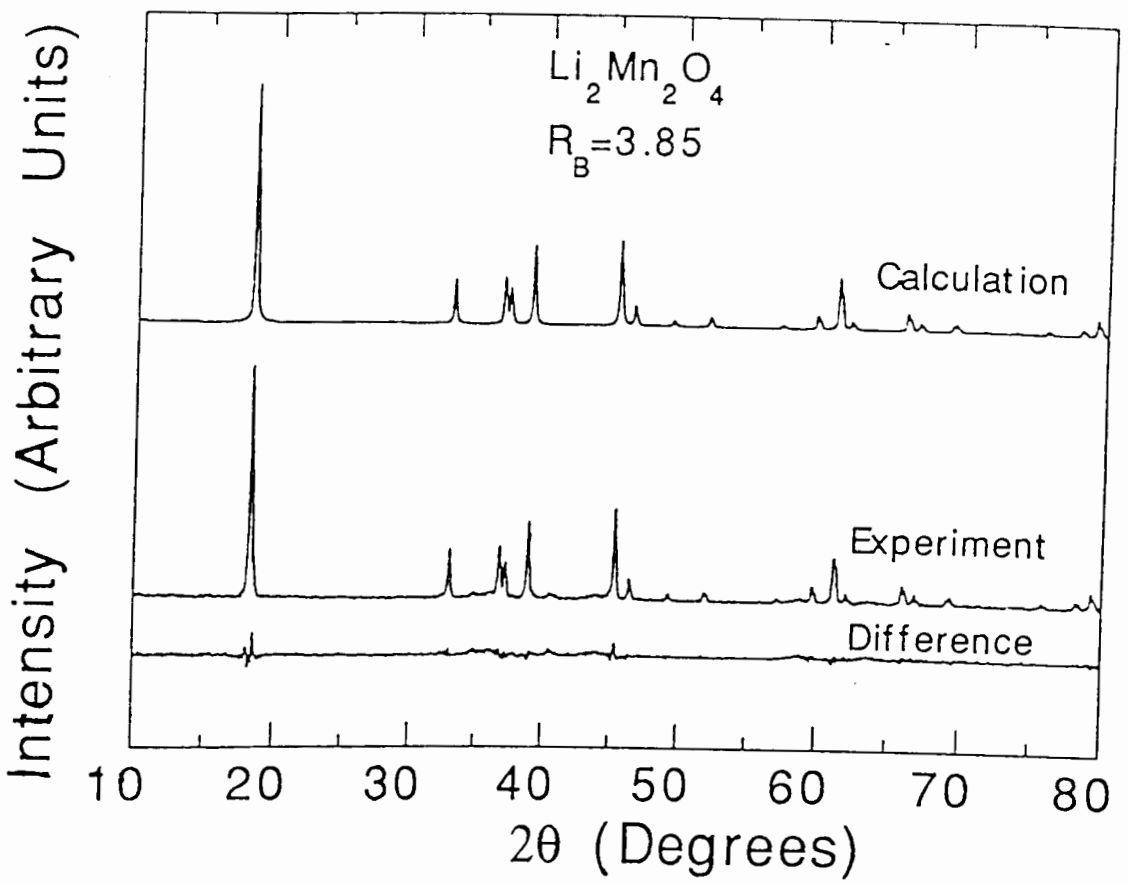

Figure 5.8. Rietveld profile refinement for Sample B. The calculated and measured patterns are shown, as is the difference between them. The Bragg R factor was 3.85.

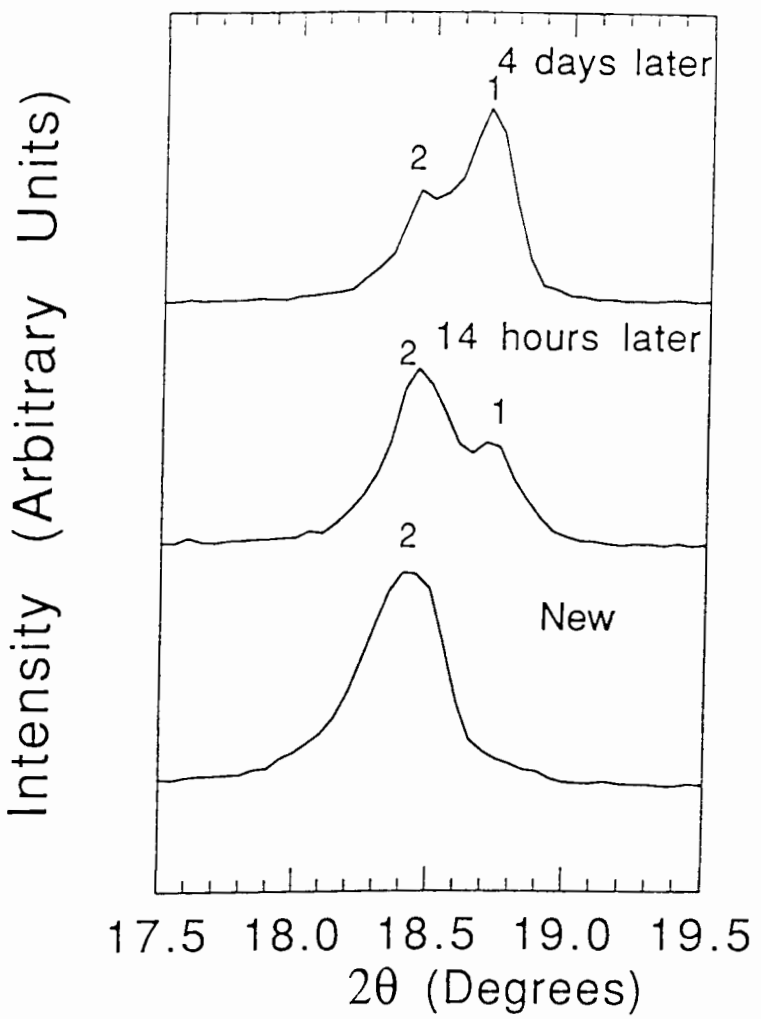

Figure 5.9. X-ray diffraction profiles of Sample B in the range from 17.5° to 19.5° showing the structure changes as a function of time upon air exposure. Peaks labelled 1 are from $LiMn_2O_4$ and those labelled 2 are from $Li_2Mn_2O_4$.

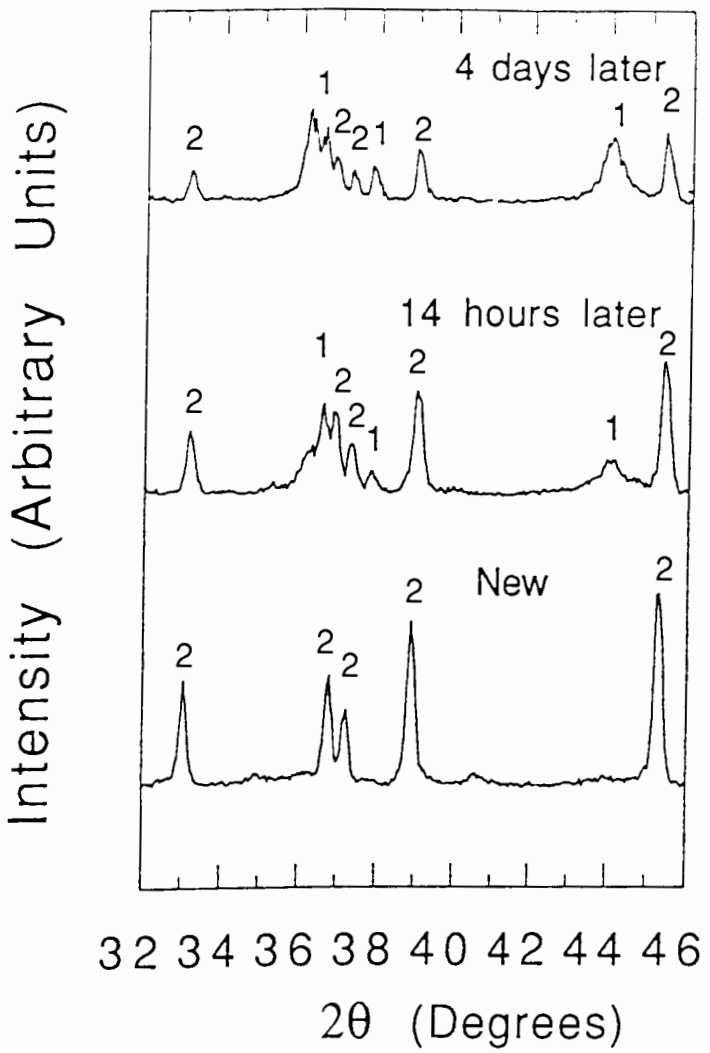

Figure 5.10. X-ray diffraction profiles of Sample B in the range from 32° to 46° showing the structure changes as a function of time upon air exposure. Peaks labelled 1 are from $LiMn_2O_4$ and those labelled 2 are from $Li_2Mn_2O_4$.

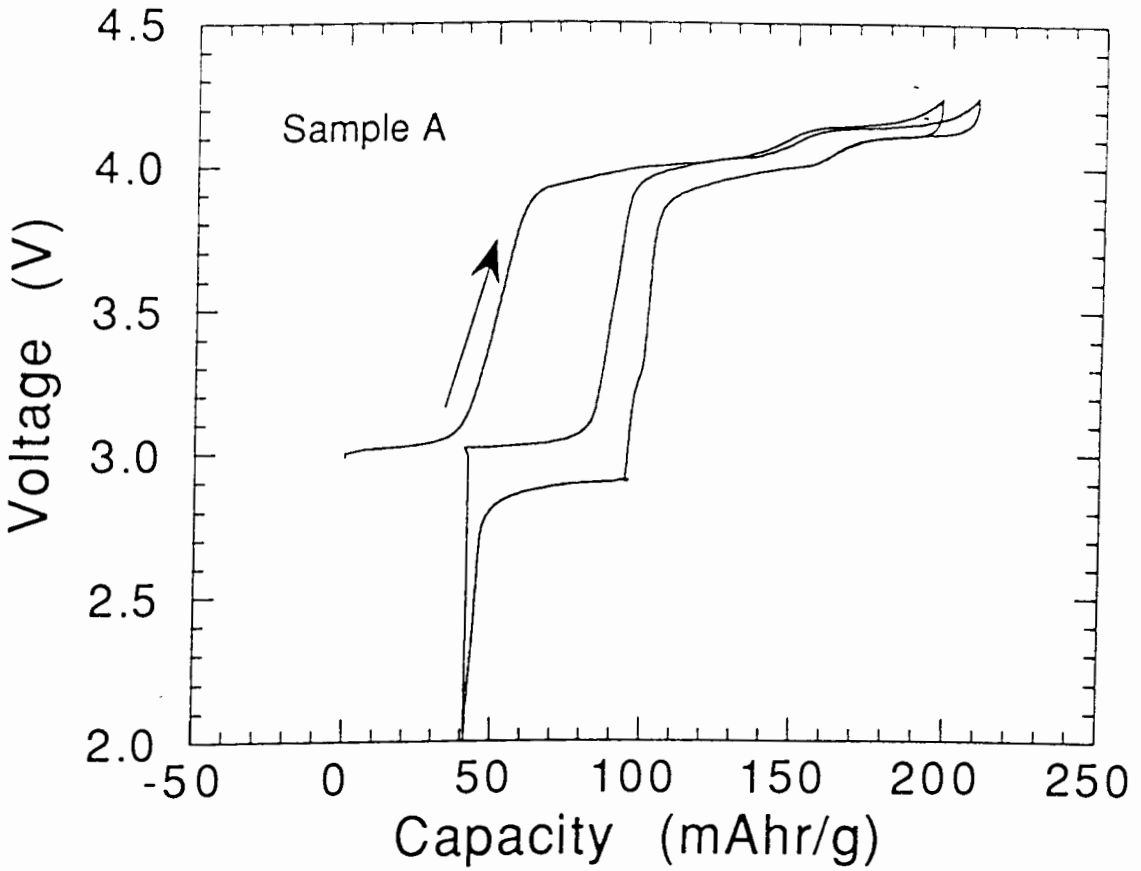

Figure 5.11. The voltage of a non-aqueous Li cell with Li metal made using Sample A as the cathode electrode. The cell current was 2.8 mA/g and the temperature was 30°C.

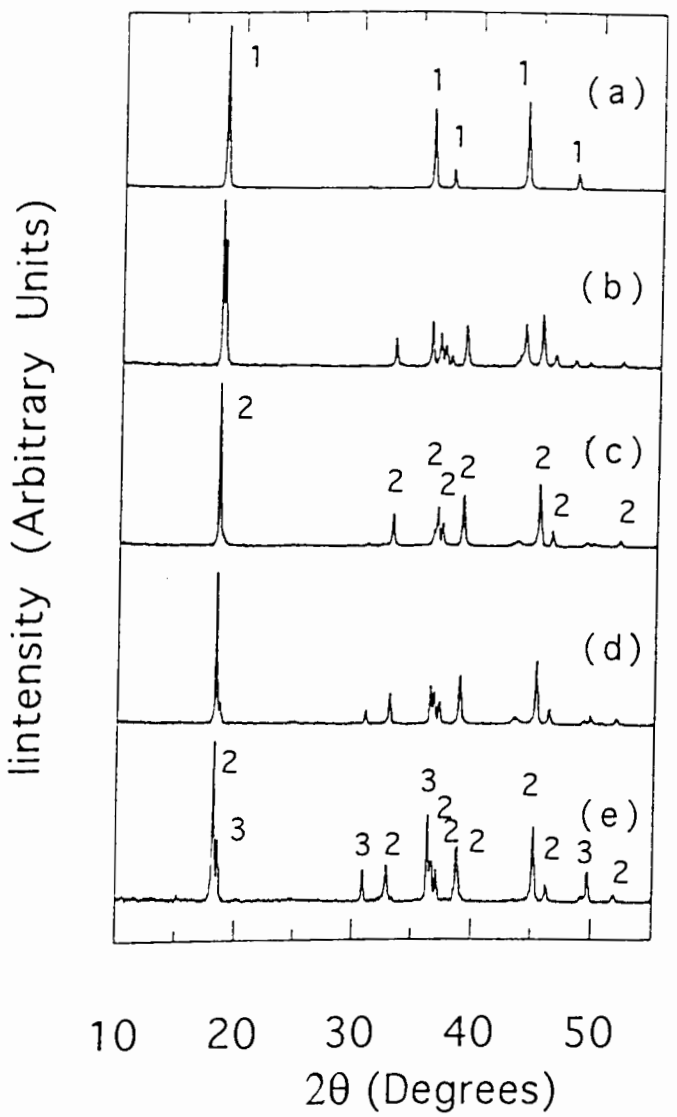

Figure 5.12. The x-ray diffraction profiles showing the phase trasitions from spinel $LiMn_2O_4$ ---->spinel $Li_2Mn_2O_4$ ----> $Mn(OH)_2$ in the aqueous cell. The numbers 1, 2 and 3 correspond to the Bragg peaks of $LiMn_2O_4$, $Li_2Mn_2O_4$ and $Mn(OH)_2$ respectively. a) The x-ray diffraction profile of spinel $LiMn_2O_4$. b) The x-ray diffraction profile when e/Mn=0.31 showing both $LiMn_2O_4$ and $Li_2Mn_2O_4$. c) e/Mn=0.63. d). e/Mn=0.75. e) e/Mn=1.61.

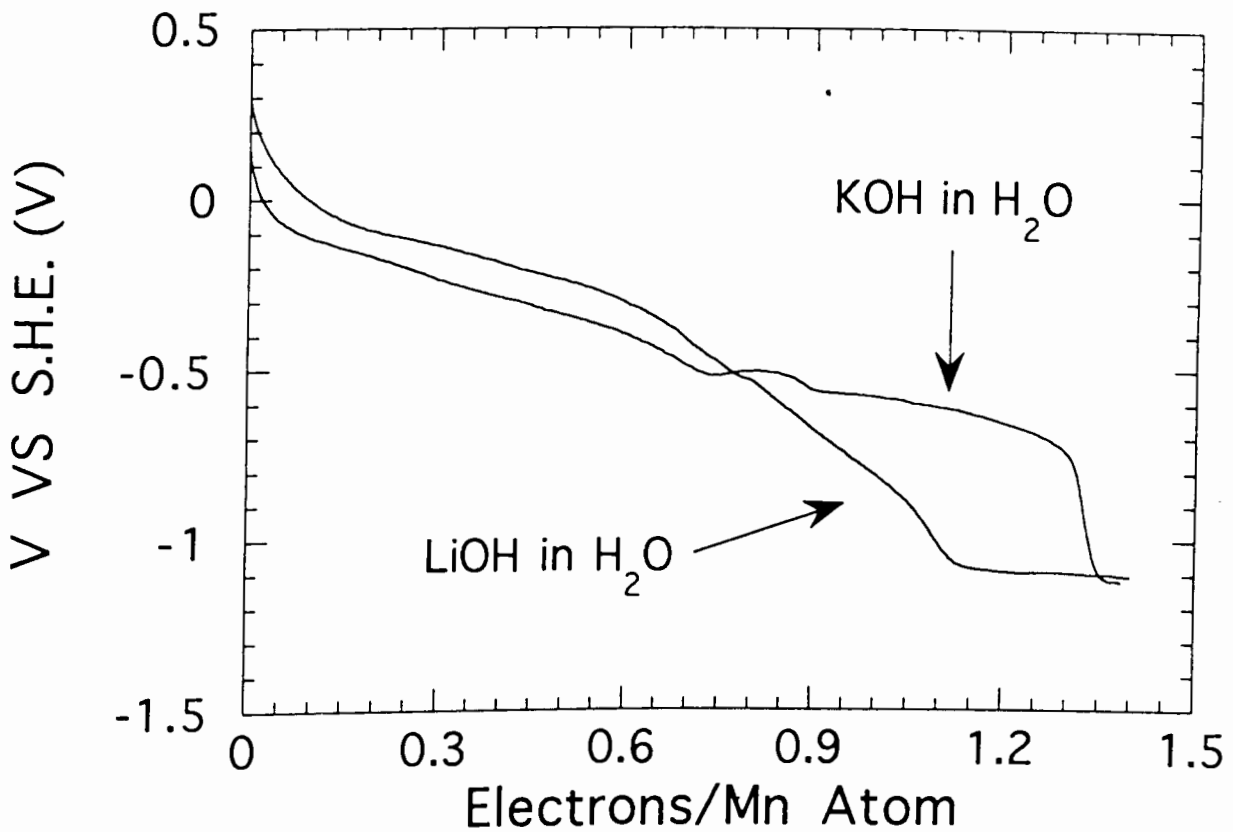

Figure 5.13. The voltage versus S. H. E. of two identical cells using γ–$Li_{0.36}MnO_2$ as the starting material but with 2.5 M KOH and 2.5 M LiOH aquoues electrolytes, respectively.

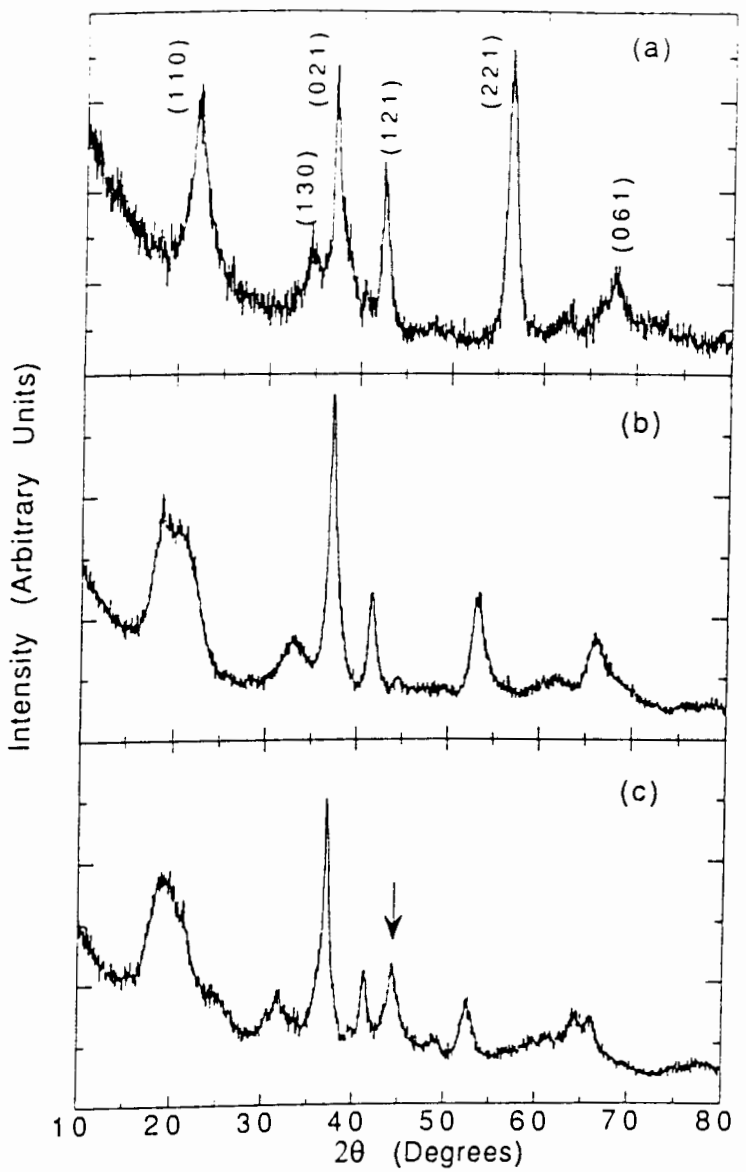

Figure 5.14. The x-ray diffraction patterns of (a) γ–MnO_2, (b) γ–$Li_{0.36}MnO_2$ and (c) sample C with a starting material of γ–$Li_{0.36}MnO_2$ followed by reduction with e/Mn=0.5 in a 2.5 LiOH aqueous solution.

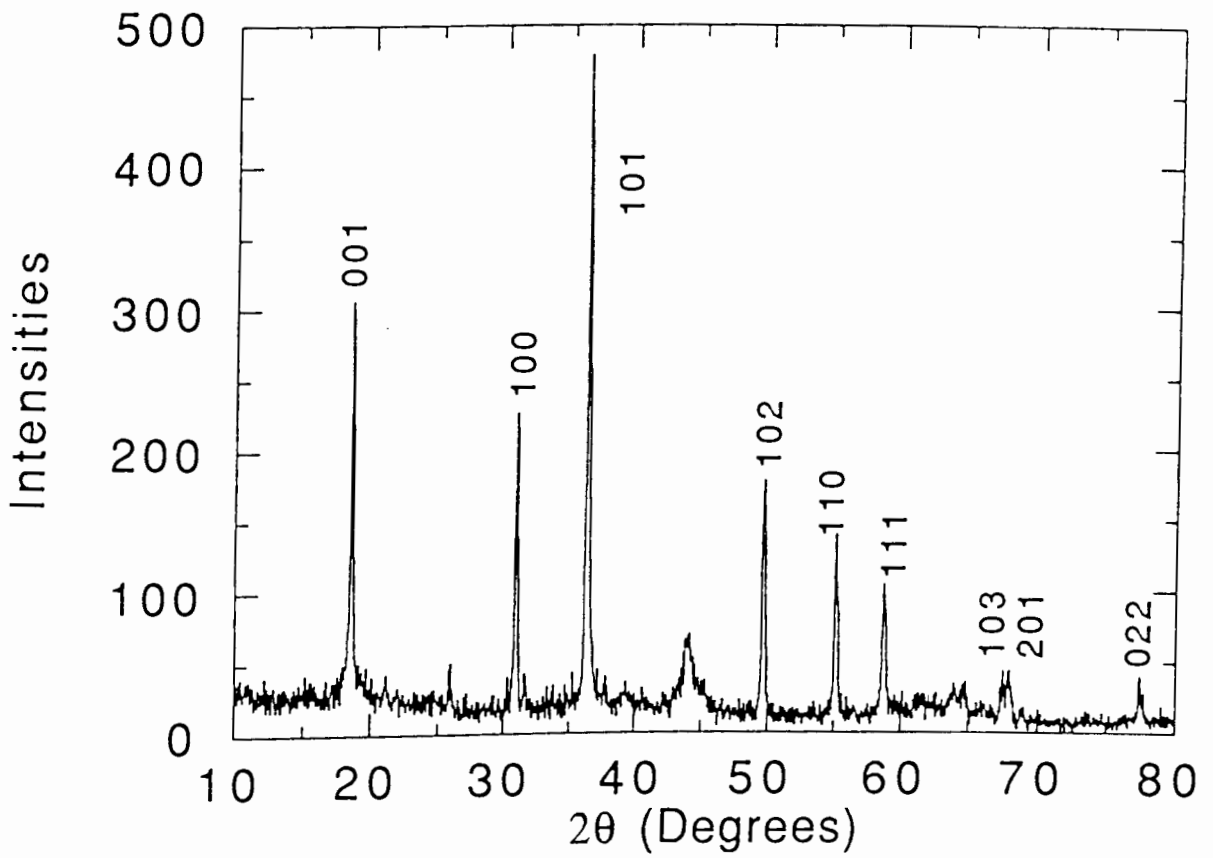

Figure 5.15. The x-ray diffraction profile of the product obtained from using the starting material γ–$Li_{0.36}MnO_2$ followed by reduction with e/Mn=0.98 in a 2.5 M LiOH aqueous solution.

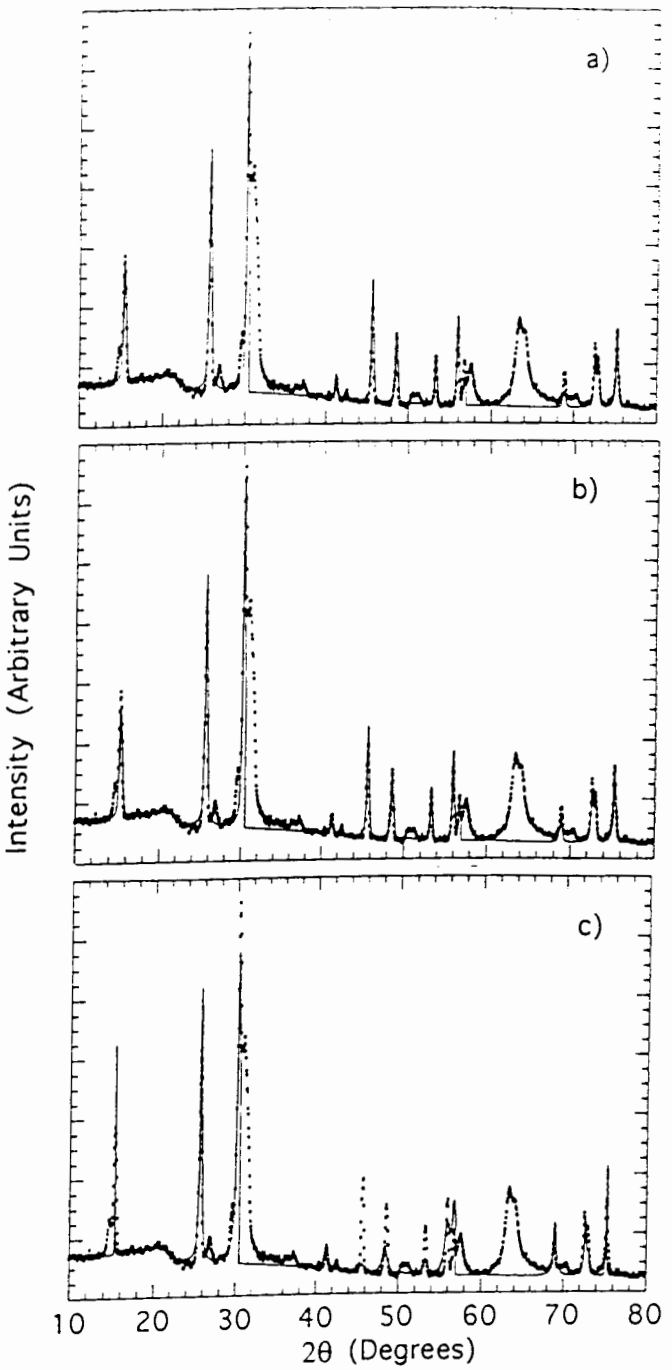

Figure 5.16. The neutron diffraction profile and the calculated results from the Rietveld fitting program. The data points are the experimental results. The lines in (a), (b) and (c) are the calculated results assuming $Mn(OD)_2$, $Mn(OLi_xD_{1-x})_2$ and $Mn(OLi)_2$ respectively.

Chapter 6. Rechargeable Lithium Batteries with Aqueous Electrolytes

6.1 Background

There are more and more people concerned about urban air quality. Recently, U. S. federal and state governments have passed legislation aimed at reducing automobile pollution. California has passed laws that require 2% of new cars sold in 1998 be emission-free, and 10 % by the year 2003. 12 eastern U. S. states are planning similar laws. Some people here in B. C. want to propose similar action. One solution for emission-free vehicles is the electric vehicle. The availability of an efficient and low cost battery is the key to develop practical electric vehicles. The Nickel-Metal Hydride Battery is currently probably the best candidate for practical electric vehicles (Ovshinsky, Fetcenko and Ross). However, some industry experts contend that the Nickel-Metal hydride battery technology is too expensive and is not environmentally acceptable for electric vehicle applications.

Rechargeable lithium batteries with non-aqueous electrolytes can be used for powering consumer electronics. However, it is more difficult to make a large safe lithium rechargeable battery a with non-aqueous electrolyte. Furthermore, non-aqueous electrolytes usually have ion conductivity two orders of magnitude lower than aqueous electrolytes, so thin electrodes must be used in these cells in order to increase power. The salts used in these cells like $LiPF_6$, $LiBF_4$ are very expensive. The separators are also very expensive. Therefore, rechargeable lithium batteries with non-aqueous electrolytes may not be suited for electric vehicle application, which require safe, inexpensive, high power, rechargeable batteries.

Here, we show that water-based electrolytes can be used in lithium-ion cells (Li, Dahn and Wainwright). When aqueous electrolytes are used, high ion conductivities are obtained and thick electrodes can be used. Cheap salts like $LiNO_3$ can be used and inexpensive separators can replace the expensive separators. Therefore this fundamentally safe and inexpensive technology provides a new option for electric vehicle applications.

In chapter 5, we showed that lithium can be intercalated from aqueous solution. The key to this discovery is to select appropriate materials which are stable in aqueous solution with dissolved Li^+, and to adjust the stability window of aqueous solution by changing its pH's value. As shown in figure 1.3, many lithium transition metal oxides are intercalation compounds. Some of the lithium binding energies in lithium intercalation compounds are within the stability window of water. Therefore these compounds can be selected as the cathode and the anode materials for rechargeable lithium batteries with aqueous electrolytes.

6.2 Aqueous Li-ion Cells

When a lithium intercalation compound is put in water, one must consider whether the intercalated lithium reacts with water as described in equation (5.2), that is

$$Li(intercalated) + H_2O <---> Li^+ + OH^- + (1/2)H_2 \qquad (6.1)$$

The chemical potential of Li^+ in solution increases with concentration and tends to drive equation (6.1) to the left. On the other hand, the concentration of H^+ or OH^- can adjust the stability window of H_2O. Therefore we must also consider the potentials for oxygen and hydrogen evolution which can occur in aqueous electrolytes. Figure 6.1 shows the standard electrode potentials for these reactions occurring in acidic or basic aqueous electrolytes which also incorporate 1M Li^+ ion concentration. Figure 6.1 also shows the standard electrode potential for the reaction:

$$Li <---> Li^+ + e^- \qquad (6.2)$$

Since figure 1.3 measures the chemical potentials of lithium intercalation compounds relative to reaction (6.2), we can locate electrode materials on figure 6.1, as we have done for the reactions

$$LiMn_2O_4 <----> Li_{1-x}Mn_2O_4 + xLi^+ + x\,e^- \qquad (6.3)$$

and

$$VO_2(B) + xLi^+ xe^- <----> Li_xVO_2(B) \qquad (6.4)$$

In an appropriately chosen electrolyte, each of reactions (6.3) and (6.4) should be viable without excessive O_2 or H_2 production occurring simultaneously. A cell based on reactions (6.3) and (6.4) will have a terminal voltage near 1.5 volts. As shown in figure 5.1, the stability window of H_2O is 1.2V which is the working voltage of Ni-MH cells. Here our cells work over this window without the direct H_2 or O_2 evolution from H_2O as shown in figure 6.1. Since the concentration of H^+ and OH^- are much smaller than that of Li^+ in the aqueous solution we used, Li^+ carries most of the ionic current in the cells. Therefore H_2 and O_2 evolution reactions are minimized.

We synthesized $LiMn_2O_4$ according to the methods of Ohzuku, Kitagawa and Hirai, and synthesized VO_2(B) according to the methods of Dahn, Buuren and Sacken. Tablet electrodes of dimension 8 mm diameter and total mass 0.10 g were prepared from each material. Carbon Black (10 % by weigh) and EPDM (ethylene propylene diene monomer) binder (3 % by weight) were added to the tablet mix to provide good electrical conductivity and good mechanical toughness. The mix was then pressed in 0.10 g allotments in a cylindrical die to the desired thickness (1.0 mm).

Coin-type test cells using 1225 (12mm diameter, 2.5 mm thickness) hardware were then prepared. First, the electrodes were thoroughly wetted with an aqueous solution that was 5.0 M in $LiNO_3$ and about 0.001 M in LiOH. A microporous polypropylene separator (Celgard 3500) which incorporates a wetting agent was used to separate the electrodes as they were tightly crimped in the cell case. Figure 6.2 shows a schematic of the finished cell. Since $[OH^-]$=0.001 M in this cell, we expect the potentials for H_2 and O_2 evolution to shift up by about 0.175 V compared to their positions in 1 M OH^- as shown on the right of figure 6.1.

The cell was then charged using a current of 1 mA. During the charge, lithium is extracted from $LiMn_2O_4$, making $Li_{1-x}Mn_2O_4$, and intercalated into $VO_2(B)$ making $Li_xVO_2(B)$. Figure 6.3 shows the voltage profile during this charging and during the next few charge-discharge cycles. The cell shows excellent reversibility, an average voltage near 1.5 volts and a capacity of 10 mAh.

Using the weight of the electrodes, the cell voltage and the cell capacity, it is possible to calculate the energy density of the cell (not including the electrolyte or cell case weight). This cell achieves 75 Wh/kg. Typically, the active electrode weights are about 50 % of the total weight of practical cells, based on the Sony Li-ion product as an example. Thus practical energy densities near 40 Wh/kg can be expected for this chemistry, when incorporated in larger size cells. Furthermore, we point out that the theoretical energy density for this cell is 112 Wh/kg assuming 0.5 Li per transition metal can be cycled in each electrode and that the average cell voltage is 1.5 V. This would give about 55 Wh/kg in a practical cell which is competitive with both Pb-acid (about 30 Wh/kg) and NiCd (about 50 Wh/kg) technologies.

The $LiMn_2O_4/VO_2(B)$ couple by no means represents the optimum electrode pair for the aqueous Li-ion cell. Many types of lithium manganese oxides are known to intercalate lithium in the right chemical potential range for this type of cell (Ohzuku, Ueda and Hirai). One interesting approach to an extremely low cost system would be to use $LiMn_2O_4$ for both electrodes. Since Li can be extracted from $LiMn_2O_4$ (to form $Li_{1-x}Mn_2O_4$) at 4V versus Li and added to $LiMn_2O_4$ (to form $Li_{1+x}Mn_2O_4$) at about 3V versus Li, a 1V cell would result. Manganese and its oxides are cheap, plentiful and less-toxic

than Ni and Co oxides, so a $Li_{1+x}Mn_2O_4/Li_{1-x}Mn_2O_4$ cell could have an enormous potential market.

As an example using Mn compounds for both the electrodes, figure 6.4 shows the voltage profile during first a few charge-discharge cycles of a cell using $LiMn_2O_4$ as positive electrode, γ–$Li_{0.36}Mn_2O_4$ as negative electrode and 5 M $LiNO_3$ aqueous electrolyte. The average voltage of this cell is 0.8V and the discharge time is about 10 hours. Using the weight of the electrodes, the cell voltage and the cell capacity, we obtain a cell specific energy of 40 Wh/kg. Although it achieves smaller energy density than the $LiMn_2O_4/VO_2(B)$ cell, the $LiMn_2O_4/\gamma$–$Li_{0.36}Mn_2O_4$ cell gives an example using aqueous electrolyte and Mn compounds as electrodes.

Other cell data obtained using various salts and electrode couples are listed in table 6.1. All of them show rechargeable capacity but most of them have a short cycle life. We do not yet know the reason for the capacity loss with cycle number. The cell shown in figure 6.3 has a good cycling behavior up to about 20 cycles and then its capacity begins to fade. For the cell using the $LiMn_2O_4/VO_2(B)$ electrode couple, the capacity fade may be due to the decomposition of H_2O since the cell working voltage is larger than the stability window of H_2O (However, we point out that the terminal voltage of the Pb-acid cell, 2.04 V, is much larger than the stability window of water). Another possible reason is that the materials could be dissolving in H_2O. For example the V ion may be dissolving since a color change in electrolyte is observed after some cycles. Many electrode materials like $VO_2(B)$ also have neighboring metastable phases and are subject to phase transitions to them. Therefore, structural changes of the electrode materials may be another reason for the capacity loss with cycles. Self discharge also appears in these cells. The reason may be due to O_2 evolution.

Again, one may be concerned that H intercalation is involved during the charge and discharge reactions in these cells, like H intercalation in alkaline cells. Here we give an argument and some results to show that it is impossible that H intercalation is the major reaction in $LiMn_2O_4/VO_2(B)$, or $LiMn_2O_4/\gamma$–$Li_{0.36}MnO_2$ cells. In the coin cells, we usually have about 0.1 g electrolyte. Imagine if Li were deintercalated from $LiMn_2O_4$ and H were intercalated into $VO_2(B)$ during the charge of $LiMn_2O_4/VO_2(B)$ cells. Then, the electrolyte would become a basic solution of LiOH. If all the Li deintercalated from $LiMn_2O_4$ (approximately 0.1g) and H intercalated into $VO_2(B)$, the electrolyte becomes a highly concentrated LiOH solution (larger than 4 M LiOH). As shown in equation (5.15), the reaction between LiOH and λ-MnO_2 would prevent further Li deintercalation from $LiMn_2O_4$. Figure 5.1 also shows that oxygen evolution appears at about 3.5 V versus Li metal in 1M LiOH (pH=14) aqueous solutions. Since Li deintercalation from $LiMn_2O_4$ appears above 3.8V, it does not proceed in highly concentrated LiOH solutions. Hence if H instead of Li intercalated into $VO_2(B)$ or into γ-$Li_{0.36}MnO_2$, there would be no Li deintercalated from $LiMn_2O_4$ and the cells would not work.

Figure 6.5 shows experimental evidence that it is Li intercalation, not H intercalation which makes these cells work. Figure 6.5a shows the voltage of a $LiMn_2O_4$/Li cell during the charge, and that of a γ–$Li_{0.36}MnO_2$/Li cell during the discharge in a non-aqueous electrolyte of 1 M $LiPF_6$ in PC/EC. Figure 6.5b shows the voltage of a $LiMn_2O_4/\gamma$–$Li_{0.36}MnO_2$ cell (smooth line) during the charge in an aqueous electrolyte of 5 M $LiNO_3$. The calculated voltage of the $LiMn_2O_4/\gamma$–$Li_{0.36}MnO_2$ cell shown in figure 6.5b (points) uses the data from the non-aqueous electrolyte cells shown in figure 6.5a. The times are scaled in figures 6.5a and 6.5b according to the active mass and the cell current in

order to compare the data from different cells. The calculated data and the experimental data shown in figure 6.5b agree very well. Therefore $LiMn_2O_4/\gamma$–$Li_{0.36}MnO_2$ cells with aqueous electrolytes work using lithium intercalation.

Figure 6.6 shows similar experimental results to prove that Li intercalation is responsible for the behavior of $LiMn_2O_4/VO_2(B)$ cells with aqueous electrolytes. Figure 6.6a shows the voltage of a $LiMn_2O_4$/Li cell with a non-aqueous electrolyte (1 M $LiPF_6$ in PC/EC) during charge and the the voltage of a $VO_2(B)$/Li cell during discharge with a non-aqueous electrolyte (1 M $LiAsF_6$ in PC/EC). Figure 6.6b shows the voltage of a $LiMn_2O_4/VO_2(B)$ cell with an aqueous electrolyte of 5 M $LiNO_3$ (smooth line) during the charge. The calculated data shown in figure 6.6b (points) is obtained from the cells with non-aqueous electrolytes shown in figure 6.6a. The times are scaled in figures 6.6a and 6.6b according to the active mass and the cell current in order to compare the data from different cells. The calculated data and experimental data for the $LiMn_2O_4/VO_2(B)$ cell shown in figure 6.6b agree very well. The small difference of the voltage between calculation and experiments is due to the slight change of $VO_2(B)$ oxygen content during its exposure to air.

More research is needed before this aqueous Li-ion technology can be considered for the practical applications. Most important is increasing the cycle life of these cells. The best lithium salt must be selected for the aqueous electrolytes with respect to the factors of price and performance. Better electrode materials are needed for these applications.

In a 1989 review of about 40 battery technologies for EV applications, Ratner et al concluded that there was no suitable technology currently available for electric vehicles. The review considered factors including cost, safety,

performance and environmental friendliness. Today, the search for an acceptable EV battery continues. It is our opinion that the aqueous Li-ion approach described here shows good promise and needs to be included in the hunt for the EV battery.

Table 6.1 Summary of matrix tests of aqueous cells (Ti is denoted for titanium hardware, 1225 is for the coin cell hardware).

Battery No.	Construction	Anode	Electrolyte	Initial Upper Cut off (V)	1st charge capacity (mAh)	1st discharge capacity (mAh)	2nd charge capacity (mAh)	2nd discharge capacity (mAh)
1	Ti	$Li_{0.36}MnO_2$	5M LiCl adjusted to pH of 12 with LiOH	1.2	6.5	5.3	5.9	5.4
2	1225	$Li_{0.36}MnO_2$	8M Li(acetate)	1.3	7.0	4.4	9.8*	7.4*
3	1225	$Li_{0.36}MnO_2$	1.5M Li_2SO_4	1.3	13.2	6.0	8.1	5.4
4	1225	$Li_{0.36}MnO_2$	5.7M $LiNO_3$ pH=7	1.3	13.5	8.1	10.0	7.8
5	1225	$Li_{0.36}MnO_2$	10M LiCl adjusted to pH of 12 with LiOH	1.3	4.4	3.0	6.6*	4.1*
6	1225	$LiMn_2O_4$	10M LiCl adjusted to pH of 12 with LiOH	1.4	3.5	3.2	0.9	0.8
7	Ti	$LiMn_2O_4$	10M LiCl adjusted to pH of 12 with LiOH	1.4	6.7	5.3	6.4	5.8
8	Ti	VO_2(B)	5.7M $LiNO_3$ adjusted to pH of 12 with LiOH	1.7	11.0	9.3	10.0	9.0
9	1225	VO_2(B)	5.7M $LiNO_3$ adjusted to pH of 12 with LiOH	1.7	11.7	9.5	10.4	9.6
10	1225	$LiMn_2O_4$	5.0M $LiNO_3$	1.5	7.2	6.7	3.3	3.2
11	1225	$LiMn_2O_4$	5.0M $LiNO_3$	1.4	5.1	4.6	3.1	2.9

* denotes upper voltage cutoff was raised after 1st cycle

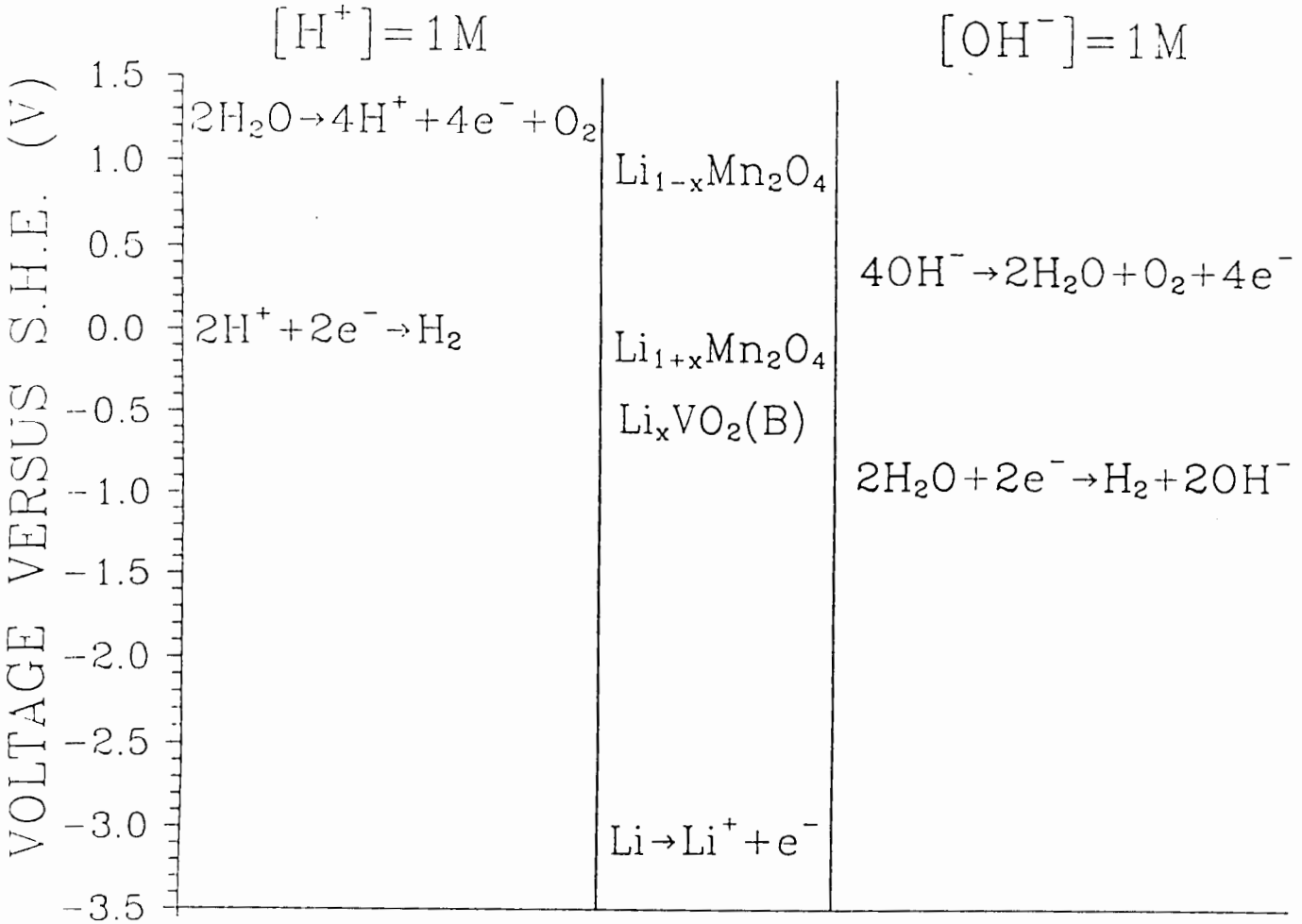

Figure 6.1. The potentials of the indicated reactions versus the Standard Hydrogen Electrode in solutions where $[Li^+]$=1.0 M. Both acidic and basic electrolytes with 1 M H^+ or 1 M OH^- respectively are considered.

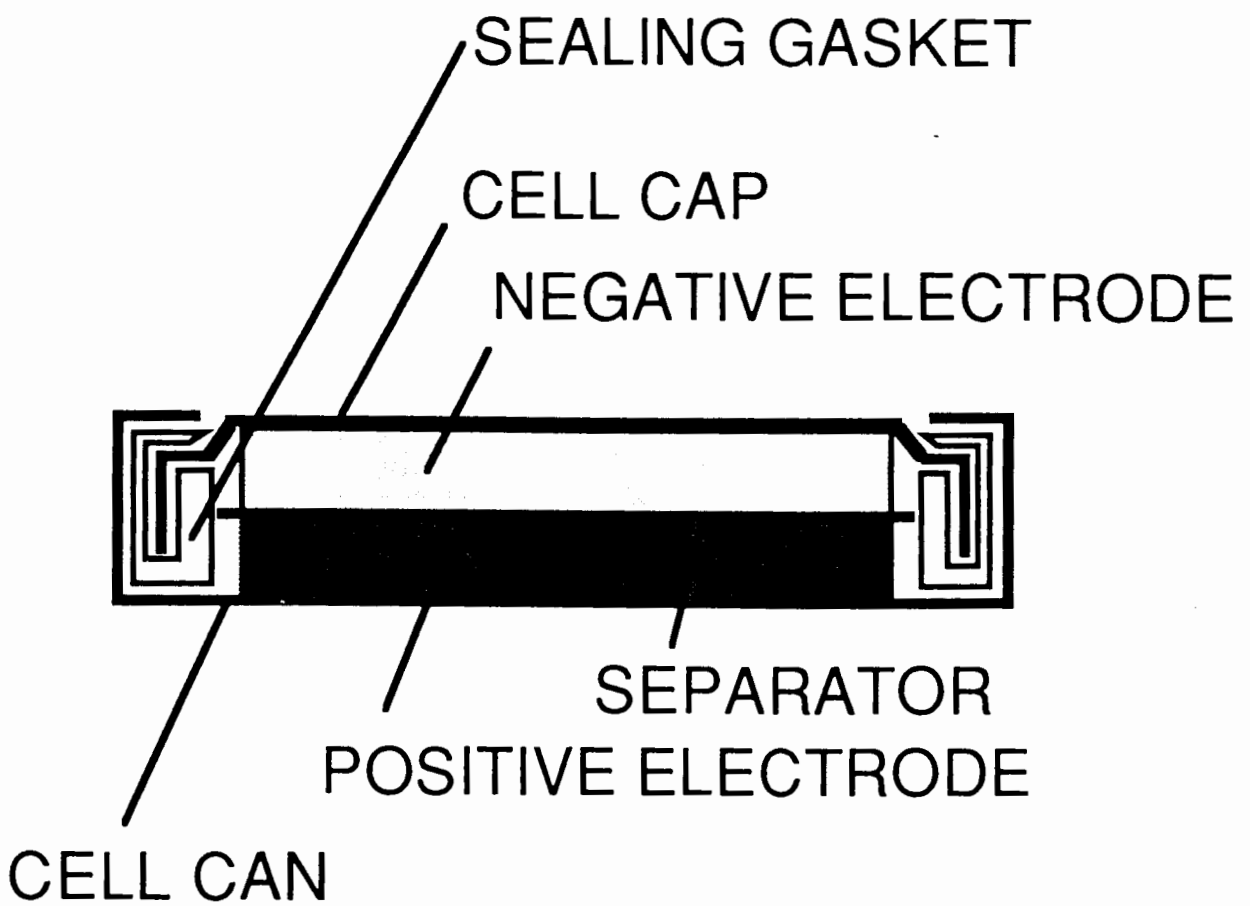

Figure 6.2. A shematic of the coin cell used to test the aqueous Li-ion chemistry.

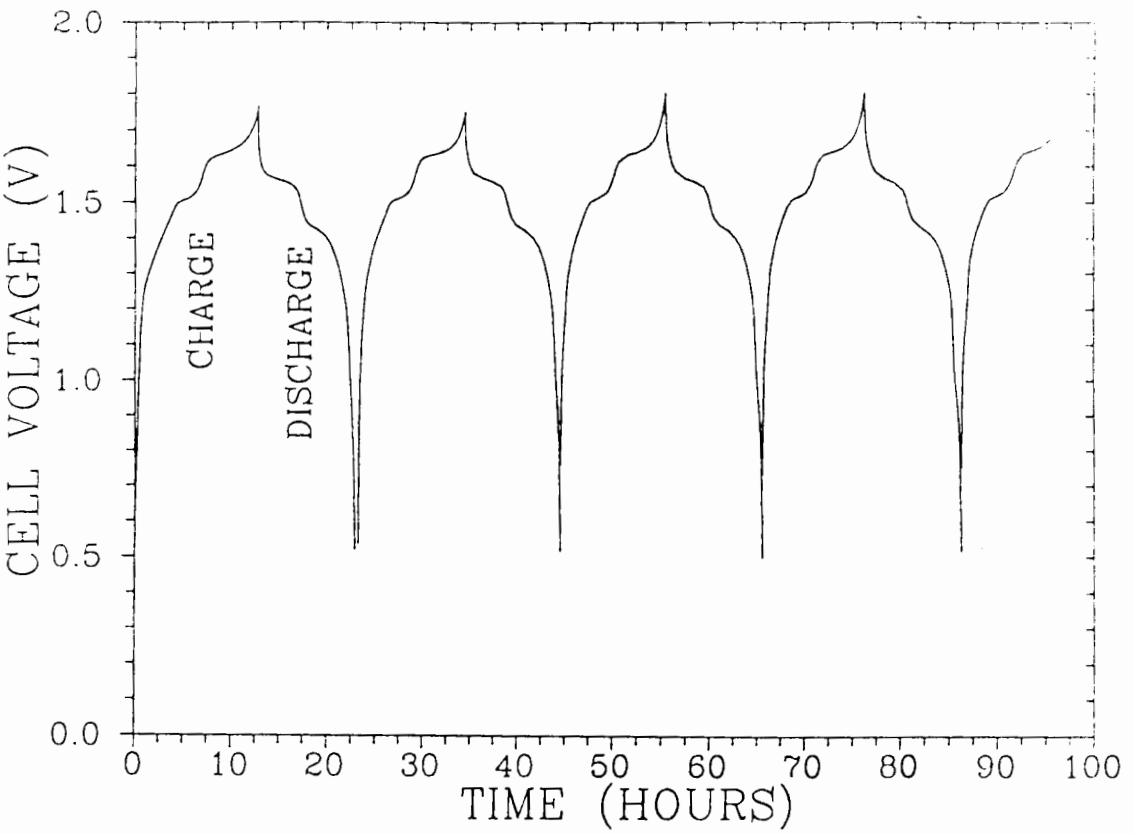

Figure 6.3. The voltage plotted versus time as a $LiMn_2O_4/VO_2(B)$ cell is repeatedly charged and discharged. The currents used were ±1 mA. The cell test was carried out at 30°C.

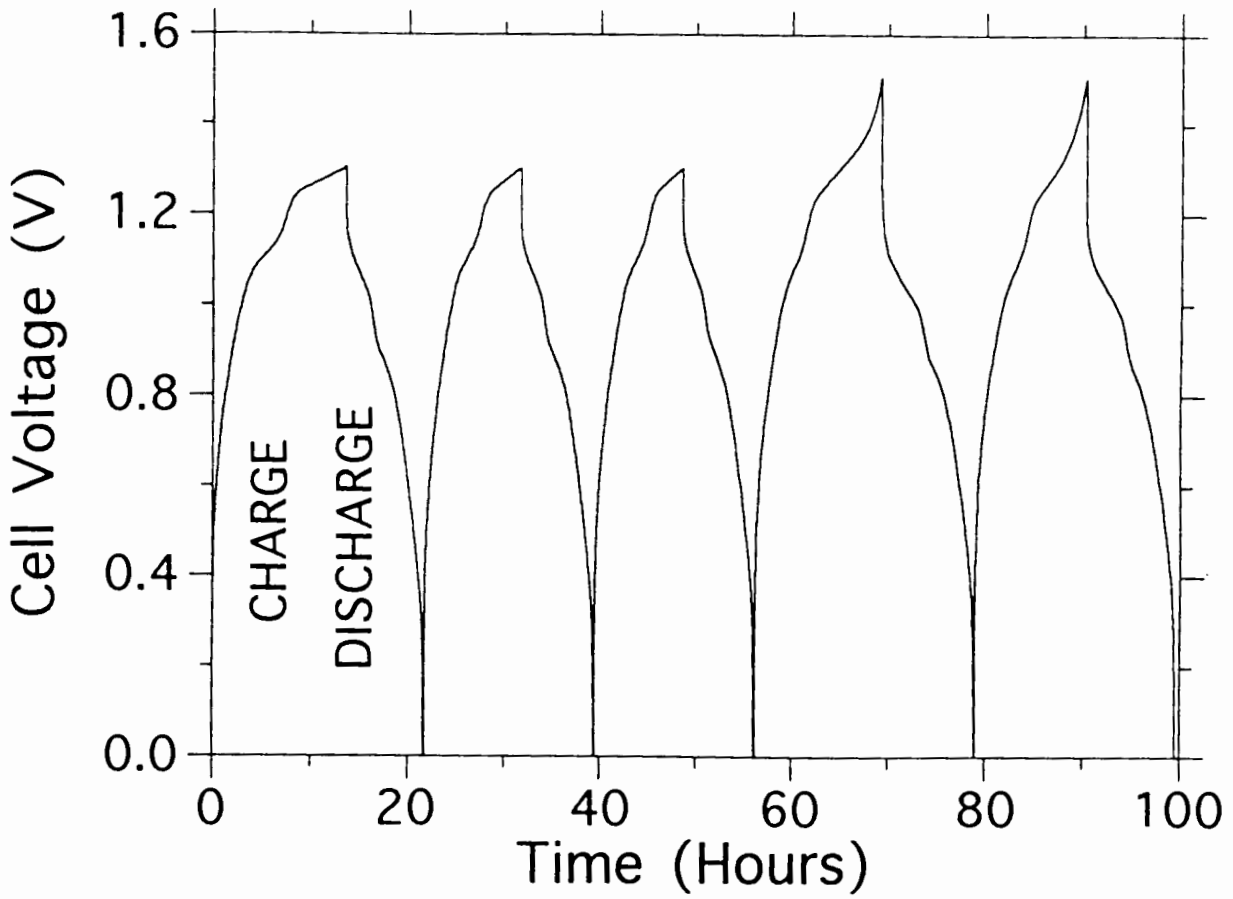

Figure 6.4. The voltage plotted versus time as a $LiMn_2O_4/\gamma$–$Li_{0.36}MnO_2$ cell is repeatedly charged and discharged. The currents used were ±1 mA. The cell test was carried out at 30°C.

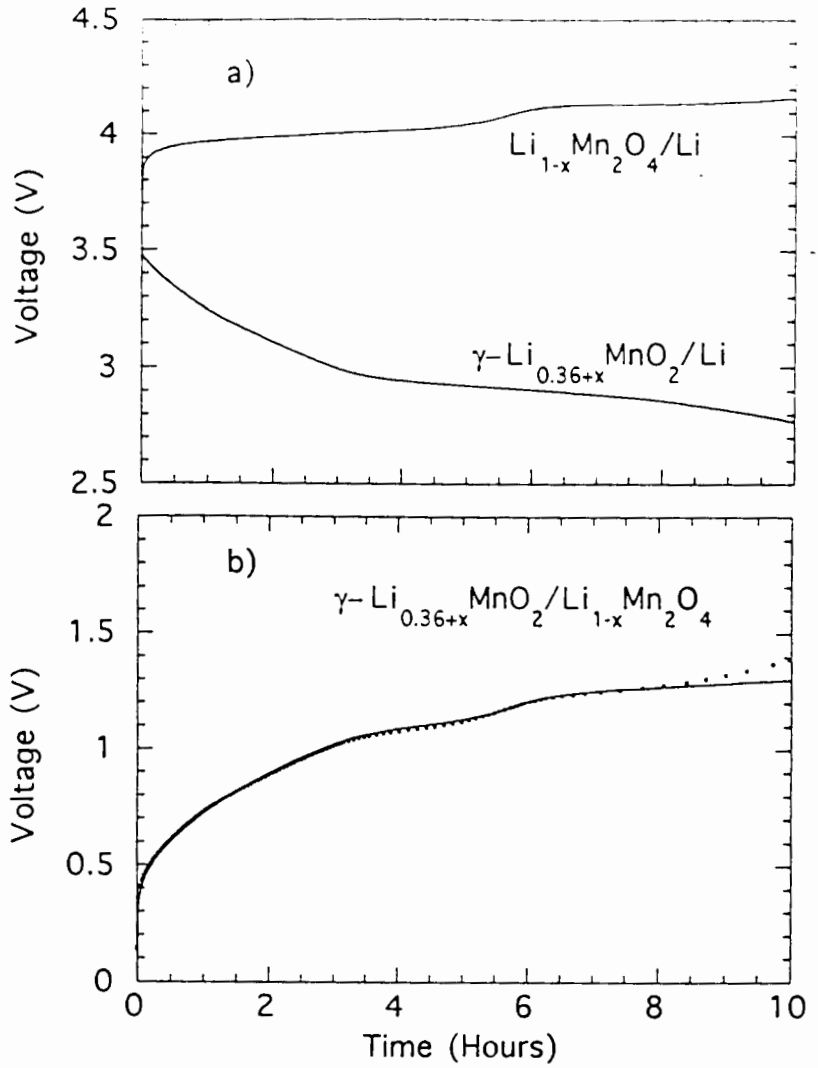

Figure 6.5. a). The voltage plotted versus time as a $LiMn_2O_4/Li$ cell is charged and as a γ–$Li_{0.36}MnO_2/Li$ cell is discharged. Both cells used non-aqueous electrolytes of 1 M $LiPF_6$ in PC/EC. The time was scaled in order to compare with the aqueous cell. b) The voltage plotted versus time as a $LiMn_2O_4/\gamma$–$Li_{0.36}MnO_2$ cell (smooth line) with an aqueous electrolyte of 5 M $LiNO_3$ is charged. The data points calculated from the voltage of the $LiMn_2O_4/Li$ cell minus the voltage of the γ–$Li_{0.36}MnO_2/Li$ cell in a) are also shown.

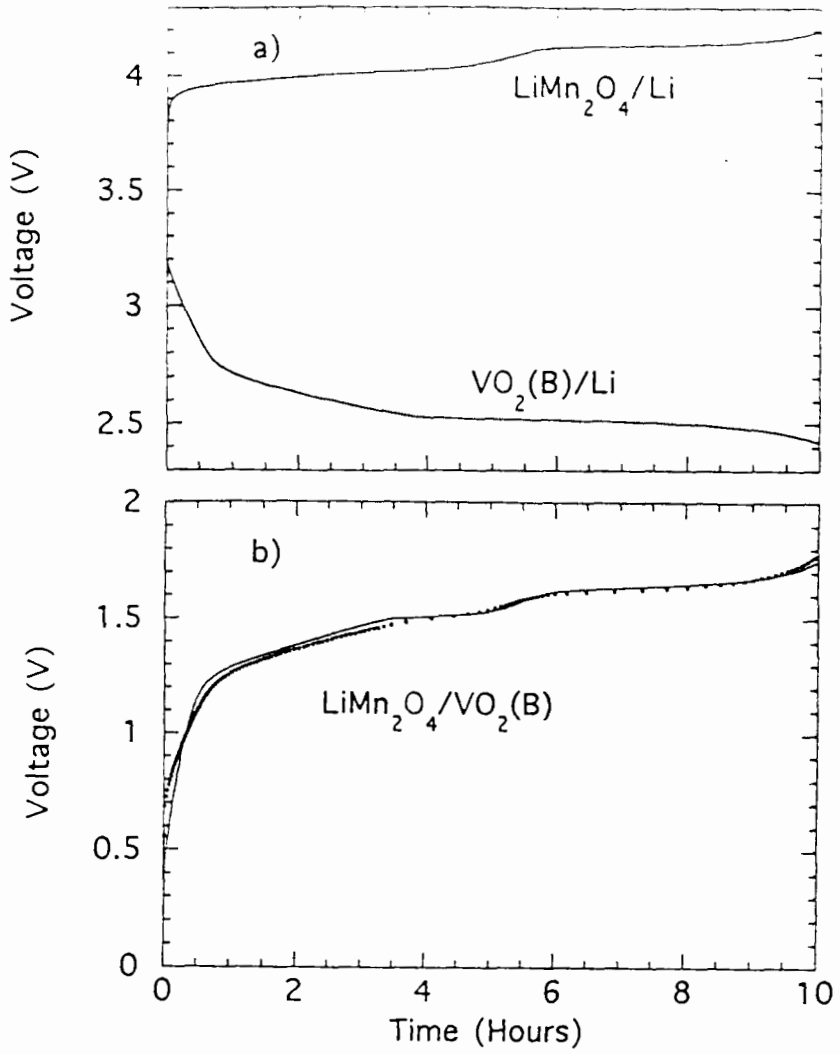

Figure 6.6. a). The voltage plotted versus time as a $LiMn_2O_4/Li$ cell with 1 M $LiPF_6$ in PC/EC is charged and the voltage plotted versus time as a $VO_2(B)/Li$ cell with 1 M $LiAsF_6$ in PC/EC is discharged. The time was scaled in order to compare with the aqueous cell. b) The voltage plotted versus time as a $LiMn_2O_4/VO_2(B)$ cell with an aqueous electrolyte of 5 M $LiNO_3$ (smooth line) is charged. The data points calculated from the voltage of the $LiMn_2O_4/Li$ cell minus the voltage of the $VO_2(B)/Li$ cell in a) are also shown for comparison.

Chapter 7. Conclusions

7.1 Summary

In this thesis, we have shown that the structures of intercalation compounds strongly affect their electrochemical behavior. The structures of the important lithium transition metal oxides and manganese oxides have been described in detail. Using a lattice gas-model, we understood many of the structures of $LiMO_2$ materials, including the spinel, the layered and γ–$LiFeO_2$ structures. Furthermore, we proved that the spinel and undistorted layered structures have the same free energies by using both mean field theory and Monte Carlo methods. We also proved that the powder diffraction pattern from the spinel and the layered materials are identical, independing of the scattering probe, if the hexagonal distortions from the layered structure are ignored. The theoretical results have been used successfully to explain the HT-$LiCoO_2$ and LT-$LiCoO_2$ structures.

Using a new in-situ x-ray cell, we measured the structures of Li_xNiO_2, as a function of x. Three hexagonal phases and one monoclinic phase are observed. Three coexisting phase regions are also found.

During the study of aqueous electrolytes, we discovered lithium intercalation from aqueous solutions. Using this method, we synthesized spinel $Li_2Mn_2O_4$ materials. Furthermore, we found the conditions in which lithium intercalation from aqueous solutions can be observed instead of hydrogen evolution. A theory is also proposed to understand lithium intercalation from aqueous solutions.

Based on the understanding of the lithium intercalation from aqueous solutions, we used aqueous electrolytes to make the rechargeable lithium cells

, which can compete on energy basis with nickel-cadmium and lead-acid cells. Such a fundamentally safe and inexpensive technology provides a new option for scientists and engineers to make practical batteries for the electric vehicle applications.

7.2 Future Work

More work is required on some other structures of lithium transition metal oxides. For example, γ–Li_xMnO_2 is important for lithium battery applications and it is not theoretically understood. Since Mn is cheaper and more environmental friendly than Co and Ni, manganese compounds need more attention in future work on rechargeable lithium battery applications. Further work is also required to solve the safety problems of rechargeable lithium batteries when non-aqueous electrolytes are used. New cathode materials with higher specific capacities need to be discovered to improve the specific energy of lithium ion cells.

Rechargeable lithium batteries with aqueous electrolytes is an attractive possibility for electric vehicle applications. It may be possible to increase the energy density of these batteries by increasing the working cell voltage since lead-acid batteries work at 2 V with aqueous electrolytes. More work is needed to understand the competition between hydrogen intercalation and lithium intercalation from aqueous electrolytes.

Reference

Abraham K. M., Goldman J. L., and Dempsey M. D., J. Electrochem. Soc. **128**, 2493 (1981)

Anderson J. C. and Schieber M., J. Phys. Chem. Solids **25**, 961 (1983).

Barboux P., Shokoohi F. K. and Tarascon J. M., U. S. patent 5,211,933 (1993).

Battery & EV Technol. **12** (7), 2 (1988).

Berlinsky A. J., Unruh W. G., McKinnon W. R. and Haering R. R., Solid State Commun. **31**, 135 (1979).

Binder K, Monte Carlo Methods in Statistical Physics (Springer-Verlag, 1986)

Binder K., Phys. Rev. Lett. **45**, 811 (1980).

Bockris J. O'M and Reddy A. K. N., Modern Electrochemistry **2**, Plenum Press, New York (1970).

Bongers P. F., Ph. D dissertation, The University of Leiden, Leiden, The Netherlands (1957).

Bronger V. W., Bade H., and Klemm W., Z. Anorg. Allg. Chem. **333**, 188 (1964).

Campet G. et al, Mater. Sc. Eng. B **8**, 303 (1991).

Cava R. J., Murphy D. W., Zahurak S., Santoro A. and Roth R. S., J. Solid St. Chem. **53**, 64 (1984).

Chieh C., Chamberland B. L and Wells A. F., Acta Cryst. **B37**, 1813 (1981).

Clapp P. C., and Moss S. C., Phys. Rev. **171**, 754 (1968).

Dahn J. R., Py M. A. and Haering R. R., Can. J. Phys. **60**, 307 (1982).

Dahn J. R., Sacken von U. and Michal C. A., Solid State Ionics **44**, 87 (1990).

Dahn J. R., Buuren T. van, and Sacken T. von, U. S. Patent 4,965,150 (1990).

Dahn J. R., Sacken U. von, Juzkow M. W. and Al-Janaby H., J. Electrochem. Soc., **138** 2207 (1991).

Dahn J. R., Sleigh A. K., Shi Hang, Way B. M., Weydanz W. J., Reimers J. N., Zhong Q. and Sacken U. von , Electrochimica Acta, **38**, 1179 (1993).

David W. I. F., Goodenough J. B., Thackeray M. M., Thomas M. G. S. R., Rev. Chim. Miner. **20**, 636 (1983).

Davidson I. J., McMillan R. S., and Murray J. J., 7th International Meeting on Lithium Batteries, Boston, Massachusettes, U. S. A. May 15-20 (1994).

Delmas C., Braconnier J. and Hagenmuller P., Mater. Res. Bull. **17**, 117(1953).

Desilvestro J. and Haas O., J. Electrochem. Soc., **137**, 5C (1990).

Ducastelle F., Order and Phase Stability in Alloys (North Holland, Amsterdam, 1991).

Dudley J. T. et.al , J. Power Sources **35**, 59 (1991).

Dyer L. D., Borie B. S. and Smith G. P. J. Am. Chem. Soc. **78**, 1499 (1954).

Falk S. U. and Salkind A. J. "Alkaline Storage batteries", Wiley, New York (1969).

Ferrenberg A. M. and Swendsen R. H., Comput. Phys. **3**, 101 (1989).

Fey G. T. K., Li W. and Dahn J. R., J. Electrochem. Soc. **141,** 2279 (1994).

Finel A., Ph. D. thesis, University of Paris, 1987.

Fong R., Sacken von U. and Dahn J. R., J. Electrochem. Soc. **37**, 2009 (1990).

Gahn H., J. Phys. Chem. Solids **43**, 977 (1982).

Globe and Mail, "Cellular Phone Recall May Cause Setback for Moli", August 15, 1989 (Toronto, Canada).

Glover D., Schumm B., Kozawa Jr. and A., Editors, Handbook of Manganese Dioxides Battery Grade, the Int'l Battery Material Ass'n (IBA, Inc.) 1989.

Goodenough J. B., Wickham D. G., and Croft W. J., J. Phys. Chem. Solids **5**, 107 (1958).

Gummow R. J., Thackery M. M., David W. I. F., and Hull S., Mat. Res. Bull. (1992).

Gummow R. J., Liles D. C. and Thackeray M. M., Mater. Res. Bull. **28**, 235 (1993).

Hill R. J. and Howard C. J., J. Appl. Cryst. **18**, 173 (1985).

Hoppe R. , Angew. Chem. **71**, 457 (1959).

Hoppe von R., Brachtel and Jansen M., Z. anorg. allg. Chemie **417**, 1 (1975).

Hestermann K. and Hoppe R., Z. anorg. allg. Chem. **367**, 261 (1969).

Hewston T. A. and Chamberland B. L., Phys. Chem. Solids **48**, 97 (1987).

Hunter J. C. , U. S. Patent 4,246,253 (1981).

International Tables for X-ray Crystallography, vol. 1, The Kynoch Press, Birmingham, England (1969), Editors: Norman F. M. Henry et al.

Johnston W. D. and Heikes R. R., J. Am. Chem. Soc. **78**, 3255 (1956).

Kanoh H., Feng Q., Miyai Y., and Ooi K., J. Electrochem. Soc. **140**, 3162 (1993).

Kao W. H., Weibel V. J. and Root M. J., J. Electrochem. Soc., **139**, 1223 (1992).

Kordesch K., Harer W., Taucher W. and Tomantscher K. in "Proceedings of 22nd Intersociaty Energy Conversion Engineering Conference" **2**, 1102 (1987).

Kuribayashi I., JEE October 52 (1993)

Li W., M. Sc. thesis, Simon Fraser University, 1992.

Li W., Reimers J. N. and Dahn J. R., Phys. Rev. B **46**, 3236 (1992).

Li W., Reimers J. N. and Dahn J. R., Solid State Ionics **67**, 123 (1993).

Li W., Reimers J. N. and Dahn J. R., Phys. Rev. B **49**, 826 (1994).

Li W. and Dahn J. R., Canadian Patent Application filed in Jan. 1994.

Li W., W. R. McKinnon and J. R. Dahn, J. Electrochem. Soc. **141**, 2310 (1994).

Li W., Dahn J. R. and Wainwright D. S., Science **264**, 1115 (1994).

Linden D., in "Handbook of Batteries and Fuel Cells". D. Linden, Editor, p. 11-1, McGraw-Hill, Inc. New York, (1984).

Manev V., Momchilov A., Nassalevska A., and Kozawa A., J. Power Sources, **44**, 305 (1993).

McKinnon W. R. and Haering R. R., 1983 Modern Aspects of Electrochemistry No. 15, ed. R. E. White, J. O'M Bockris and B. E. Conway (New York: Plenum).

Mizushima K., Jones P. C., Wiseman P. J. and Goodenough J. B., Mater. Res. Bull. **15**, 783 (1980).

Mohri T., Sahchez J. M., and De Fontaine D., Acta Metall. **33** , 1171 (1985).

Molicel $^{2\ TM}$ Product data sheet, Moli Energy Ltd.

Murphy D. W., Christian P. A., DiSalvo F. J. and Carides J. N., J. Electrochem. Soc. **126**, 497 (1979).

Murphy D. W. et al. J. Electrochem. Soc. **128**, 2053 (1981).

Nagaura T. and Tozawa K., Progress in Batteries and Solar Cells **9**, 209 (1990).

Nassau K. and Murphy D.W., J. Non-Cryst. Solids **44**, 297 (1981)

Nohma T., Saito T., Furukawa N. and Ikeda H., J. Power Sources **26**, 389 (1989).

Nohma T., Yamamoto Y., Nishio K., Nakane I. and Furukawa N., J. Power Sources **32**,373 (1990).

Ohzuku T., Kitagawa M. and Hirai T., J. Electrochem. Soc. **137**, 40 (1990).

Ohzuku T., Ueda A. and Hirai T., Chmistry Express **7**, 193 (1992).

Ohzuku T., Ueda A. and Nagayama M., J. Electrochem. Soc. **140**, 1862 (1993).

Ohzuku T and Ueda A., Solid State Ionics, in press (1994).

Paner S., Pasquali M. and Pistoia G., J. Electrochem. Soc. **130**, 1225 (1983)

Pistoia G., Pasquali M., Tocci M., Manev V. and Moshtev R. V., J. Power Source **15**, 13 (1985)

Phani M. K., Lebowitz J. L., and Kalos M. H. , Phys. Rev. B **21**, 4027 (1980).

Ratner E. Z., Symons P. C., Walsh W., Warde C. J., and Hendriksen G. L., "Assessment of Battery Technologies for Electric Vehicles", U. S. Dept. of Energy Contract DE-AC07-76ID01570, August 1989.

Reimers J. N. and Dahn J. R., J. Phys.:Condens. Matter **4**, 1(1992).

Reimers J. N. and Dahn J. R., J. Electrochem. Soc. **139**, 2091 (1992).

Reimers J. N., Li W., Rossen E., and Dahn J. R., Proceeding Material Research Society (1992).

Reimers J. N., Li W. and Dahn J. R., Phys. Rev. B **47**, 8486 (1993).

Reimers J. N., Fuller E. W., Rossen E. and Dahn J. R., J. Electrochem. Soc. **140**, 3396 (1993).

Richards M. S. and Cahn J. M. , Acta Metall. **19**, 1263 (1971).

Rietveld H. M., Acta Crystallogr. **22**, 151 (1967).

Rossen E., Reimers J. N. and Dahn J. R., Solid State Ionics **62**, 53 (1993).

Rudorff W. and Becker H., Z. Naturforsch. **9B**, 613 (1954).

Sacken von U., Nodwell E., Sundher A., and Dahn J. R. submitted to Solid State Ionics

Sakurai Y., Okada S., Yamaki J. and Okada T., J. Power Sources **20**, 297 (1987)

Sanchez J. M. and De Fontaine D., Phys. Rev. B **25**, 1759 (1982).

Sharpe A. G., Inorganic Chemistry, Longman Group Limited, England, 1981.

Shockley W. , J. Chem. Phys. **6**, 130 (1938).

Styer D. F., M. K. Phani, and J. L. Lebowitz, Phys. Rev. B **34**, 3361 (1986).

Tarascon J. M. and Guyomard D., Electrochimca Acta **38**, 1221 (1993).

Tarascon J. M. and Guyomard D., J. Electrochem. Soc. **138**, 2864 (1993).

Tarascon J. M., U. S. patent 5,196,279 (1993).

Thomas M. G. S. R. , Bruce P. G. and Goodenough J. B., Solid State Ionics **18/19**, 794 (1986).

Thackeray M. M., Kock de A., Rossouw M. H. and Liles D., Bittihn R. and Hoge D., J. Electrochem. Soc. **137**, 769 (1990).

Thackeray M. M., David W. I. F., Bruce P. G. and Goodenough J. B., Mater. Res. Bull. **18**, 461 (1983).

Thackeray M. M., Rossouw M. H., Gummow R. J., Liles D. C., Pearce K., Kock de A., David W. I. F., and Hull S., Electrochemica Acta. **38**, 1259 (1993).

Toyoguchi Y. , Yamaura J., Matsui T. and Iijima J., Abstract 73, p. 109, The Electrochemical Society Extended Abstracts Vol. 87-2, Honolulu, HI Oct. 18-23 (1987)

Voorn G. , J. Power Source **14**, 135 (1985)

Warren B. E., X-ray Diffraction, Addison-Wesley Publishing Company (1969)

Weast R. C. and Astle M. J., Handbook of Chemistry and Physics, 60th edition, CRC Press Inc., Boca Raton, Florida(1979-1980).

Wyckoff R. W. G., Crystal Structures (2nd edn), Vol. 2, p. 312 Interscience, New York (1964).

Yamamoto O., Takeda Y., Kammo R., Oyabe Y. and Shiuya, J. Power Sources **20**, 151 (1987).

Way B. M. and Dahn J. R., J. Electrochem. Soc., **141**, 907 (1994).

Weydanz W. J., Way B. M., Buuren T. Van and Dahn J. R., J. Electrochem. Soc., **141**, 900 (1994).